DOCTORAL THESIS

Investigating the electro-optical properties of 3D superlattices and 2D materials: A DFT study

A thesis submitted to the Institute of Physics, Polish Academy of Sciences in partial fulfillment of the requirements for the degree Doctor of Philosophy supervised by Dr. hab. Carmine Autieri, prof. IFPAN and auxiliary supervisor Dr. Giuseppe Cuono.

By

Ghulam Hussain

Institute of Physics, Polish Academy of Sciences

Warsaw Poland

January 2023

Dedication and acknowledgements

I would like to say special thanks to my supervisor Dr. Carmine Autieri for his continuous support and guidance throughout my PhD. In addition, I am very thankful to Prof. Tomasz Dietl and my co-guide Dr. Giuseppe Cuono for their assistance and constructive suggestions. Last but not the least, I pay gratitude to my friends and my beloved family, without whose endless love, encouragement and support, I could not achieve this.

Moreover, we appreciate the support of the Foundation for Polish Science through the international research agendas program co-financed by the European Union within the smart growth operational program.

Author's declaration

I hereby certify that the work contained in this dissertation has not been submitted for consideration in any other academic awards and has been completed in accordance with the rules and guidelines of the Institute of Physics, Polish Academy of Science (IFPAN) and the Code of Practice for Research Degree Programs. Unless otherwise specified by a specific reference in the text, the work is the candidate's own contribution. Work accomplished with the assistance of or in collaboration with others is acknowledged as such. In the dissertation, only the author's viewpoints are given.

SIGNED: .... DATE: ....

List of publications

This thesis includes the following papers, where I contributed as the 1st author highlighted by bold text.

Ghulam Hussain, Giuseppe Cuono, Rajibul Islam, Artur Trajnerowicz, Jarosław Jureńczyk, Carmine Autieri, Tomasz Dietl. *Electronic and optical properties of* $InAs/InAs_{0.625}Sb_{0.375}$ *superlattices and their application to far-infrared detectors,* Journal of Physics D: Applied physics **55**, 495301 (2022)

Ghulam Hussain, Mazia Asghar, Muhammad Waqas Iqbal, Hamid Ullah, Carmine Autieri. *Exploring the structural stability, electronic and thermal attributes of synthetic 2D materials and their heterostructures*, Applied Surface Science **590**, 153131 (2022)

Ghulam Hussain, Mumtaz Manzoor, Muhammad Waqas Iqbal, Imran Muhammad, Asadollah Bafekry, Hamid Ullah, Carmine Autieri. *Strain modulated electronic and optical properties of laterally stitched* $MoSi_2N_4/XSi_2N_4$ *(X=W, Ti) 2D heterostructures,* Physica E **144**, 115471 (2022)

Ghulam Hussain, Abdus Samad, Majeed Ur Rehman, Giuseppe Cuono, Carmine Autieri. *Emergence of Rashba splitting and spin-valley properties in Janus* $MoGeSiP_2As_2$ *and* $WGeSiP_2As_2$ *monolayers,* Journal of Magnetism and Magnetic Materials **563**, 169897 (2022)

Publications other than thesis

I also contributed in the following papers.

Giuseppe Cuono, **Ghulam Hussain**, Amar Fakhredine, and Carmine Autieri. *Topological phase diagram of* $Pb_{1-x}Sn_xSe_{1-y}Te_y$ *quaternary compound* (Accepted in Acta Physics Polonica A)

Rajibul Islam, **Ghulam Hussain**, Rahul Verma, Mohammad Sadegh Talezadehlari, Zahir Muhammad, Bahadur Singh and Carmine Autieri. *Electrically-controllable large gap quantum spin Hall phase in* MGe_2Z_4 (Submitted)

Mian Muhammad Faisal, Syeda Ramsha Ali, **Ghulam Hussain**, Carmine Autieri, Sanal Kozhiparambil Chandran. *Development of 2D* W_2CT_x *MXene from non-MAX Phase W-Sn-C for Electrochemical Energy Storage Devices: Experiment and theory* (Submitted)

Zahir Muhammad, Faiz Wali, **Ghulam Hussain**, Rajibul Islam, Sami Ullah, Carmine Autieri, Peng Wu, Firoz Khan, Yue Zhang, Thamraa Alshahrani, and Weisheng Zhao. *Anisotropic phonon dispersion and optoelectronic properties of a few layers* HfS_2, J. Mater. Chem. C, (2023)

CERTIFICATE

This is to certify that the thesis entitled "Investigating the electro-optical properties of 3D superlattices and 2D materials: A DFT study", submitted by Ghulam Hussain to Institute of Physics, Polish academy of sciences, is a record of bona fide research work under our supervision and guidance, and we consider it worthy of consideration for the award of the degree of Doctor of Philosophy of the Institute.

Supervisor

Dr. hab. Carmine Autieri, prof. IFPAN
MagTop, Institute of Physics, Polish academy of sciences
Warsaw, Poland

Auxiliary supervisor

Dr. Giuseppe Cuono
MagTop, Institute of Physics, Polish academy of sciences
Warsaw, Poland

ABSTRACT

The electromagnetic radiations can propagate in space, which could interact with the matter in various ways. Advancement in the electronic industry demands to explore new materials with pronounce electronic and optical features. Due to the boosted semiconductor industry, the optoelectronic devices are extensively employed in manufacture, medicine, astronomy, automobile, communications, military, and so on, reshaping our lives. These include light emitting diodes, semiconducting lasers, photovoltaic devices, photodiodes and photodetectors. Previous studies incorporate the investigation of optoelectronic properties for different materials such bulk systems, alloys, thin films and 2D layered structures. Currently, the Ga- and Hg-free type-II superlattices of InAs/(InAsSb) are highly demanding in the infrared industry due to their unique optoelectronic properties. Moreover, the distinct mechanical and electro-optical features of the newly discovered 2D materials family MA_2Z_4 as compared to other 2D materials necessitates further studies to explore this 2D material class.

Motivated from the outstanding characteristics of Ga- and Hg-free type-II superlattices of InAs/(InAsSb), and the extraordinary mechanical and electro-optical features of MA_2Z_4 family, we explore here the electronic and optical properties of $InAs/InAs_{0.625}Sb_{0.375}$ 3D superlattice (SL), 2D materials XSi_2N_4 (X = Mo, W, and Ti) and their vertical/lateral heterostructures $MoSi_2N_4/XSi_2N_4$ (W, Ti), and Janus structures.

In the study of $InAs/InAs_{0.625}Sb_{0.375}$ 3D superlattice, the modified Becke-Johnson exchange-correlation functional is employed to have a good description of the electronic and optical properties. The bulk InAs and InSb are analyzed first and then the $InAs/InAs_{0.625}Sb_{0.375}$ superlattice for the three lattice constants of the bulk InAs, GaSb and AlSb is investigated, respectively. A strong dependence of electronic and optical properties on the variation of lattice constant is observed. There exists two heavy-hole bands with increasing in-plane effective mass as one goes far from the Fermi level. In addition, a considerable decrease in the effective masses for heavy-holes and energy gaps in the k_x-k_y plane is noticed as compared to their bulk phases of the parent compounds. We noticed that the electrons are delocalized in the InAs part of SL, while the holes mainly are localized in the $InAs_{0.625}Sb_{0.375}$ part. The absorption spectra in the far-infrared regime are strongly increased in the case of the aforementioned superlattice with respect to bulk InAs and InSb suggesting their applications in long-wavelength IR detectors.

In the second project, we discuss newly discovered 2D layered materials such as XSi_2N_4 (X = Mo, W, and Ti), and their vertical and laterally stitched 2D heterostructures $MoSi_2N_4/XSi_2N_4$ (X=W, Ti). We report that all the systems are structurally stable as confirmed by the total energy ground state calculations and the phonon spectra. After establishing their thermodynamical stability, we study the electronic band structures and the density of states of the monolayers XSi_2N_4 (X = Mo, W, and Ti) and 2D heterostructures, respectively. Both the monolayers and the heterostructures demonstrate a semiconducting behavior with band gaps ranging from the infrared to the visible

region. From the electronic band structures, we noticed that the band gap of $MoSi_2N_4/WSi_2N_4$ lies in the visible region employing their applications for photovoltaics and other optoelectronic devices. Instead, in the $MoSi_2N_4/TiSi_2N_4$ wherein the 'W' is replaced with 'Ti', the band gap drops to the IR range, thus providing the possibility to utilize these heterostructures as IR detector materials. In the third project, we extend the study of laterally stitched 2D heterostructures to investigate the effect of biaxial strain on the electronic and optical properties, which reveals significant modifications in the electronic band structures and optical spectra. We observed a transition from indirect to direct band gap semiconductor with the compressive strain in $MoSi_2N_4/WSi_2N_4$. Similarly, the biaxial strain causes a semiconducting to metallic transition in $MoSi_2N_4/TiSi_2N_4$. Besides, the optical spectra including absorbance, transmittance and reflectance can be tuned effectively using strain engineering. Our findings based on the electro-optical properties and their controlled modulation via biaxial strain suggest that these newly discovered 2D materials and heterostructures could be useful in nano- and optoelectronics.

Lastly, we study the pristine $MoSi_2P_4$ and Janus phase $XGeSiP_2As_2$ (Mo, W) in this new family of 2D materials. The appearance of high cohesive energies and the absence of imaginary phonon modes confirm their stability and possible experimental realization. The Janus structures indicate small direct band gaps and larger spin splittings at K/K' in comparison to pristine $MoSi_2P_4$. The monolayered structure of Janus material possesses the broken mirror symmetry that gives rise to a potential gradient, which is normal to the plane of the material. This generates a difference in the work function of 2D material for the two surfaces. In addition, it is exposed from the spin textures that the broken mirror symmetry causes the Rashba spin-splitting in the Janus monolayers, which can be increased by using higher atomic spin-orbit coupling. In the supplementary material, we manifest and compare the optical spectra for pristine and Janus phases revealing characteristic absorption peaks in the infrared region. The large spin and Rashba-type splittings together with the exceptional optical spectra in the Janus structures can make an extraordinary contribution to the valleytronics, spintronics and IR applications.

ABSTRAKT

Promieniowanie elektromagnetyczne może rozchodzić się w przestrzeni oddziaływując z materią na wiele sposobów. Postęp w przemyśle elektronicznym wymaga poszukiwania nowych materiałów o specyficznych własnościach elektronowych i optycznych. Urządzenia optoelektroniczne, takie jak diody elektroluminescencyjne, lasery półprzewodnikowe, urządzenia fotowoltaiczne, fotodiody i fotodetektory, są szeroko stosowane w przemyśle, medycynie, astronomii, motoryzacji, komunikacji, wojsku itd., mając duży wpływ na nasze życie. Wcześniejsze prace badawcze dotyczyły właściwości optoelektronicznych różnego rodzaju materiałów, takich jak stopy, cienkie warstwy i inne struktury warstwowe 2D. Obecnie supersieci typu II InAs/(InAsSb) wolne od Ga i Hg są bardzo pożądane dla zastosowań w podczerwieni ze względu na ich unikalne właściwości optoelektroniczne. Z drugiej strony właściwości mechaniczne i elektrooptyczne nowo odkrytej rodziny materiałów 2D MA_2Z_4 predestynują je do zastosowań komercyjnych, ale konieczne są dalsze badania dla scharakteryzowania tej klasy materiałów 2D.

Motywowani nietypowymi właściwościami supersieci typu II bez Ga i Hg InAs / (InAsSb) oraz właściwościami mechanicznymi i elektrooptycznymi rodziny MA_2Z_4, badamy właściwości elektronowe i optyczne supersieci 3D $InAs/InAs_{0,625}Sb_{0,375}$ (SL), materiałów 2D XSi_2N_4 (X = Mo, W i Ti) oraz ich pionowe/boczne heterostruktury $MoSi_2N_4/XSi_2N_4$ (W, Ti) oraz struktury typu Janus.

W badaniu supersieci 3D $InAs/InAs_{0,625}Sb_{0,375}$ zastosowano zmodyfikowany funkcjonał korelacji wymiany Becke-Johnsona, aby uzyskać dobry opis właściwości elektronowych i optycznych. Najpierw analizujemy objętościowe układy InAs i InSb, a następnie badamy supersieci $InAs/InAs_{0,625}Sb_{0,375}$ dla trzech różnych stałych sieciowych: InAs, GaSb i AlSb. Obserwujemy silną zależność właściwości elektronowych i optycznych od wielkości stałej sieciowej. Otrzymujemy dwa pasma ciężkich dziur o rosnącej efektywnej masie w płaszczyźnie w miarę oddalania się od poziomu Fermiego. Ponadto zauważalny jest znaczny spadek mas efektywnych dla ciężkich dziur i przerw energetycznych w płaszczyźnie k_x-k_y w porównaniu z fazami objętościowymi związków macierzystych. Zauważyliśmy, że elektrony są zdelokalizowane w części InAs SL, podczas gdy dziury są zlokalizowane głównie w części $InAs_{0,625}Sb_{0,375}$. Widma absorpcyjne w dalekiej podczerwieni są silnie wzmocnione w porównaniu do objętościowych InAs i InSb, co sugeruje ich zastosowanie w długofalowych detektorach IR.

W drugim projekcie omawiamy nowo odkryte materiały warstwowe 2D, takie jak XSi_2N_4 (X = Mo, W i Ti) oraz ich pionowo i poprzecznie skonfigurowane heterostruktury 2D $MoSi_2N_4/XSi_2N_4$ (X=W, Ti). Okazuje się, że wszystkie systemy są strukturalnie stabilne, co potwierdzają obliczenia stanu podstawowego całkowitej energii i widma fononów. Po ustaleniu ich stabilności termodynamicznej badamy odpowiednio struktury pasm elektronowych i gęstość stanów monowarstw XSi_2N_4 (X = Mo, W i Ti) oraz heterostruktur 2D. Zarówno monowarstwy, jak i

heterostruktury wykazują właściwości półprzewodnikowe z pasmami wzbronionymi w zakresie od podczerwieni do obszaru widzialnego. Na podstawie struktur pasma elektronicznego zauważyliśmy, że pasmo wzbronione $MoSi_2N_4/WSi_2N_4$ leży w obszarze widzialnym, co pozwala na zastosowania w fotowoltaice i innych urządzeniach optoelektronicznych. Natomiast w $MoSi_2N_4/TiSi_2N_4$, gdzie wolfram zastąpiono tytanem, pasmo wzbronione przenosi się do zakresu IR, zapewniając w ten sposób możliwość wykorzystania tych heterostruktur jako detektorów IR. W trzecim projekcie rozszerzamy badanie heterostruktur 2D zszytych bocznie, aby zbadać wpływ odkształcenia dwuosiowego na właściwości elektroniczne i optyczne. Obserwujemy znaczące modyfikacje w strukturach pasm elektronowych i widmach optycznych, w tym przejście od pośredniego do bezpośredniego półprzewodnika z pasmem wzbronionym przy naprężeniu ściskającym w $MoSi_2N_4/WSi_2N_4$. Podobnie odkształcenie dwuosiowe powoduje przejście półprzewodnikowe do metalicznego w $MoSi_2N_4/TiSi_2N_4$. Poza tym widma optyczne, w tym absorbancję, transmitancję i współczynnik odbicia, można skutecznie dostroić za pomocą manipulacji odkształceniem. Nasze badania właściwościach elektrooptycznych i ich kontrolowanej modulacji przez odkształcenie dwuosiowe sugerują, że te nowo odkryte materiały i heterostruktury 2D mogą być przydatne w nano- i optoelektronice.

Badamy również czysty $MoSi_2P_4$ i oraz fazę typu Janus $XGeSiP_2As_2$ (Mo, W). Pojawienie się wysokich energii kohezji i brak urojonych modów fononów potwierdza ich stabilność i sugeruje możliwość przeprowadzenia badań doświadczalnych. Struktury typu Janus wykazują w porównaniu z czystym $MoSi_2P_4$ małe bezpośrednie przerwy wzbronione i większe rozszczepienie spinowe przy K/K'. Jednowarstwowa struktura materiału Janus posiada złamaną symetrię lustrzaną, co powoduje powstanie gradientu potencjału, który jest normalny do płaszczyzny materiału. Generuje to różnicę w funkcji pracy materiału 2D dla dwóch powierzchni. Ponadto z tekstur spinowych wynika, że złamana symetria lustrzana powoduje w monowarstwach typu Janus rozszczepienie spinowe Rashby, które można zwiększyć stosując wyższe atomowe sprzężenie spinowo-orbitalne. W dodatkowym materiale przedstawiamy i porównujemy widma optyczne dla faz czystej i typu Janus, ujawniając charakterystyczne piki absorpcji w obszarze podczerwieni. Duże rozszczepienia spinowe i typu Rashby w połączeniu z wyjątkowymi widmami optycznymi w strukturach Janus mogą być bardzo przydatne w Valleytronice, Spintronice i zastosowaniach w podczerwieni.

Table of Contents

List of figures xx

1 Introduction **1**

1.1 Motivation of $InAs/InAs_{0.625}Sb_{0.375}$ 3D SL………………… 2

1.1.1 Alternatives to HgCdTe……………………… 6

1.2 Two-dimensional (2D) materials……………………... 7

1.2.1 Hybrid 2D materials…………………….. 10

1.2.2 Janus structures…………………….. 10

1.3 MA_2Z_4 2D materials……………………... 12

1.4 Thesis outline…………………….. 12

2 Methodology and Computational Details **14**

2.1 Many body electron system……………………… 14

2.2 Density functional theory (DFT)……………………… 17

2.2.1 Kohn-Sham equations……………………… 18

2.2.2 Local density approximation (LDA)…………………….. 19

2.2.3 Generalized gradient approximation (GGA)…………….. 20

2.2.4 Other exchange-correlation functionals……………….. 20

2.2.5 Plane wave basis set……………………… 20

2.2.6 Pseudopotential…………………….. 21

3 Papers Comprising the Thesis **23**

3.1 A short overview of the main results……………………… 23

3.2 PAPER I: $InAs/InAs_{0.625}Sb_{0.375}$ 3D superlattice……………… 24

3.3 PAPER II: 2D materials and heterostructures……………… 38

3.4 PAPER III: Strain modulated electro-optical properties of laterally stitched 2D heterostructures……………………… 47

3.5 PAPER IV: Janus structures……………………… 58

4 Conclusions **69**

Bibliography 71

List of Figures

1.1 Electromagnetic spectrum increasing wavelength indicated from X-ray to radio, the infrared region is also zoomed with NIR, MWIR, and FIR shown……………….. **03**

1.2 Schematic exhibiting the type-II band alignment; the electrons lie in InAs, while holes are located in GaInSb part of the superlattice…………………………………………. **07**

1.3 Illustration of bandgaps for different 2D materials. The true value of the bandgap is dependent on a number of factors such as the number of layers, chemical doping and strain level……………………………………………………………………………….. **08**

1.4 (a) Side view of vertically stacked heterostructure (b) Top and side views of parallel stitched 2D superlattice of MX_2 class, (c) representation of pristine (MX_2) and Janus structure (MXY)……………………………………………………………………. **11**

1.5 Side and top view of MA_2Z_4 family of 2D materials……………………………… **12**

Chapter 1

INTRODUCTION

The electronic and optical properties are of extreme importance while designing the electronic devices for optoelectronic applications. In optoelectronics, the investigation and utilization of materials is carried out that could 1) produce or become the source of light, 2) detect the light [1]. In the first instance, the electronic devices such as light emitting diodes (LEDs) and the semiconducting lasers are widely employed, which convert the electrical signals into light energy. On the other hand, for the detection purpose devices like photodiodes and photodetectors are commonly used, that convert the light energy into electrical signals. Besides, solar cells are commercially utilized in different parts of the world as a renewable source of energy that convert the sunlight into useful electrical energy through the photovoltaic effect. Owing to the importance of optoelectronics, the investigation of new materials for the electronic and optical features is quite demanding.

To this end, we first explore the $InAs/InAs_{0.625}Sb_{0.375}$ 3D superlattice (SL) and then 2D materials, which include XSi_2N_4 (X = Mo, W, and Ti) monolayers and their vertical/lateral heterostructures (such as $MoSi_2N_4/WSi_2N_4$, and $MoSi_2N_4/TiSi_2N_4$), and the Janus structures $XGeSiP_2As_2$ (X = Mo, W). The thesis comprises four chapters, **chapter 1** that is devoted to introduction, while the methodology is explained in **chapter 2**, **chapter 3** consists of results and discussion, where we include four published papers, and the last **chapter 4** covers conclusions.

In paper I, we investigate the electronic and optical properties of the bulk InAs, InSb and that of $InAs/InAs_{0.625}Sb_{0.375}$ SL and emphasizes why the $InAs/InAs_{0.625}Sb_{0.375}$ 3D superlattices are suitable for applications in far infrared detection. In paper II, we report the newly discovered 2D layered materials such as XSi_2N_4 (X = Mo, W, and Ti), and their vertical/lateral heterostructures like $MoSi_2N_4/WSi_2N_4$, and $MoSi_2N_4/TiSi_2N_4$. It is established that the monolayers as well as the heterostructures are structurally stable with unique electronic properties as confirmed from the density of states and electronic bandstructures. Both, the monolayers and the heterostructures demonstrate a semiconducting behavior with band gaps ranging from the infrared to the visible region. The paper III is the extension of paper II, where the effect of biaxial strain on the electro-optical properties of laterally stitched heterostructures is explored. The study revealed substantial modifications in the electronic and optical properties. In paper IV, the pristine $MoSi_2P_4$ and Janus $XGeSiP_2As_2$ (X = Mo, W) monolayers of new family of 2D materials are studied. The high

cohesive energies and the non-existence of imaginary phonon modes confirm their stabilities. The Janus structures $XGeSiP_2As_2$ (X = Mo, W) with broken mirror symmetry indicate small direct band gaps, larger spin splittings at K/K' and the Rashba spin-splitting in comparison to pristine $MoSi_2P_4$. From the electronic and optical band gaps, it is recognized that these materials can be used in near- and mid- infrared detection applications.

1.1 Motivation of $InAs/InAs_{0.625}Sb_{0.375}$ 3D SL

Infra-red are electromagnetic radiations lying just below the red color of the visible spectrum. An IR detector is a device, which in general images, detects, and/or measures the patterns of thermal radiations emitted by all objects. In the start, the development of IR sensors/detectors was linked with those of thermal detectors, for instance the bolometers and thermocouples. These detectors were operated at room temperature, which could sense almost the whole infrared spectrum of wavelengths, and are widely used even today. The second type is the photon detectors, which are more developed in terms of sensitivity and their response time. So far, several class of materials have been utilized in the IR technology, such as Pb salt, extrinsic Ge (doped with Cu, Zn, Au), InSb, InAs and their alloys, IV−VI alloy ($Pb_{1-x}Sn_xTe$), II−VI ($Hg_{1-x}Cd_xTe$), and GaAs/AlGaAs superlattices (SLs). However, there are always some drawbacks as will be discussed in the coming sections of this chapter. The experiments of Sir Frederick William Herschel in 1800, to measure the temperature of each color in the electromagnetic spectrum lead to the discovery of IR radiations. After measuring the temperature individually for colors such as red, orange, yellow, green, blue and violet, he noticed that the temperature in the visible range decreases from red to violet, and vice versa. After noticing such a trend of temperature, Herschel performed other experiments for measuring the temperature after red part of the visible spectrum; region of no sunlight. Surprisingly, he observed the highest temperature for this region. Further experiments revealed that these radiations can reflect, refract, transmit, and absorb just like visible light. This invisible light just beyond the red portion of the visible region is now termed as infrared radiation [2-4]. Figure 1.1 shows the schematic of electromagnetic spectrum, where the spectral window for infrared region is divided into three sub-spectral ranges i.e. from 0.7 to 3 μm that lies near IR (NIR), from 3 to 5 μm mid-wave IR (MWIR), and from 8 to 30 μm as long-wave IR (LWIR)/far IR (FIR). For example, the range of thermal radiations emitted by ordinary objects and human bodies lie in the FIR spectral window. Therefore, the tracking of thermal objects can be feasible with the design of LWIR cameras.

The first thermocouple and electrical thermometer were designed in 1829 by L. Nobili with the discovery of thermoelectric effect (Seebeck in 1826). After four years, M. Melloni connected in series many bismuth−copper based thermocouples, which generated measurable and higher output voltage. He found the device almost 40 times sensitive with respect to the available thermometers at that time, which can sense a person's heat who is at 30 ft distance from the detector [5]. In 1880, Samuel Pierpont Langley invented a bolometer that looked like a Wheatstone bridge [6, 7]. With this instrument, he was able to study the solar radiations at different wavelengths and the irradiance

in the IR range [8-10]. Langley continues efforts of developing and improving his bolometer yielding the detector to be 400 times more sensitive, which could even sense the thermal heat of a cow that is a quarter mile away from the bolometer [8]. The first observation of photoemission was revealed by Hertz in 1887, when he noticed the emission of negatively charged entities from a conductor by irradiating it with the UV light [11]. Further experiments indicated that the effect is also possible with the visible light by using alkali metal [12]. Between the WW I and WWII, the image converters and photon detectors were developed, together with the infrared spectroscopy, which was considered as important analytical tool for the chemists. The image converter (designed just before the WW II) was of immense importance to military, since this instrument enabled the night vision in the darkness. Theodore W. Case developed the first infrared photoconductor in 1917 [13], where the photoconductivity for Tl_2S was exhibited. The system was able to send messages to about 18 miles in the environment known as smoky atmosphere. During 1930's, in the United States perhaps the crucial development in the IR technology was the Radio Corporation of America (RCA) IR image tube. The NIR cathodes during WW II were connected with visible phosphors that provided the image converter in NIR. After setting up the National Defense Research Committee, the tube was produced in large productions as RCA 1P25 image converter in 1942. In the WW II, this tube connected to 'Sniperscope' and 'Snooperscope' were extensively benefited for night vision. At the University of Berlin, Edgar W. Kutzscher in 1933 observed that PbS is photoconductive, which can response to 3 μm. In 1943, the photoconductors based on PbS were brought into productions in Germany. This was the first ever practical IR detector (bearing excellent range) used during the WW II for various applications [14].

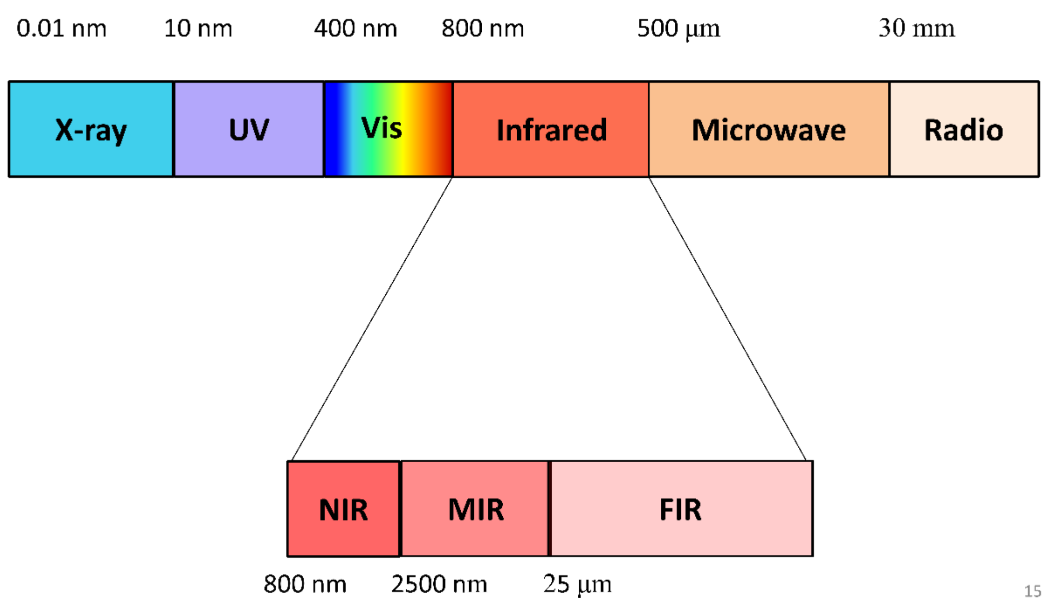

Figure 1.1 Electromagnetic spectrum increasing wavelength indicated from X-ray to radio, the infrared region is also zoomed with NIR, MWIR, and FIR shown.

In 1941, the thallous sulphide based detectors technology was improved by Robert J. Cashman leading to large production [15, 16]. After success, Cashman focused his studies on PbS based detectors. After WW II, he established that other semiconductors such as PbTe and PbSe can be used as infrared detectors [17]. It was only a matter of time before the military realized the benefits of night vision. At the end of World War II, IR technology for the military was still in its infancy. From the 1950s, passive night vision technology and the radiometric instruments were the key IR hardware developments, which enabled the vision in ambient starlight. After the war, the fire control, communications and the search systems strongly stimulated the lead salt detector technology development, which has continued even today. The IR systems, primarily for anti-air missile seekers, were constructed from cooled lead salt detectors [7]. For many applications in the spectral ranges 1-3 µm and 3-5 µm, the low-cost, adaptable PbS and PbSe polycrystalline thin films continue to be the preferred photoconductive detectors after 60 years. The focal plane arrays (FPAs) is the current lead salt development. Following the invention of the transistor, which greatly improved the growth and material purification procedures, extrinsic impurity based photoconductive detectors were reported in 1950s [18, 19]. These first extrinsic detectors were germanium based, since the methods for impurity introduction in a controlled manner were known by the time.

Devices operating in the range 8-14 µm spectral window as LWIR and 14-30 µm as VLWIR were made possible by the extrinsic photoconductive response of gold, copper, zinc, and mercury impurity levels in germanium. Before intrinsic detectors were developed, the extrinsic photoconductors were frequently utilized at wavelengths greater than 10 µm. However, in order to attain performance equivalent to that of intrinsic detectors, their operation at lower temperatures is required. The early 1960s saw the discovery of first extrinsic Hg-doped Ge as forward-looking IR detector, which operated in long wavelength region [20]. Ge:Hg with an activation energy of 0.09 eV was an excellent match for the LWIR range, however because the detection process relied on an external excitation, it needed a two-stage cooling mechanism to run it at 25 K. The first forward-looking IR system in actual production using Ge:Hg was constructed in 1969 for B52 Aircraft in the Air Force [21]. It produced very good imaging, but the two-stage cooling process had a short lifespan and required a lot of maintenance. In the start of 1950's, many advancements in the narrow bandgap semiconducting materials were made, which subsequently were proven to be highly sensitive together extended wavelength capabilities. InSb, a member of the III-V compound semiconductors, was the first such material. InSb attracted interest due to its narrow energy gap as well as the ease with which its single crystal can be produced using standard techniques. Moreover, the development of the semiconductor alloys of III-V ($InAs_{1-x}Sb_x$), II-VI ($Hg_{1-x}Cd_xTe$) and IV-VI ($Pb_{1-x}Sn_xTe$) material systems occurred at the end of 1950s and start of 1960s. These compositions made it possible to tune the spectral response for particular applications by manipulating the bandgap of materials. Variable band gapped alloys of $Hg_{1-x}Cd_xTe$ were first developed in 1959 by Lawson and colleagues [22]. They are practically perfect for a variety of IR detectors due to the fundamental characteristics of these narrow-gap semiconductors including the high electron mobility, high optical absorption coefficient and low thermal generation rate as well

as the ability to engineer bandgaps. Over the past 40 years, new detection technologies have been developed due to difficulties in the growth of HgCdTe, which are largely caused by the high vapour pressure of Hg. In the early 1970s and late 1960s, the PbSnTe was equally pursued [23, 24]. The growth of PbSnTe was relatively easier, and their demonstration as LWIR lasers and photodiodes is straightforward. Harman and Melngailis in 1974 [24], compared $Hg_{1-x}Cd_xTe$ and $Pb_{1-x}Sn_xTe$ systems as 'We predict that Pb_{1-x} Sn_xTe can be utilized extensively in future for detecting the blackbody radiations from 8 to 14 µm range, since the crystal growth is less expensive and more scalable for mass production. Furthermore, when compared to $Hg_{1-x}Cd_xTe$, the $Pb_{1-x}Sn_xTe$ seems to be more durable and much less degradable at high temperatures. $Hg_{1-x}Cd_xTe$, however, can be anticipated to be more advantageous in GHz frequency range for sensing heterodyne including some high-speed applications owing to its lower dielectric constant.' This perspective dramatically changed a few years later due to the chalcogenides' two major flaws. First, the high dielectric constant, which led to a high diode capacitance and consequently limiting frequency response [25]. Secondly, the extremely high thermal expansion coefficients (TEC) of IV–VI compounds [26], limiting their use for hybrid configurations with silicon multiplexers.

The advancement of material technology continuously focused on the military purposes. The Vietnam War in the US led to the development of the IR technology. When photolithography was made accessible in 1960s, the IR detector arrays were made. The linear array technology was employed for InSb, PbSe, and PbS detectors in the early stages. The first FIR forward-looking IR device was produced in 1969 by utilizing linear Ge:Hg arrays. The HgCdTe detector, in which optical transitions are related transitions from the valence band maximum (VBM) to conduction band minimum (CBM), was known at the time to be capable of achieving very good sensitivity at significantly higher temperatures, and many countries actively developed the HgCdTe based detectors [27]. In 2009, the 35th conference in Infrared Technology and Applications, which took place in Florida, scheduled a separate session for celebrating the HgCdTe's 50th anniversary. The capability of HgCdTe alloy to tune its band gap as proposed by Lawson and colleagues (in 1959) [22], has given IR detector technology a unique degree of freedom in their designs. Applications for IR detectors that cover NIR (1-3 µm), MIR (3-5 µm), long wavelength (LWIR: 8-14 µm), and FIR: 14-30 µm ranges are made possible due to its variable bandgap. The most popular variable gap semiconductor for IR photodetectors right now is HgCdTe, which successfully have gone through many challenges like lead-tin telluride and extrinsic silicon devices, although it has now more competitors. For instance the silicon-based Schottky barriers, heterojunctions of SiGe, GaInSb superlattices and AlGaAs quantum wells, high-temperature superconductors, and particularly there are two different kinds of thermal detectors (pyroelectric detectors and silicon-based bolometers). However, it is intriguing to note that none of these competed in terms of basic characteristics. However, it should be noted that the GaInSb type II superlattice could be very appealing from the physics perspective.

1.1.1 Alternatives to HgCdTe

Due to the difficulty in the synthesis of HgCdTe, particularly the high Hg vapour pressure and the solidus-liquidus separation, alternate technologies have been developed. Among them were PbSnTe [23, 24], strained $Ga_{1-x}In_xSb$ superlattices (8-14 µm range) [28], and a variety of quantum well infrared photodetectors (QWIPs) based on GaAs/AlGaAs [29-31]. InSb was found to have the narrowest energy gap as compared to other semiconductors during 1950s, that is why its use as a MIR detector was apparent. At higher working temperatures, the InSb band gap is less matched with 3-5 µm wavelength, and HgCdTe performs better. Similar to InSb in composition, the InAs has greater band gap with a threshold wavelength of 3-4 µm. The comparison of the dark currents for InSb and HgCdTe photodiodes suggests the better performance of HgCdTe based photodiodes. Due to the defect center in the energy band gap of InSb, the devices are influenced by generation-recombination currents. On other hand HgCdTe detector does not demonstrate any generation-recombination currents in the given temperature range and are instead constrained by the diffusion currents. Additionally, the HgCdTe has become the desired material because to its wavelength tunability [7]. A possible detector material for NIR range (1.0-1.7 µm) can be the alloy of $In_{0.53}Ga_{0.47}As$ with a lattice matching substrate of InP. The material can be used for applications like remote sensing, light wave communication systems, process control and the night vision due to the lower dark current and noise with respect to germanium, a competitor NIR material [32]. The photodiodes of InGaAs are shown to be of higher performance for materials with composition almost matching with InAs (cut–off wavelength of 3.6 µm) and InP (cut-off wavelength of 1.7 µm). However, the performance rapidly declines (at intermediate wavelengths) because of the defects induced by substrate lattice mismatch.

The QWIPs could be alternative hybrid detectors for the LWIR range i.e. 8-14 µm. The superlattices of GaAs/AlGaAs have been constructed to produce the high impedance detectors. The LWIR HgCdTe focal plane arrays continue to be expensive despite significant research and developments, principally due to the low yield obtained from operable arrays. The sensitivity of HgCdTe systems to defects is the cause of lower yield that occurs because of materials' fundamental properties. GaAs/AlGaAs QWIPs bear a number of benefits over HgCdTe devices, including the ability of using the standard manufacturing tools (MBE growth setup). This results in high yield and consequently lower cost with improved radiation hardness and thermal stability. Due to inherent constraints related to inter-subband transitions, LWIR QWIP cannot compete with HgCdTe photodiode as a single device, especially at higher temperatures (>70 K). The QWIP devices usually reveal low quantum efficiency and lower spectral response band. Due to many issues with HgCdTe material, for instance the Shockley-Read recombination, surface and interface instabilities, trap assisted tunneling and p-type doping, it has less distinct benefit below 50 K [30, 33].

The performance limitations for applications requiring quick integration times and the lower working temperatures are the key disadvantages of QWIP focal plane array technology. The large size focal plane arrays and the uniform performance are two key features of this technology. Due

to the widespread use of GaAs in telecommunication sector, there is a significant industrial infrastructure for the growth, packaging and processing of III-V materials and devices. Infrared detection is the only know application for HgCdTe . The lack of big size focal plane arrays required for TV format and larger formats is the major limitation in LWIR HgCdTe technology. Strain layer superlattices (SLSs) of InAs/$Ga_{1-x}In_xSb$ can be considered as one of the alternatives to HgCdTe. However, the InAs/GaInSb SLs are still in the process of development. There exist several problems including the substrate preparation, material growth, device passivation and processing. In a superlattice, the holes are located in one layer (GaInSb in this case), while electrons in the other (InAs) of the superlattice. This kind of bands alignment in the electronic structure categorizes the superlattice as type-II (see the schematic in Fig. 1.2). As a result, the carrier lifetime is increased and Auger recombination processes are suppressed. Over the last few years, InAs/In(As,Sb) Ga- and Hg free type-II superlattices (T2SLs) are widely investigated as promising candidates for IR applications due to their narrow electronic band gaps and carrier lifetimes longer compared to other systems [34-42].

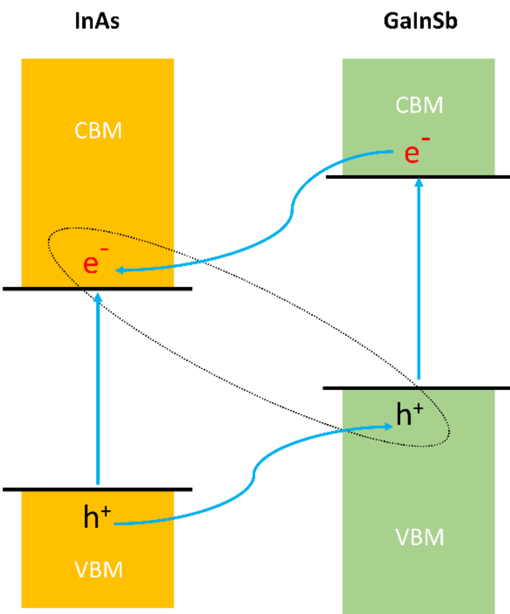

Figure 1.2 Schematic exhibiting the type-II band alignment; the electrons lie in InAs, while holes are located in GaInSb part of the superlattice.

1.2 Two-dimensional (2D) materials

The search continued on finding other materials with unique electronic and optical properties. Bulk materials just thinned to their single-layer limit may show extraordinary features due to the electron containment and their layered nature. Among these, 2D materials such as graphene and transition metal dichalcogenides (TMDs) are broadly investigated exhibiting unique electro-optical properties, which could be very promising in optoelectronic devices. There has been several

issues faced with the fabrication of the electronic devices based on bulk materials, a central drawback is their growth on flexible substrates. The discovery of 2D layered materials made it possible to design electronic devices on flexible substrates [43]. On the other side, the Moore's law scaling limit seems approaching, and thus narrowing the Si technology that is simply because of basic limitations in Si on atomic scale [44]. In view of the aforementioned drawbacks, it is intriguing to speculate about the position of 2D materials in electronics and nono-electronics.

The 2D materials has ignited the research for next generation photonic devices building the platform to different optoelectronic applications [45, 46], such as transparent electrodes [47, 48], fast photodetectors [49, 50], plasmonic devices [51], ultrafast lasers [52], and optical modulators [53]. 2D materials can be Dirac like gapless materials (graphene), insulators (hexagonal boron nitride, h-BN), semiconductors (TMDs e.g. WS_2, MoS_2 etc.), and narrow band gap materials (black phosphorus, bP) [54]. Hence, they can be found in different flavors as demonstrated in the schematic of Fig. 1.3. The most significant physical and chemical features for 2D materials are:

1) A quantum restriction that favors the 2D plane and is advantageous for the absorption of light and quantum devices.

2) Van der Waals forces, which weakly stack the atomic planes on top of one another making it easier to build heterostructures and providing the possibility to integrate these layered structures with silicon chips.

3) Nanodevices devoid of parasitic capacitance can be produced with atomically thin 2D materials.

4) Devices with extraordinary performance could be made possible due to the absence of dangling bonds at the surfaces and interfaces of layered structures.

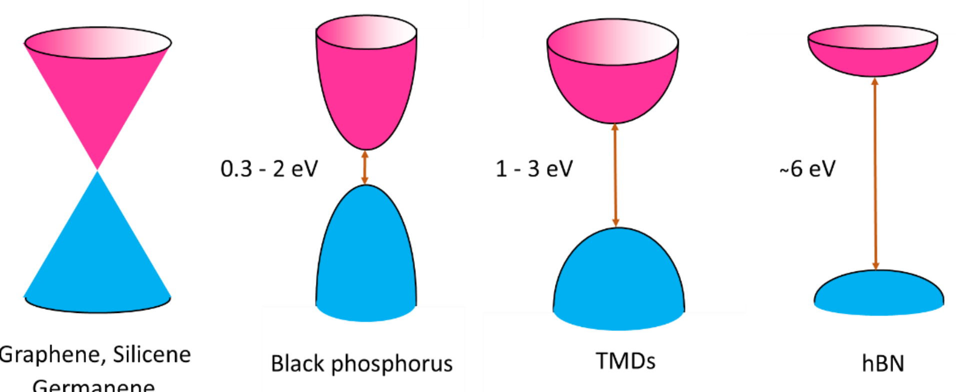

Figure 1.3 Illustration of bandgaps for different 2D materials. The true value of the bandgap is dependent on a number of factors such as the number of layers, chemical doping and strain level.

Since graphene has no gaps, there is a large dark current that significantly lowers photodetection's sensitivity and prevents future advancement in optoelectronics. The discovery and novel tools of growing 2D materials bearing direct energy band gaps that are tunable from visible region to IR spectral window have given an insight of manufacturing the photodetectors. Nicolosi et al. grouped the different 2D materials covering a wide spectral range of the optoelectronic properties as: atomically thin h-BN (UV region), TMDs (visible to IR), bP (layer dependent band gaps from visible to IR), metal halides (PbI_2, $MgBr_2$), metal oxides (MnO_2, MnO_3), and halide perovskites [55]. 2D TMDs have chemical formula as MX_2, where M represents transition metal (such as Mo, Hf, W, Nb, Re, etc.) while X stands for chalcogen atom (like Te, Se, S) [56]. The pair of X layers sandwich a single layer of M atoms. There are three polytypes of layered TMDs: 1T (trigonal), 2H (hexagonal), and 3R (rhombohedral), each of which has a unique set of electrical characteristics ranging from metallic to semiconducting and/or even superconducting [57]. Unlike graphene, whose electronic properties depends on the hybridization of 's' and 'p' orbitals, the electronic attributes of TMDs instead are dependent on the coordination environment and filling of 'd' orbitals of transition metal element. From group IV to X in periodic table, in a transition metal the d electrons varies from zero to six, correspondingly. A semiconducting behavior results from the fully filled d orbitals (2H-MoS_2 of group VI and 1T-PtS_2 of group X), whereas metallic nature is observed for the partially filled d states (2H-$NbSe_2$ of group V and 1T-ReS_2 from group VII). The electro-optical characteristics of TMDs are thickness dependent, i.e. on the number of layers and differ greatly from those of their bulk counterpart. Bulk materials of TMDs are known to be indirect band gap semiconductors with typical 1 eV bandgap. The band structure switches from a narrow indirect nature to a wide direct, as the bulk is thinned to monolayer. As a result, TMDs are able to detect light at various energies thereby modulating the electronic bandgap via changing the layers of TMDs. These variations in the optoelectronic properties occur due to the surface and quantum confinement effects [46, 50, 58-61]. Furthermore, the application of strain can also have a significant impact on the materials' optical and electrical characteristics [62, 63].

The optical absorption taking place in the spectral range from visible to near-infrared is mostly caused by the electron direct transition from valence to conduction band at K/K' points in 2D Brillouin zone. This explains why TMDs have absorption coefficient in the range 10^4-10^6 cm^{-1}, which is comparatively higher. Consequently, TMD films having sub-micron thickness absorb more than 95 % of electromagnetic radiations coming from the sun. TMDs, such as MoS_2, $MoSe_2$, and WS_2 demonstrate even better absorbance in the UV to NIR region than graphene. The region of absorbance can be broadened to MWIR region due to defect or edge states in the electronic band gap and comparatively higher ratio of edge-to-surface area [63]. It is necessary to use the layered semiconductors with low bandgaps and high mobilities for LWIR detector devices. The group-X noble TMDs, which have recently been revisited with broadly tweakable bandgaps, anisotropy, air stability, and moderate carrier mobility [64], offer such a possibility. Theoretically, the bandgaps for the bilayers and bulks of this class (PtX_2, where X=Se, S) might be as low as 0-0.25 eV, and the carrier mobility is found to be above 1000 cm^2/Vs at ambient temperature [65, 66]. TMD monolayers are regarded as promising materials for optoelectronics and could be ideal as the

channel layered materials FETs due to their inherent band gap of 1.1–1.9 eV [67-71]. Furthermore, the spin splitting in the range 150-500 meV at the corners (K, K' points) of the hexagonal Brillouin zone is caused by inversion symmetry breaking combined with spin-orbit interaction causing from the metal atoms' d orbitals of TMD monolayers [72-75]. TMDs are considered as typical valleytronic materials due to the strong coupling among the spin and valley degrees of freedom [76-78].

1.2.1 Hybrid 2D materials

The 2D TMDs due to their unique crystal structures and extraordinary physical properties are the materials of choice in applications such as electronics, photonics, valleytronics and optoelectronics [79-82]. However, integrating the 2D materials with other layered structures in the form of heterostructures and/or superlattices could be very promising. In particular, the 2D TMDs could be skillfully bring-together thereby fabricating various heterostructures or superlattices possessing exotic features, which cannot be acquired from the isolated component of the layered 2D material, thus providing the opportunities to explore and investigate the novel applications for the nanodevices [83-85]. In nanoelectronics and optoelectronics, the hybrid structures between different 2D materials could be very crucial building blocks because of their versatility and greater capacity [62, 86-90]. The mechanical exfoliation followed by the pick-up-and-transfer technique can be used to create 2D layered heterostructures, but chemical vapor deposition (CVD) enables the direct growth of TMDs layers that are lattice aligned for both the heterostructures i.e. Van der Waals vertical heterostructures and lateral heterostructures having sharp interfaces. Moreover, the monolayer TMD on a wide scale can be synthesized on large scale with seeding promoter-assisted-CVD. Based on the choice of seeding promoter and its capacity to adhere to substrates, this strategy was subsequently adapted for the construction of a range of vertical and lateral hybrid-structures. Besides, it is demonstrated that the technique is independent of lattice mismatch among the combining materials (2D and TMD) to create vertical or lateral heterostructures [91-93]. One-step or two-step CVD synthesis have both been used to effectively produce a number of lateral heterostructures, including MoS_2/WSe_2, NbS_2/MoS_2, $MoS_2/MoSe_2$, and $ReS_2/ReSe_2$, MoS_2/WS_2 (the top and side views for such structure are shown in Fig. 1.4b).

The laterally stitched and van der Waals heterostructures demonstrate abrupt change in their optoelectronic features due to their unique quality of interfaces and their distinctive electrostatics, and thus such heterostructures between the various 2D materials have recently attracted a lot of interest [92, 94-97]. The heterostructures of 2D materials are superior to bulk hetero-systems in that they have larger depletion region, and therefore are more sensitive to charge fluctuation [98, 99], making them perfect for optoelectronic applications [100, 101].

1.2.2 Janus structures

2D transition metal chalcogenides structures have undergone substantial research and found a wide range of uses in electronics and optoelectronics [70, 102-104]. The TMDs bearing the bandgaps

in the range of 1.1–1.9 eV with promising mechanical and electronic properties make them suitable to use these systems in photonics and electronic devices [69, 76, 105, 106]. At the corners of the hexagonal Brillouin zone of TMDs, there exist high spin splitting due to the absence of inversion symmetry, and significant spin-orbit coupling (SOC), which is produced by the d-orbitals of transition metals in TMDs [73-75]. Because of the strong correlation between the spin and valley degrees of freedom, the TMDs are regarded as the optimal materials in valleytronics [76-78]. Additionally, the alloy composition in TMDs, such as in $Mo_xW_{1-x}S_2$, MoS_xSe_{2-x}, and MoS_xSe_{2-x}, might be used to modify the electrical and optical characteristics [107-111]. Recently, the CVD approach has been used to successfully develop the Janus phase of MoSSe in the 2H phase [112, 113], where the S layer is replaced with Se atoms in the case of MoS_2, while the Se layer with S atoms in $MoSe_2$. In contrast to MX_2 (M=Mo, W, and X=S, Se), which has mirror symmetry, the Janus structure i.e. MXY (M=W, Mo, X=Se, S, and Y=S, Se) displays the out-of-plane piezoelectricity and Rashba-type spin splitting due to the perpendicular electric field that results from the breaking of mirror symmetry [72, 114-116]. Figure 1.4c shows the structures for pure and Janus phases of TMDs.

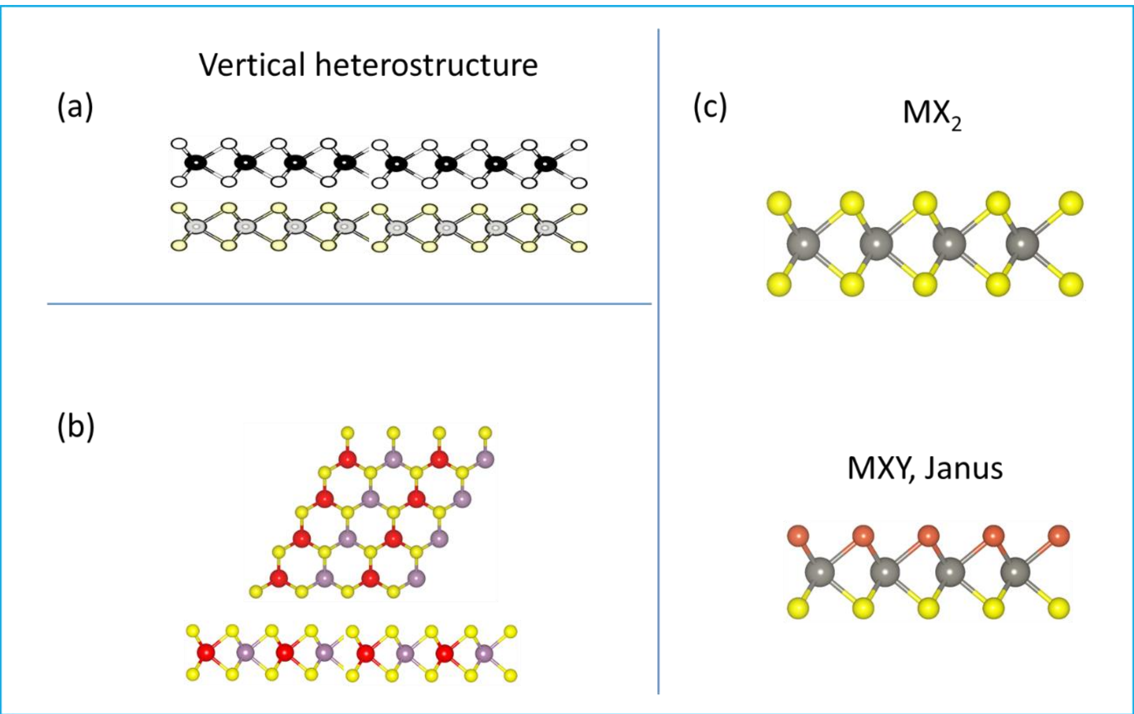

Figure 1.4 (a) Side view of vertically stacked heterostructure (b) Top and side views of parallel stitched 2D superlattice of MX_2 class, (c) representation of pristine (MX_2) and Janus structure (MXY).

1.3 MA_2Z_4 2D materials

Recently, a novel class of 2D materials MA_2Z_4, (where M represents a transition metal, A stands for group IV element, while Z is group V element) has received considerable attention owing to their exceptional properties [117]. The $MoSi_2N_4$ is first 2D material of this group, which was successfully grown using the CVD method over a big surface of 15 mm by 15 mm. This septuple-atomic-layer semiconducting material (N-Si-N-Mo-N-Si-N) may be viewed of as the three atom thick MoN_2 sandwiched between the two SiN layers with indirect band gap of about 1.94 eV. The elastic modulus of a monolayer of $MoSi_2N_4$ is about four times greater than that of a single layer of MoS_2, and the carrier mobilities of holes and electrons are correspondingly four to six times greater. Moreover, calculations using density functional theory predict the existence of a novel family called MA_2Z_4 (M is Transition metal, A is IV-element, and Z is V-element). The extraordinary attributes of this family have been the subject of several studies to date [118-125].

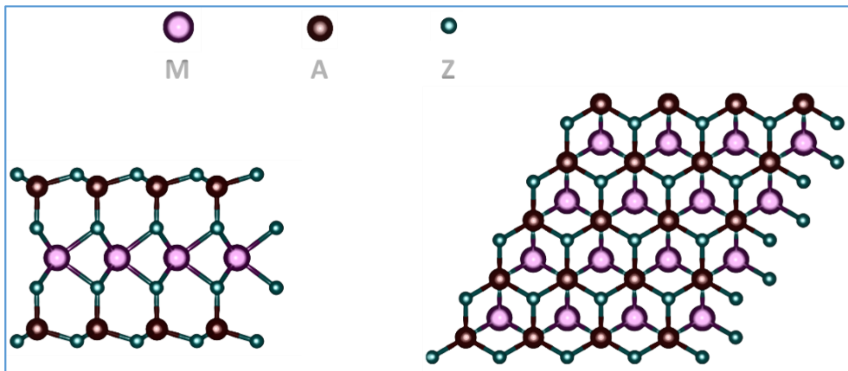

Figure 1.5 Side and top view of MA_2Z_4 family of 2D materials.

1.3 Thesis Outline

Using density functional theory (DFT), this thesis aims to address the electronic and optical properties of 3D $InAs/InAs_{0.625}Sb_{0.375}$ superlattice, XSi_2N_4 (Mo, W, Ti) 2D materials and their heterostructures $MoSi_2N_4/XSi_2N_4$ (W, Ti), and the pristine $MoSi_2P_4$ and Janus structures $XGeSiP_2As_2$ (X = Mo, W).

Chapter 2 is devoted to methodologies and computational details. First, the density functional theory is introduced, discuss different exchange–correlation functionals and the limitations of DFT. Then we review the nuts and bolts of DFT.

In **Chapter 3**, we give a brief overview of the main results compiled in this thesis along with the summaries of the papers attached. This thesis is the collection of four papers attached in this chapter. In paper I, the electronic and optical properties of the bulk InAs and InSb using modified Becke-Johnson (MBJ) exchange-correlation functional together with generalized gradient

approximation (GGA) for the exchange-correlation potential are discussed. After the validation of our approach, we studied the InAs/$InAs_{0.625}Sb_{0.375}$ SLs with three lattice constants of bulk InAs, GaSb and AlSb, respectively. In paper II, the structural stability and electronic properties of the monolayers of 2D materials such as $MoSi_2N_4$, WSi_2N_4, and $TiSi_2N_4$, and that of 2D heterostructures like $MoSi_2N_4$/WSi_2N_4, and $MoSi_2N_4$/$TiSi_2N_4$ are investigated. In paper III, the study is extended for the laterally stitched heterostructures, where the tuning of the electro-optical attributes via biaxial strain engineering is addressed. In paper IV, the electronic, spintronic and optical properties of pristine $MoSi_2P_4$ and Janus structures $XGeSiP_2As_2$ (X = Mo, W) for this new class of 2D materials are reported.

Finally, the last **Chapter 4** is dedicated to the conclusions.

Chapter 2

METHODOLOGY AND COMPUTATIONAL DETAILS

2.1 Many body electron system

Consider a scenario where you need to describe the properties of a clearly defined group of atoms, such as the atoms that make up a single molecule or the crystal structure of an intriguing material. The precise properties of a material can be approximated by taking into account every possible interaction, such as electron-electron, electron-nucleus, and nucleus-nucleus interactions. The following is a description of the Hamiltonian of a material with many-body interactions;

$$\hat{H} = \hat{T}_n + \hat{T}_e + \hat{V}_{n-n} + \hat{V}_{e-e} + \hat{V}_{n-e} \quad (2.1)$$

Where $\hat{T}_n$, $\hat{T}_e$ represent the system's nuclei and electrons' kinetic energies.

$$\hat{T}_n = \sum_{\alpha=1}^{K} \frac{(-i\hbar\nabla_{R\alpha})^2}{2M_\alpha}$$

$$\hat{T}_e = \sum_{\alpha=1}^{N} \frac{(-i\hbar\nabla_i)^2}{2m}$$

Here m is the mass of the electron in the N electron system and $R\alpha$ is the Cartesian coordinate of the nucleus with mass $M\alpha$. There are two types of Coulomb interactions that exist among the particles indicated in Eq. 2.1; the $\hat{V}_{n-e}$ potential which is between a nucleus and an electron (attraction), and $\hat{V}_{n-n}, \hat{V}_{e-e}$ represent the Coulomb repulsion potentials between the nuclei and electrons, respectively.

$$\hat{V}_{n-n} = \sum_{\alpha,\beta=1;\alpha<\beta}^{K} \frac{Z_\alpha Z_\beta e^2}{|\vec{R}_\alpha - \vec{R}_\beta|}$$

$$\hat{V}_{e-e} = \sum_{i,j=1;i<j}^{N} \frac{e^2}{|\vec{r}_i - \vec{r}_j|}$$

$$\hat{V}_{n-e} = -\sum_{\alpha=1}^{K} \sum_{i=1}^{N} \frac{Z_\alpha e^2}{|\vec{R}_\alpha - \vec{r}_i|}$$

where the ith and j[th] electrons are indicated by the letters r_i and r_j. A many-electron system's Hamiltonian may be expressed as

$$\hat{H} = \sum_{\alpha=1}^{K} \frac{(-i\hbar\nabla_{R\alpha})^2}{2M_\alpha} + \sum_{\alpha=1}^{N} \frac{(-i\hbar\nabla_i)^2}{2m} + \sum_{\alpha,\beta=1;\alpha<\beta}^{K} \frac{Z_\alpha Z_\beta e^2}{|\vec{R}_\alpha - \vec{R}_\beta|} + \sum_{i,j=1;i<j}^{N} \frac{e^2}{|\vec{r}_i - \vec{r}_j|} - \sum_{\alpha=1}^{K} \sum_{i=1}^{N} \frac{Z_\alpha e^2}{|\vec{R}_\alpha - \vec{r}_i|} \quad (2.2)$$

One may solve the time-independent Schrödinger equation to determine the electronic characteristics of a many-electron system by taking into account all of the Hamiltonian's terms in Eq. 2.2.

$$\hat{H}\Psi = E\Psi \quad (2.3)$$

'Ψ' represents the eigenstates or a set of solutions of the Hamiltonian with the associate eigenvalues Ethat is a real quantity. Since there are 10^{23} times more ions and electrons in actual systems, it is challenging to find a precise solution to the equation with current computational resources. Approximations are necessary to solve this problem.

We must determine the locations of both the electrons and nuclei in order to find the location of an atom. Atomic nuclei are significantly heavier than individual electrons; in a nucleus each proton or neutron is more than 1800 times heavier than the mass of an electron. This is an important finding for applying quantum mechanics to atoms, which basically indicates that electrons react to changes in their environment considerably faster than those of nuclei. Thus, we can divide our physical query into two parts. First, the equations describing the many electron system are solved for fixed locations of the atomic nuclei. We determine the lowest energy configuration, or state, of the electrons for a specific set of electrons travelling in the field of a particular set of nuclei. This lowest or minimum energy configuration is termed as the ground state of system, and the formalism that separates the nuclei and electrons in the separate mathematical schemes is known as the Born Oppenheimer approximation. The Born Oppenheimer approximation, the first and most significant approximation, allows one to separate the motion of the electrons and ions, because in a typical solid ions travel far more slowly than electrons do. This approach assumes that the potential energy of ions is constant and the kinetic energy of ions is ignored. Hamiltonian therefore becomes;

$$\hat{H} = \sum_{i=1}^{N} \frac{(-i\hbar\nabla_i)^2}{2m} + \sum_{i,j=1;i<j}^{N} \frac{e^2}{|\vec{r}_i - \vec{r}_j|} - \sum_{\alpha=1}^{K}\sum_{i=1}^{N} \frac{Z_\alpha e^2}{|\vec{R}_\alpha - \vec{r}_i|} \tag{2.4}$$

This approximation allows us to decouple the wave function that may be expressed as the product of the ionic and electronic wave functions i.e.

$$\Psi = \Psi_{ik}^{n}(\vec{R}_\alpha)\, \Psi_k^e(\vec{r}_i\,,\ \vec{R}_\alpha) \tag{2.5}$$

The details of Hamiltonian are dependent on the state and situation of the physical system that the Schrödinger equation describes. There are several well-known instances where the Hamiltonian has a simple form and the Schrödinger equation can precisely be solved, such as particle in a box problem and that of harmonic oscillator. The problem we are dealing with is a more complex scenario when several electrons are interacting with numerous nuclei. Therefore, the Schrödinger eq. by taking into account the Born-Oppenheimer approximation is expressed as;

$$[\hat{T}_e + \hat{V}_{e-e} + \hat{V}_{n-e}]\, \Psi_k^e(\vec{r}_i\,,\ \vec{R}_\alpha) = E_k\,(R-\alpha)\, \Psi_k^e(\vec{r}_i\,,\ \vec{R}_\alpha) \tag{2.6}$$

For a set of frozen ions situated at $\vec{R}_\alpha$, the eigenvalue problem represented by Eq. 2.6 is stationary. Solving Eq. 2.6 is a difficult task due to many reasons, for instance, (i) the many meta-stable state arrangements for nuclei, (ii) intricate geometry of many body (many electrons) systems, and (iii) the enormous number of the electrons and their quantum nature. Therefore, even if the ion mobility is neglected, a more effective approximation is required to solve this problem. For that reason, we now discuss Hartree-Fock (HF) formalism, which is also called self consistent field approximation. In this approach, the ground state for a many electron system Ψ_0^e is exemplified by the product of single particle states termed as Slater determinants.

$$\Psi_0^e(\vec{r}_i\,\sigma_1, \ldots\ldots \vec{r}_N\,\sigma_N) \approx \phi_{1\ldots\ldots N}\,(\vec{r}_i\,\sigma_1, \ldots\ldots \vec{r}_N\,\sigma_N) \tag{2.7}$$

Where, ϕ_i stand for single electron wave functions with the spins denoted as σ_i, and the $\phi_{1\ldots N}$ representing the ground state wave of functions are obtained using the variational principle. One can notice that the HF scheme is analogous to the usual Schrödinger eq., where the effective potential shows a non local nature through the terms $V_H(r)$ (Hartree Coulomb potential) and V_x^{HF} (the exchange potential).

$$\left[\frac{(-i\hbar\nabla_i)^2}{2m} + V_H(r) + V_x^{HF}\right] \phi_i(\vec{r},\sigma) = E_i \phi_i(\vec{r},\sigma) \tag{2.8}$$

While $V_H(r)$ and V_x^{HF} are given as;

$$V_H(r) = \int \frac{d^3r'}{|\vec{r} - \vec{r}'|} \sum_{\sigma'=\uparrow,\downarrow} \sum_{j\neq i} \left|\phi_j\left(\vec{r}', \sigma'\right)\right|^2$$

$$V_x^{HF}(\vec{r}\sigma, \vec{r}'\sigma') = \frac{e^2}{|\vec{r}-\vec{r}'|} \sum_{j=1}^{N} \phi_j(\vec{r}\sigma)\phi^*{}_j(\vec{r}'\sigma')$$

The potentials are calculated self consistently; it starts with an initial guess, the potential and the ϕ_i states are improved step by step. Once a certain level of precision is attained, the iterative procedure is terminated. In the HF approach the electron-electron Coulomb repulsions are not taken into account and the wavefunction of N-electrons is approximated by the average field of the whole electron cloud. In order to take into account the Coulomb repulsion, the unoccupied states (finite or infinite) must be included together with the occupied states. The improved correlated wave function is given by;

$$\Psi_k(\vec{r}_1\, \sigma_1, \ldots\ldots \vec{r}_N\, \sigma_N) = \sum_{i_1 \ldots\ldots i_N} C^k_{i_1 \ldots\ldots i_N}\ \ \phi_{i_1 \ldots\ldots i_N}\,(\vec{r}_1\, \sigma_1, \ldots\ldots \vec{r}_N\, \sigma_N) \quad (2.9)$$

The expansion coefficient is calculated in a number of ways. The single electron wave functions $\phi_{i_1 \ldots\ldots i_N}$ should be expanded in a finite set of basis functions for efficient numerical implementations.

$$\phi_i(\vec{r}\sigma) = \sum_{k=1}^{M} b_{i,k\sigma}\, \eta_k(\vec{r}) \quad (2.10)$$

With the matrix elements $< \eta_k | \eta_l >$, Eq. (2.8) becomes an eigenvalue problem, the $b_{i,k\sigma}$ are determined simultaneously. Thus using the HF method, an effective single particle formalism is written as;

$$\sum_{l=1}^{M} \sum_{\sigma'} [\langle\, \eta_k \left| -\frac{(-i\hbar\nabla_i)^2}{2m} \delta_{\sigma,\sigma'} + v_{eff}\, \sigma, \sigma' \right| \eta_l \rangle - \ \epsilon_i \langle\, \eta_k | \eta_l \rangle]\, b_{i,l\sigma'} = 0 \quad (2.11)$$

Here, the potential experienced by the electrons is $v_{eff}\, \sigma, \sigma'$.

There are always searches for alternative approaches that can fully map the interactive many-body problem onto an effective single particle problem. Such an approach should include the correlations in some fashion to make it applicable for approximating the properties of a system precisely. One such scheme is the density functional theory (DFT), which is a remarkable method, which simply replaces the wave function concept with the electron density (ρ).

2.2 Density functional theory (DFT)

The fundamental concept of Density functional theory is the electronic density (ρ) that replaces the idea of wave function representing the many-body arrangement. As a result, the number of

scaling factors in the numerical algorithm is reduced. The ground state electronic density can be expressed as;

$$\rho(\vec{r}) = \langle \Psi_0 | \hat{\rho}(\vec{r}) | \Psi_0 \rangle$$

$$= N \sum_{\sigma_1, \ldots\ldots \sigma_N} \int d^3r_2 \ldots\ldots d^3r_N \, |(\vec{r}_1\, \sigma_1, \ldots\ldots \vec{r}_N\, \sigma_N)\, |\Psi_0 >|^2 \quad (2.12)$$

Two key mathematical theorems established by Kohn and Hohenberg, as well as a series of equations derived by Kohn and Sham in the mid-1960s, provide the foundation of the whole area of density functional theory. The first theorem is that '*the ground-state energy derived from Schrödinger's equation is a unique functional of the electron density, i.e. E=E[ρ(r)]*' as demonstrated by Hohenberg and Kohn, with ρ(r) as the electron density. This is the reason why this discipline is called density functional theory. This theorem can also be stated as *'The ground-state electron density is the only determinant of all ground-state features, including the energy and wave function, according to Hohenberg and Kohn.'* An essential characteristic of the functional is defined by the second Hohenberg-Kohn theorem: *'The actual electron density corresponding to the complete solution of the Schrödinger equation is the one that minimizes the energy of the overall functional.'*

2.2.1 Kohn-Sham equations

Unfortunately, the Hohenberg-Kohn (HK) theorem does not define the exact form of E[ρ(r)]. An accurate mapping of the interacting N-particle problem onto an effective non-interacting system can simplify the problem in question, which is feasible within the Kohn-Sham (KS) formalism. The single particle orbitals in the KS-scheme are referred to as KS orbitals ($\Psi_i^{KS}(\vec{r})$), which mimic the density of the real system.

$$\rho(\vec{r}) = \sum_{i=1}^{N} \left|\Psi_i^{KS}(\vec{r})\right|^2 \quad (2.13)$$

$\Psi_i^{KS}(\vec{r})$ follow the KS eq.

$$[-\frac{(-i\hbar\nabla_i)^2}{2m}\delta_{\sigma,\sigma'} + V_{eff}^{[\rho]}(\vec{r})]\Psi_i^{KS}(\vec{r}) = E_i \Psi_i^{KS}(\vec{r}) \quad (2.14)$$

Here, $V_{eff}^{[\rho]}(\vec{r})$ is the effective potential that is function of density 'ρ' of electrons and E_i denote the KS eigenvalues. The $V_{eff}^{[\rho]}(\vec{r})$ is rewritten as;

$$V_{eff}^{[\rho]}(\vec{r}) = V_{ext}^{[\rho]}(\vec{r}) + V_H^{[\rho]}(\vec{r}) + V_{XC}^{[\rho]}(\vec{r}) \quad (2.15)$$

$V_{ext}^{[\rho]}(\vec{r})$ represent the external potential which is given as;

$$V_{ext}^{[\rho]}(\vec{r}) = \int d^3 r v_{ext}\, \rho(\vec{r}) \tag{2.16}$$

$V_H^{[\rho]}(\vec{r})$ is the density-dependent classical (Hartree) interaction between the N particles

$$V_H^{[\rho]}(\vec{r}) = \frac{1}{2}\int d^3 r \int d^3 r' \frac{\rho(\vec{r})\,\rho(\vec{r}')}{|\vec{r}-\vec{r}'|} \tag{2.17}$$

$V_{XC}^{[\rho]}(\vec{r})$ stands for the exchange–correlation functional, that includes all quantum mechanical effects.

$$V_{XC}^{[\rho]}(\vec{r}) = \frac{\delta E_{XC}[\rho]}{\delta\rho(\vec{r})} \tag{2.18}$$

Here, $E_{XC}[\rho]$ stands for the exchange-correlation functional of total energy, which takes into account all possible interactions of many-body problem. Although the precise form of $E_{XC}[\rho]$ is not known, since it depends on electron density, it might be reliably predicted self consistently. If the precise form of $V_{XC}^{[\rho]}(\vec{r})$ is calculated, the Kohn-Sham equation can calculate the exact ground state energy. It is difficult to determine and computationally expensive to compute the precise shape of the exchange-correlation term of a many electron system. In the following, we discuss some approaches of approximation for $E_{XC}[\rho]$.

In general, the exchange correlation potential $E_{XC}[\rho]$ is composed of two contributions; one is the Exchange part $E_C[\rho]$, and the other is the correlation part $E_X[\rho]$ in the many-body problem. There are different approximation functionals to calculate $E_{XC}[\rho]$, two of these are well-known approximations known as the local density approximation (LDA), and the other is called general gradient approximation (GGA).

2.2.2 Local density approximation (LDA)

The Hohenberg-Kohn theorem guarantees the existence of exchange-correlation functionals, but it is simply unknown what their exact form is. Fortunately, the uniform electron gas is one instance where this functional can precisely be deduced. In this case, the electron density is $\rho(r)$ is constant in the whole space. Since the variation in electron density $\rho(r)$ form chemical bonds and in general make materials interesting, this scenario could seem to be of little relevance in any actual material. However, the uniform electron gas offers a useful application for the Kohn-Sham equations. To do this, we set the known exchange-correlation potential at each point to equal the electron density measured at that position of the uniform electron gas. This approximation is known as the local density approximation (LDA) because it only employs the local density to approximate the exchange-correlation functional. LDA is the foundation of all exchange correlation functionals. The electron gas is supposed to have a slowly fluctuating density. Subsequently, the exchange correlation energy remain locally uniform at small volume d^3r. Then, the $E_{XC}[\rho]$ within the LDA formalism is given as;

$$E_{XC}[\rho] = \int \rho(\vec{r})\epsilon_{XC}[\rho(\vec{r})]d^3r \qquad (2.19)$$

Where $E_{XC}[\rho]$ denotes the exchange relation energy for the density ρ(r) of uniform electron gas.

2.2.3 Generalized gradient approximation (GGA)

A generalized gradient approximation is considered to be the best-known functional after LDA, which not only makes use of the information of the local electron density, but also considers the local gradient in the electron density. It is easy to assume that the GGA must be more accurate because it contains more physical data than the LDA. There are several diverse GGA functionals due to the numerous ways in which information from the gradient of the density ρ(r) may be included. The Perdew-Wang functional (PW91) and the Perdew-Burke-Ernzerhof (PBE) functional are two of the most often employed functionals in DFT involving solids. These functions are all GGA functions. In our calculations, we used the PBE approach in the framework of GGA to treat electron exchange–correlations [126, 127]. When GGA is applied to systems with homogenous electron densities, this approximation performs rather well and produces comparatively better results for the metals. Unfortunately, it significantly underestimates the band gap in semiconductors. When compared to LDA, the GGA approximation takes into consideration the first order correction of the electron density ρ(r). Consequently, it includes the impact of the electron density's local inhomogeneity. Using GGA, the total exchange correlation energy can be expressed as:

$$E_{XC}[\rho(\vec{r})] = \int \rho(\vec{r})\epsilon_{XC}[\rho(\vec{r}), \nabla\rho(\vec{r})]d^3r \qquad (2.20)$$

2.2.4 Other exchange-correlation functionals

DFT employs a number of techniques to help with band gap issues and the materials' electronic structure, including the LDA+U, GGA+U scheme, meta-GGA functional scheme, van der Waals correction (vdW) strategy, different hybrid functional like HSE, and GW. In this this, we utilized the GGA, MBJGGA, and HSE functionals for the computations in 3D, 2D superlattices and Janus structures. The most common approach to employing a plane-wave basis set to solve the Kohn-Sham equation with the pseudopotential is described in the next section.

2.2.5 Plane wave basis set

In this thesis, we will emphasize in applying DFT to materials that are periodic in space (e.g. crystalline materials). We used the lattice vectors a_1, a_2, and a_3 to determine the geometry of the supercell, a cell that repeats itself repeatedly in space. The solution of the Schrödinger equation for a periodic system should satisfy the Bloch's theorem, a basic requirement. This follows;

$$\Psi_{ik}(\vec{r}) = e^{\vec{k}.\vec{r}}\, u_{ik}(\vec{r}), \qquad u_{ik}(\vec{r}+\vec{R}) = u_{ik}(\vec{r}) \qquad (2.21)$$

where $u_{ik}(\vec{r})$ exhibits the same periodicity as the supercell in space, with the lattice vector $\vec{R}$. According to this theorem, it is conceivable to attempt to independently solve the Schrödinger equation for each value of k. This conclusion is valid for quantities that are derived from the solutions of Schrödinger equation, such as the electron density. As a consequence, solving the mathematical problems raised by DFT in k-space (momentum space) is often far more practical than solving them in real space. Calculations based on this concept are usually referred to as 'plane-wave calculations' since the functions $e^{\vec{k}.\vec{r}}$ represent plane waves. In a plane wave basis set with a periodic condition, the Bloch wave function $\Psi_{ik}(\vec{r})$ may be expanded as;

$$\Psi_{ik}(\vec{r}) = \sum_{G} C_{i,k}^{\vec{G}} e^{i(\vec{k}+\vec{G})} \tag{2.22}$$

In this case, $C_{i,k}^{\vec{G}}$ is the expansion coefficient, and G is the reciprocal lattice vector. To increase computing efficiency, the sum should be limited to an ideal number of plane waves rather of the infinite number that exists in reality. With origin at the center, all the G vectors in a sphere with a radius of $|\vec{G}_{max}|$ are considered. The following eq. is used to determine the $|\vec{G}_{max}|$ from the kinetic energy cut off (E_{cut}).

$$E_{cut} = \frac{\hbar^2 |\vec{k} + \vec{G}_{max}|^2}{2m} \tag{2.23}$$

2.2.6 Pseudopotential

The orthogonality requirement between the valence electron wave function and the core electron wave function must be satisfied. Because of the rapid oscillations of wavefunction closer to the core of atoms, the energy scale spanned by the core electrons differs significantly from that of the valence electrons. As a result, Eq. requires a high number of plane waves to accurately characterize the valence electron wave function. However, the characteristics of solids are not significantly influenced by the core electrons. Because of this, an effective method known as the pseudopotential approach can be used in place of the real potential. Chemical bonding and other physical properties of materials are mostly determined by the less firmly coupled valence electrons; core electrons are not very significant in determining these properties. It was obvious from the first plane-wave procedure that calculations which mimicked the characteristics of core electrons in a way might decrease the number of plane waves necessary in a calculation may have considerable advantages. The usage of pseudopotentials is the most crucial strategy for lowering the computational burden caused by core electrons. Conceptually, a pseudopotential substitutes a smoothed density chosen to correspond to several significant physical and mathematical characteristics of the real ion core for the electron density from a selected set of core electrons. One such approach is the projector augmented-wave (PAW) method that was first introduced by Blöchl, later remodeled for plane-wave calculations by Joubert and Kresse. Materials possessing large electronegativity differences and strong magnetic moments, the PAW formalism is found to

be more reliable compared to other approaches. In this thesis, all the calculations are performed using PAW method that is built-in to VASP code.

Let's assume that the Kohn-Sham equation is satisfied by the system's real wave function;

$$\left[-\frac{(\hbar\nabla_i)^2}{2m} + V_{eff}^{[\rho]}(\vec{r})\right] \Psi_i^{KS}(\vec{r}) = E_i \Psi_i^{KS}(\vec{r}) \tag{2.24}$$

A pseudo wave function may be constructed as;

$$\Psi_i^{KS}(\vec{r}) = (1 - \hat{P})\phi_i(\vec{r}) \tag{2.25}$$

where the $\hat{P}$ signifies the projection operation that is expressed as follows;

$$\hat{P} = \sum_j |k_j >< k_j| \tag{2.26}$$

Any function can be projected by the $\hat{P}$ here to the core states ($| k_j >$). It may be demonstrated that $\Psi_i(r)$ can satisfy the equation as $\Psi_i^{KS}(r)$.

$$\left[-\frac{(\hbar\nabla_i)^2}{2m} + V_{ps}(\hat{r})\right] \phi_i(\hat{r}) = E_i\ \phi_i(\hat{r}) \tag{2.27}$$

Here, $V_{ps}(\hat{r})$ is the pseudopotential and it can be expressed as;

$$V_{ps}(\hat{r}) = V_{eff}^{[\rho]}(\vec{r}) - \left[-\frac{(\hbar\nabla_i)^2}{2m} + V_{eff}^{[\rho]}(\vec{r})\right] \hat{P} + E_i \hat{P} \tag{2.28}$$

Chapter 3

PAPERS COMPRISING THE THESIS

3.1 A short overview of the main results

Dimensionality of materials have revealed important impacts on their attributes. In addition to referring to the materials' structural characteristics, this also affects many of their electronic and optical properties [128]. To this end, we first investigate the electronic and optical features of InAs and InSb bulk, and then those of $InAs/InAs_{0.625}Sb_{0.375}$ 3D superlattice via first principles approach. We observed that the electronic and optical properties are modified remarkably in the superlattice geometry. A strong dependence of the electronic and optical features on the variation of lattice constant is observed. A considerable decrease in the effective masses for heavy-holes and energy gaps in the k_x-k_y plane is noticed as compare to their bulk phases of the parent compounds. The absorption spectra in the far-infrared regime is strongly increased in the case of superlattice with respect to bulk InAs and InSb suggesting their applications in the long-wavelength IR detectors. Moreover, a great deal of interest in 2D materials has been sparked by the successful "isolation" of graphene from the bulk graphite and the findings of its extraordinary physical features, such as ultrahigh electron mobility, ballistic carrier transport, and anomalous quantum Hall effect [129, 130]. Here, inspired from the excellent features of the newly discovered 2D materials family MA_2Z_4, we explore the monolayers XSi_2N_4 (X = Mo, W, and Ti) and the vertical and lateral heterostructures of these structures including $MoSi_2N_4/WSi_2N_4$, and $MoSi_2N_4/TiSi_2N_4$. After establishing the thermodynamical stability of both, the monolayers and heterostructures, we studied the electronic band structures and the density of states indicating a semiconducting behavior with the band gaps ranging from 0.30 to 2.60 eV giving the possibility to utilize them for photovoltaics and other photonic devices operating in the visible range (IR detectors). Besides, we investigated the effect of biaxial strain on the electro-optical properties of laterally stitched heterostructures, which revealed significant modifications in the electronic band structures and optical spectra. Lastly, the pristine $MoSi_2P_4$ and Janus phase such as $XGeSiP_2As_2$ (X = Mo, W) are studied in detail presenting outstanding thermodynamical stabilities. Comparing to pristine $MoSi_2P_4$, the Janus structures $XGeSiP_2As_2$ (X = Mo, W) possessing broken mirror symmetry indicate small direct band gaps, larger spin splittings at K/K' and the Rashba spin-splitting. The

large spin and Rashba-type splittings together with the exceptional electronic and optical features in the Janus structures can make extraordinary contribution in the valleytronics, spintronics and IR applications.

3.2 PAPER I: InAs/$InAs_{0.625}Sb_{0.375}$ 3D Superlattice

Owing to the small band gaps and longer carrier lifetime, the Ga- and Hg-free type-II superlattices (T2SLs) of InAs/(InAsSb) have gained attention as viable options for infrared detector applications during the past several years [7, 34, 36-39, 41, 131]. Besides, the In(As,Sb) based quantum wells and their nanowires are suggested as a platform to observe the topological superconductivity [132], whereas the InAs/GaSb heterostructures due to their type-III band bending have been reported to host topological states [133-135]. Generally, electronic band structures for III-V semiconductors are investigated within the tight-binding approximation or using the envelope function *k.p* formalism [7]. Such empirical approaches are successful while describing conduction band, yet fails for the valence band representing the heavy-hole. The failure of these methods is due to the fact that these approaches do not take into account the curvature and anisotropy of the remote bands. In this chapter, based on first-principle method, the electronic band structures and optical spectra of bulk In(As,Sb) and that of InAs/$InAs_{0.625}Sb_{0.375}$ SLs are explored with the lattice constants of bulk InAs, GaSb and AlSb, respectively. The results manifest higher absorption coefficients for SLs with respect to bulk counterpart, which reconfirms the dominance of the 3D SLs in detector applications. Further, the effective masses computed for heavy-holes in the k_x-k_y plane are reduced in the case of superlattice, which suggest that III-V SLs could possibly replace IV-VI materials as efficient Pb-free infrared detectors. The InAs and InSb are the III-V zinc-blende compounds with semiconducting behavior. For these compounds and alloys, the growth of heterostructures and superlattices is possible, wherein through alloy composition, thickness, and the interface chemistry one can modulate the electronic band gaps and their bandwidths [136]. There exists type-II band alignment in InAs/In(As,Sb) SLs, where the electrons are found in InAs part, while the holes are confined in the In(As,Sb) layers, indicating that electrons and holes are separated spatially. Consequently, with the adjustment of InAs thickness or that of In(As,Sb) or the concentration of Sb, the band gap can be tuned for a broad range of infrared detecting region. Due to these characteristics, we have chosen the T2SLs of InAs/In(As,Sb) for far-infrared applications. To this end, we first perform the DFT calculations using spin-orbit coupling and modified Becke-Johnson (MBJ), for the bulk In(As,Sb) and then consider a large 3D superlattice. On top of this, the optical properties are calculated, making our approach quite demanding from computational perspective.

OPEN ACCESS
IOP Publishing
Journal of Physics D: Applied Physics
J. Phys. D: Appl. Phys. 55 (2022) 495301 (10pp)
https://doi.org/10.1088/1361-6463/ac984d

Electronic and optical properties of $InAs/InAs_{0.625}Sb_{0.375}$ superlattices and their application for far-infrared detectors

Ghulam Hussain[1,*], Giuseppe Cuono[1,*], Rajibul Islam[1], Artur Trajnerowicz[2], Jarosław Jureńczyk[2], Carmine Autieri[1,3,*] and Tomasz Dietl[1,4]

[1] International Research Centre MagTop, Institute of Physics, Polish Academy of Sciences, Aleja Lotników 32/46, PL-02668 Warsaw, Poland
[2] VIGO System S.A., 129/133 Poznanska Str., 05-850 Ozarow Mazowiecki, Poland
[3] Consiglio Nazionale delle Ricerche CNR-SPIN, UOS Salerno, I-84084 Fisciano (Salerno), Italy
[4] WPI-Advanced Institute for Materials Research, Tohoku University, Sendai 980-8577, Japan

E-mail: ghussain@magtop.ifpan.edu.pl, gcuono@magtop.ifpan.edu.pl and autieri@magtop.ifpan.edu.pl

Received 1 May 2022, revised 18 September 2022
Accepted for publication 7 October 2022
Published 19 October 2022

Abstract

We calculate the electronic and optical properties of $InAs/InAs_{0.625}Sb_{0.375}$ superlattices (SLs) within relativistic density functional theory. To have a good description of the electronic and optical properties, the modified Becke–Johnson exchange-correlation functional is employed to describe the band gaps correctly. First, we analyze the electronic and optical characteristics of bulk InAs and InSb, and then we investigate the $InAs/InAs_{0.625}Sb_{0.375}$ SL. The optical gaps deduced from the imaginary part of the dielectric function are associated with the characteristic interband transitions. We investigate the electronic and optical properties of the $InAs/InAs_{0.625}Sb_{0.375}$ SL with three lattice constants of the bulk InAs, GaSb and AlSb, respectively. It is observed that the electronic and optical properties strongly depend on the lattice constant. Our results support the presence of two heavy-hole bands with increasing in-plane effective mass as we go far from the Fermi level. We notice a considerable decrease in the energy gaps and the effective masses of the heavy-holes in the k_x–k_y plane compared to the bulk phases of the parent compounds. We demonstrate that the electrons are *s*-orbitals delocalized in the entire SL, while the holes have mainly *p*-Sb character localized in the In(As,Sb) side of the SL. In the SL, the low-frequency absorption spectra greatly increase when the electric field is polarized orthogonal to the growth axis allowing the applicability of III–V compounds for the long-wavelength infrared detectors.

* Authors to whom any correspondence should be addressed.

Original Content from this work may be used under the terms of the Creative Commons Attribution 4.0 licence. Any further distribution of this work must maintain attribution to the author(s) and the title of the work, journal citation and DOI.

Supplementary material for this article is available online

Keywords: infrared detectors, optical properties, type-II superlattices

(Some figures may appear in colour only in the online journal)

1. Introduction

Over the last few years, InAs/In(As,Sb) Ga- and Hg-free type-II superlattices (T2SLs) have attracted attention as promising candidates for infrared (IR) detector applications due to their narrow gaps and carrier lifetime longer than those in other systems [1–9]. Furthermore, In(As,Sb) quantum wells and nanowires have been proposed as a platform for topological superconductivity [10] while the InAs/GaSb heterostructures host topological states due to their type III band bending [11–13]. Typically, the band structure of these compounds is studied by the envelope function $\boldsymbol{k} \cdot \boldsymbol{p}$ formalism or within tight-binding approximation [2]. These empirical methods are successful in describing the conduction band but often fail in the case of the heavy-hole valence band, whose curvature and anisotropy are determined by remote bands not considered usually within effective Hamiltonian methods. In this paper, we determine, by a first-principle method, band structures and optical properties of bulk In(As,Sb) and $InAs/InAs_{0.625}Sb_{0.375}$ SLs with lattice constants of InAs, GaSb and AlSb, respectively. Our results show that the absorption coefficient of SLs is larger than that of bulk materials, reconfirming the superiority of SLs for detector applications. We demonstrate also that the effective mass of heavy-holes in the k_x–k_y plane is much reduced in SLs indicating that III–V SLs might replace IV–VI compounds as efficient Pb-free IR emitters.

The InAs and InSb bulk compounds belong to the family of the III–V zinc-blende semiconductors. For the zinc-blende systems and their alloys, it is possible to grow heterostructures and SLs, in which the alloy content, thickness and interface chemistry can serve to tune the band gap and bandwidths [14] of the two sides of the interface to have type II or type III SL. In a first approximation, in the InAs/In(As,Sb) SLs due to the type II band alignment the electrons are confined within the InAs layer and the holes in the In(As,Sb) layers, and thus electrons and holes are spatially separated. Therefore, by adjustment of the InAs and/or In(As,Sb) thickness as well as the Sb concentration, it is feasible to tune the band gap within a wide range of the IR region. Moreover, the thickness and the Sb concentration have to be tuned to keep the average lattice constant of SL as close as possible to the lattice constant of the substrate. Owing to these unique properties, T2SLs InAs/In(As,Sb) have been chosen as materials for applications in the far-IR radiation. In this paper, we will give more details about the location and dispersion of electrons and holes in T2SLs InAs/In(As,Sb). To achieve this goal, we perform density functional theory (DFT) calculation for a large 3D SL using spin–orbit coupling (SCO) and modified Becke–Johnson (MBJ). On top of this, we calculate the optical properties making this calculation quite computationally demanding. To our knowledge, there was no previous calculation combining large 3D SL, spin–orbit, MBJ and optical properties.

In section 2, we describe the computational details, section 3 is devoted to the electronic and optical properties of the InAs and InSb bulk while in section 4 the $InAs/InAs_{0.625}Sb_{0.375}$ SL properties are investigated. Finally, section 5 is dedicated to the conclusions.

2. Computational details

We have performed DFT calculations by using the VASP package [15–17]. The core and the valence electrons are treated within the projector augmented wave method [18] with a cutoff of 300 eV for the plane wave basis. Given the importance of SOC in narrow-gap zinc-blende compounds and given the size of the SOC in the elements in question, all calculations have been performed with the relativistic effects taken into account. The valence bands are predominantly composed of anion *p*-states. Since the SOC energy of *p*-states is 164 meV in InAs [19], i.e. comparable to the bandgap, the inclusion of SOC is essential for an exact representation of the band structure. If SOC is not included in the calculations, the system is metallic in disagreement with experimental results. For compounds with a zinc-blende structure, DFT within a standard local spin density approximation does not predict properly electronic properties, e.g. band gaps, spin–orbit splittings, and effective masses. The resulting band structure has often a wrong band ordering at the Γ point; these compounds turn out to be zero-gap topological semimetals (like HgTe) rather than narrow-gap semiconductors. Few approaches have made it possible to solve this problem, among these, there is the hybrid exchange-correlation functional [20, 21] and an all-electron screened exchange approach within the full potential linearized augmented plane-wave method [22]. These approaches reproduce the experimental band gaps of these compounds, however, they are computationally expensive to study heterostructures. Therefore, in order to study heterostructures and SLs, we have employed the MBJ exchange-correlation functional together with generalized gradient approximation (GGA) for the exchange-correlation potential [23], which is a semilocal potential that improves the description of the band gaps especially for narrow gap semiconductors [24–26] including zinc-blende semiconductors [21, 27–29]. We can tune the band gap by varying the parameter c^{MBJ}, as reported in supplementary materials figures S1 and S2. The value of c^{MBJ} is the only adjustable parameter that is fixed fitting the band gap of the bulk compounds or the SL. In the literature, the MBJ approach was successfully used for other zinc-blende systems [30]. Despite the MBJ functional having problems with doped systems due to its non-locality [31], we have found that our

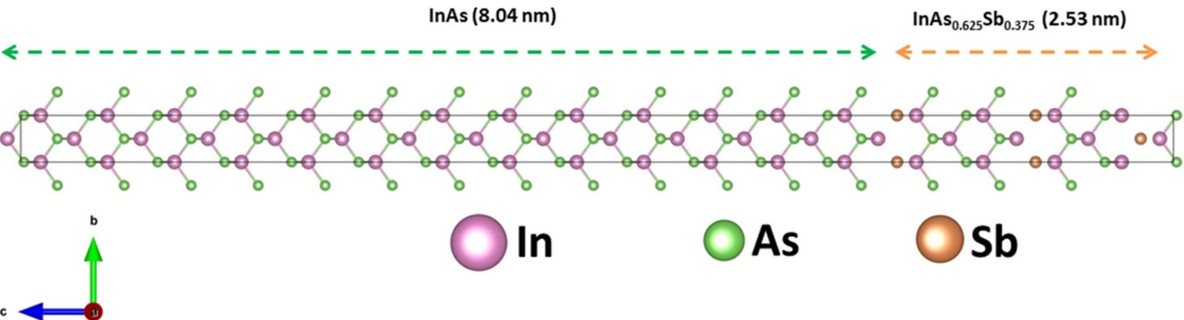

Figure 1. Optimized crystal structure of the InAs/$InAs_{0.625}Sb_{0.375}$ SL grown along the *z*-axis, (001) axis of the bulk unit cell. The orchid, green and sandy brown spheres represent In, As and Sb atoms, respectively. The dashed green arrow represents the extension of the InAs side of the supercell, while the dashed orange arrow represents the extension of the $InAs_{0.625}Sb_{0.375}$ side of the superlattice. The solid black line represents the unit cell of the superlattice.

results for the bulk system are quite remarkable. Therefore, we conclude that the MBJ provides reliable results if the properties of the doping do not differ too much from the properties of the host as in the case InAs doped with Sb. The GGA+U does not solve the gap problem for the zinc-blende unless we would use exotic negative Coulomb repulsions [32].

To inspect how the energy gaps and optical properties of InAs/$InAs_{0.625}Sb_{0.375}$ SL change as a function of the lattice constant, we used room temperature lattice constants of InAs, GaSb and AlSb, respectively. The values of the lattice parameters at $T = 300$ K are: $a_{\mathrm{InAs}} = 6.0583$ Å, $a_{\mathrm{GaSb}} = 6.0959$ Å and $a_{\mathrm{AlSb}} = 6.1355$ Å [33]. In other words, we considered the SL is grown on InAs, GaSb and AlSb substrates, respectively. The SLs are treated as fully strained and we have a perfect interface without intermixing. Our (001) SL is composed of 8.04 nm of InAs (26 unit cells) and 2.53 nm of $InAs_{5/8}Sb_{3/8}$ (8 unit cells), as shown in figure 1.

Table 1. Effective masses of bulk InAs calculate within MBJ (this work) compared with other theoretical approaches [20] and experimental results [34, 35] at Γ along different directions of the ***k***-space. Increasing the energy, we name the bands as split-off, light-hole, heavy-hole and electron bands as used in the literature [20].

Approach	Direction	$m_{\mathrm{split-off}}$	$m_{\mathrm{light-hole}}$	$m_{\mathrm{heavy-hole}}$	m_{electron}
HSE06	[100]	0.112	0.033	0.343	0.027
	[111]	0.111	0.031	0.836	0.027
	[110]	0.112	0.032	0.623	0.027
MBJ	[100]	0.189	0.064	0.155	0.021
	[111]	0.119	0.046	0.609	0.014
	[110]	0.062	0.037	0.409	0.031
Experiment	[100]	0.140	0.027	0.333	0.023
	[111]	0.140	0.037	0.625	0.026
	[110]	0.140	0.026	0.410	0.026

3. Bulk properties

In this section, we investigate the electronic and optical properties of the InAs and InSb bulk to use as a benchmark for the investigation on the SL.

3.1. Electronic properties of the InAs and InSb bulk

Using the eigenvalues at the Γ point of InAs and InSb bulk, we can calculate the band bending of the SLs. The band bending of the InAs/InSb returns a type III SL, while the band bending of the InAs/$InAs_{0.625}Sb_{0.375}$ returns a type II SL in agreement with experimental data. For the calculation of band gap of $InAs_{0.625}Sb_{0.375}$, we have used the virtual crystal approximation for the energetic levels with $0.625E_{\mathrm{c,v;InAs}}+0.375E_{\mathrm{c,v;InSb}}$ where $E_{\mathrm{c,v;InAs}}$ and $E_{\mathrm{c,v;InSb}}$ are the energetic levels of the valence (v) or conduction (c) bands of InAs and InSb, respectively. This highlights how our computational setup is reliable in the description of the electronic properties of this material class.

Using the notation of [20], table 1 summarizes the effective masses of the energy bands such as $m_{\mathrm{split-off}}$, $m_{\mathrm{light-hole}}$, $m_{\mathrm{heavy-hole}}$ and conduction electron m_{electron} along the directions [100], [110] and [111] for various theoretical and experimental approaches. In this paper, we have fitted the DFT band structure with a quadratic dispersion and reported the numerical values of the fitting. The effective masses calculated for heavy-hole along the [111] and [110] directions strongly match experimental results. Similarly, the effective masses of conduction electrons in the [100] and [111] directions coincide with those of experiments. Respect to the Heyd–Scuseria–Ernzerhof (HSE06) exchange-correlation results present in the literature, the light-holes in MBJ are heavier than HSE06 while the heavy-holes in MBJ are lighter than HSE06.

3.2. Optical properties of the InAs and InSb bulk

The optical properties of a particular semiconductor are of great interest due to their possible applications in optoelectronics and photon sensing. After establishing the values of c^{MBJ} for the bulk compounds, as reported in the supplementary materials figures S1 and S2, we calculate the optical properties of InAs and InSb at $T = 0$. In figures 2 and 3 we show optical characteristics of InAs and InSb in the bulk form, respectively. Due to the cubic symmetry, the optical properties of InAs and InSb bulk are isotropic and therefore independent on whether the electric field is polarized along the *x*-, *y*- and *z*-axis.

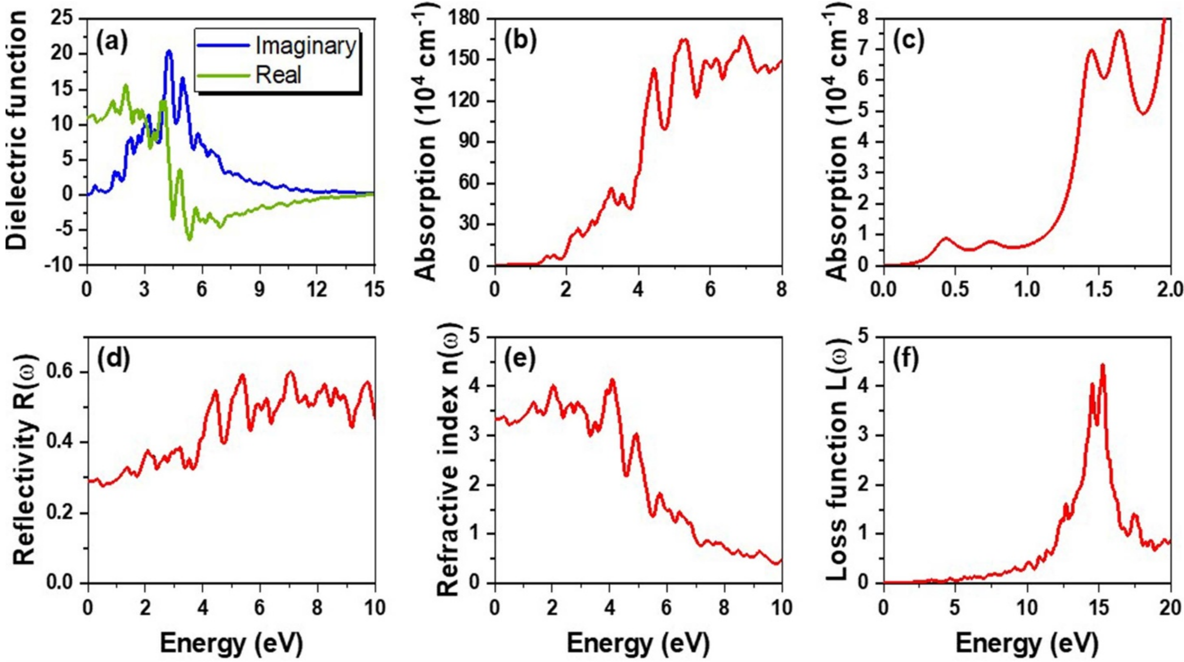

Figure 2. Frequency-dependent optical properties of InAs bulk with the low-temperature lattice constant. (a) Real (green line) and imaginary (blue line) parts of the dielectric function. (b) Absorption spectrum in the frequency-range between 0 and 8 eV. (c) Absorption spectrum in the IR region. (d) Reflectivity. (e) Refractive index. (f) Energy loss function.

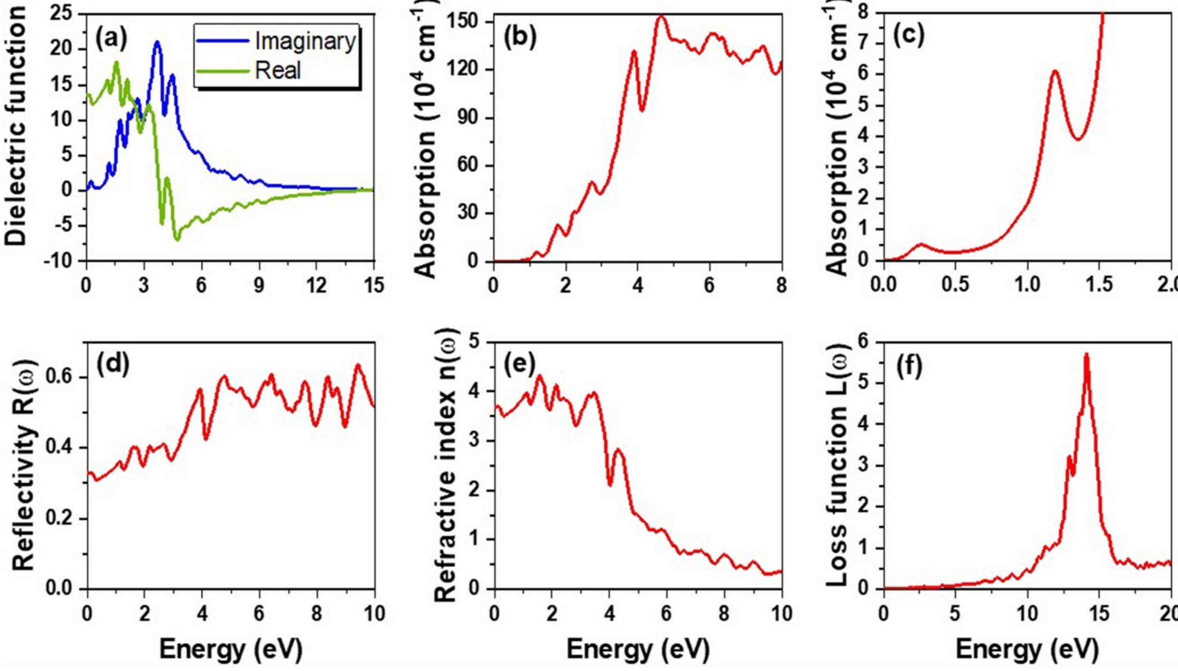

Figure 3. Frequency-dependent optical properties of InSb bulk with the low-temperature lattice constant. (a) Real (green line) and imaginary (blue line) parts of the dielectric function. (b) Absorption spectrum in the frequency-range between 0 and 8 eV. (c) Absorption spectrum in the IR region. (d) Reflectivity. (e) Refractive index. (f) Energy loss function.

Figures 2(a) and 3(a) illustrate the real and imaginary parts of the dielectric function for InAs and InSb, which are used to extract other optical responses for the system. The values of the real part of the dielectric function on the vertical *y*-axis of the graph are known as static values of the real part; the value of static dielectric constant for InAs is 11.07, while that of InSb is 13.42, which is in agreement with the values reported in theoretical [36, 38] and experimental works [37]. Table 2 gives a comparison between the present work and the literature. The imaginary and real parts of the dielectric function [39], as well as the refractive index, are in very good agreement with the literature [39] for both InAs and InSb.

Table 2. Static dielectric constants (ε) and refractive indices (n_0) for the InAs bulk in the present work and in the literature.

Approach	ε	(n_0)
Present work	11.07	3.315
GGA-EV theory [36]	10.82	3.289
Experiment [37]	11.67	—

If we look at the absorption spectra of figures 2(b) and 3(b), we can see that the first absorption peaks appear at 0.417 eV for InAs and 0.235 eV for InSb. These peaks correspond to the energy-gap between the highest occupied and the lowest unoccupied energy bands, characterizing specific electronic transitions. In figures 2(c) and 3(c) we zoom in the 0–2 eV energy range, to quantify and describe the importance of InAs and InSb semiconductors in the IR region. Previous calculations on the same material class were reported using an all-electron method with c^{MBJ} calculated self-consistently [40, 41] and tight-binding method [42], despite the different methodology our results are in quantitative agreement with the theoretical literature. If we compare our absorption spectra with experimental literature, we find that our theoretical absorption coefficients overestimate the experimental values as expected neglecting the local field effect.

Besides, the surface behavior of these semiconductors is studied via reflectivity, which is defined as the ratio of the reflected and incident power. Figures 2(d) and 3(d) display the reflectivity spectra for InAs and InSb, which indicate that these compounds are less reflective in the IR region compared to other regions. Nevertheless, the refractive index shows a substantial value in the IR region, as we can see from figures 2(e) and 3(e). The low reflectivity and higher refractive index in the IR region make these materials very useful for IR detectors. The static refractive indices n_0 are 3.315 and 3.684 for InAs and InSb, respectively. Further, the energy loss function (ELF) is calculated in figures 2(f) and 3(f), to measure the loss of energy taking place in the systems. Almost no energy loss can be seen for the photons in the IR region. However, as the energy increases beyond 5 eV, energy loss starts to increase and becomes maximum around 15 eV. The peaks in ELF spectra correspond to the plasma resonance and hence the associated frequency is the plasma frequency.

4. Study of the InAs/$InAs_{0.625}Sb_{0.375}$ SL

In this section, we study the SL of InAs/$InAs_{0.625}Sb_{0.375}$ since it is employed in the devices of IR-detectors. Here, we use as in-plane lattice constant of the SL the values of the InAs, GaSb and AlSb at $T = 300$ K, respectively [33]. We used the value of $c^{\mathrm{MBJ}} = 1.22$ for all atoms of the SL. This value gives a reasonable agreement with experimental results of 0.1 eV [43]. Then, we calculated the band structures and optical properties of the SL for the three different lattice constants. Both InAs and InSb have the zinc-blende as a structural ground state, then we do not expect any structural disorder in the alloy part of the SL. The following two subsections present the electronic and optical attributes with these three lattice constants.

4.1. Electronic properties of the SL

After the structural relaxation of the InAs/$InAs_{0.625}Sb_{0.375}$ SL, the electronic properties were calculated. Figure 4 shows the band structures calculated along the **k**-path X-Γ-M-X for the InAs/$InAs_{0.625}Sb_{0.375}$ SL for the three lattice constants of bulk InAs, GaSb and AlSb, sequentially. We noticed a considerable decrease in the energy gaps compared to the parent compounds which allows their applicability in far-IR detection. The value of the band gap is calculated to be 116 meV in the case of a_{InAs}, while for a_{GaSb} this decreases to 87 meV and further decreases to 53 meV for a_{AlSb}, as shown in table 3. We noticed that, as the value of the lattice constant increases, the energy gap of the SL decreases.

At the Γ point below the Fermi level, we have the highest valence band (HVB) two times degenerate. At 0.1 eV below HVB, we find another hole band two times degenerate, and another hole band two times degenerate at 0.25 eV below the HVB. All these six bands become almost degenerate at the high-symmetry point X, therefore, all these bands originate from the heavy-holes and light-holes of the bulk. We define the two HVBs as heavy-holes and the third highest valence band as light-hole. The presence of multiple heavy-hole bands is a huge difference respect to the bulk. The number of heavy-holes bands strongly depends on the period of the SL [43, 44]. In the literature with tight-binding models, usually it was reported one heavy-hole band [42, 43] for a 10.57 nm period. However, within first-principle calculations, we obtained two heavy-hole bands. The far we go from the Fermi level, heavier the effective masses of these bands become as opposite to the bulk where we have the HVB as heavy-hole and the second HVB as light-hole. In the case of the SL, we define the HVB as heavy-hole1 and the second HVB as heavy-hole2. To study the effect of lattice constant on the effective masses of the charge carriers, we computed the effective masses at the Γ point of the SL such as $m_{\mathrm{heavy-hole2}}$, $m_{\mathrm{heavy-hole1}}$ and m_{electron} along the two in-plane directions i.e. [100] and [110] as shown in table 3. We report different effective masses for the [100] and [110] directions, going beyond the approximation of isotropic effective mass in the k_x–k_y plane found in the literature.

Due to the change of the symmetry, it is not possible to compare directly the effective masses along the same directions in bulk and SL. However, it is interesting to compare the effective masses of the SL respect to the effective masses of the bulk, since we expect that this trend can be observable in experiments. The biggest change in the SL is the reduction of the effective masses of the HVB (heavy-hole1) respect to the bulk, while the second HVB (heavy-hole2) is now heavier as opposite to the bulk. The effective masses that we have calculated are in line with previous effective masses calculated with other theories [42, 43, 45]. A considerable decrease of the effective masses along the [100] direction can be seen, as the lattice constant increases from 6.05 830 Å (InAs) to 6.1355 Å (AlSb). Except for the m_{electron}, the effective masses along the [110] direction are smaller than the effective masses along the [100] direction. We have noticed that the lattice constant not only influences the band gaps but also the effective masses associated with charge carriers. Indeed, except for the m_{electron},

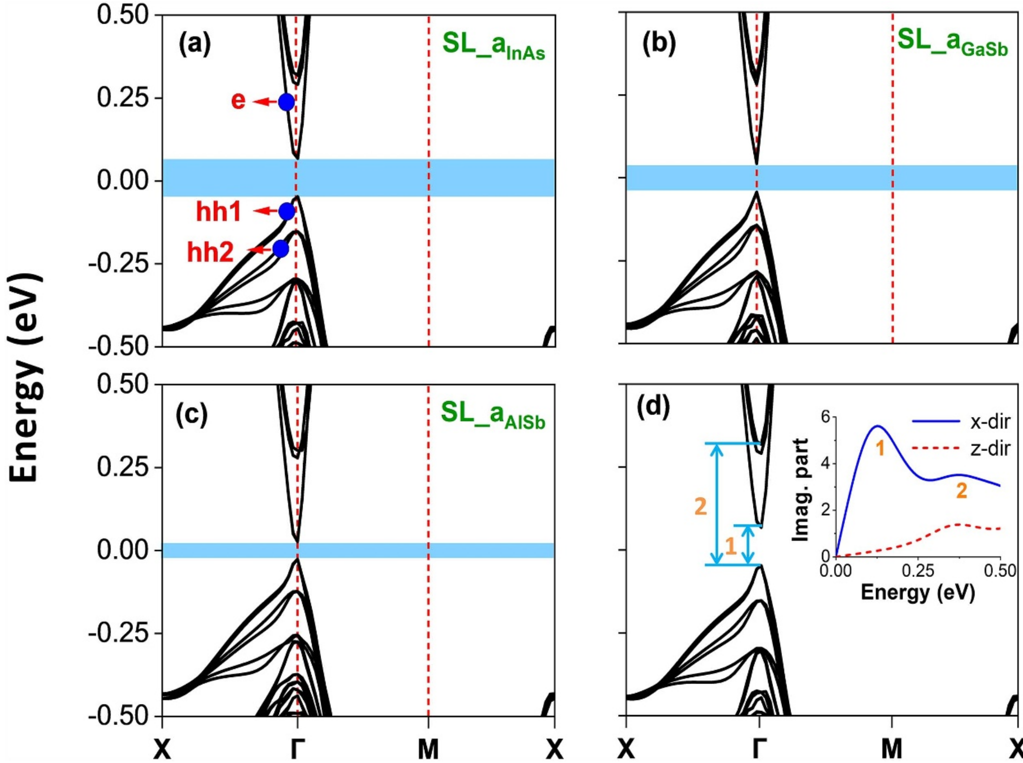

Figure 4. Band structures of the SL for three different lattice constants at 300 K i.e. (a) a_{InAs}, (b) a_{GaSb} and (c) a_{AlSb}. (d) Numbers 1 and 2 indicate the characteristic interband transitions. The inset shows the peaks associated with the number 1 and 2 in the imaginary part of the dielectric function for the x- and z-polarization of the electric field. The Fermi level is set to zero.

Table 3. Effective masses of $InAs/InAs_{0.625}Sb_{0.375}$ at Γ point along in-plane directions of the $\boldsymbol{k}$-space for the lattice constants of InAs, GaSb and AlSb and their comparison with the literature [43].

Lattice constant (Å)	Band gap	Direction	$m_{\mathrm{light-hole}}$	$m_{\mathrm{heavy-hole2}}$	$m_{\mathrm{heavy-hole1}}$	m_{electron}
InAs (6.0583)	0.116 eV	[100]		0.196	0.175	0.022
		[110]		0.062	0.056	0.023
GaSb (6.0959)	0.087 eV	[100]		0.147	0.126	0.016
		[110]		0.052	0.041	0.018
AlSb (6.1355)	0.053 eV	[100]		0.112	0.099	0.016
		[110]		0.046	0.044	0.024
k·p model for 14.5 nm SL [43]	0.1 eV	k_x–k_y plane	0.096	0.040		0.019
InAs/GaSb with 17 layers [44]	0.1 eV	k_x–k_y plane	0.051–0.061	0.33–0.37		0.023–0.031

Table 4. Effective masses of $InAs/InAs_{0.625}Sb_{0.375}$ at Γ point along k_z for the lattice constants of InAs, GaSb and AlSb and their comparison with the literature [43].

Lattice constant (Å)	Band gap	Direction	$m_{\mathrm{light-hole}}$	$m_{\mathrm{heavy-hole1}}$	$m_{\mathrm{heavy-hole2}}$	m_{electron}
GaSb (6.0959)	0.087 eV	[001]		54.9	32.5	0.256
k·p model for 14.5 nm SL [43]	0.1 eV	[001]	0.104	31.02		0.023

the effective masses decrease with the increase of the lattice constant of the SL.

The SL Brillouin zone is very different from the bulk Brillouin zone due to the change of the unit cell symmetries and lattice constants. In particular, the z-axis is extremely elongated flattening the band and increasing the effective mass along the [001] direction [43]. The calculated effective masses along [001] are reported in table 4 and compared with the literature. The calculated effective masses of the heavy-holes along [001] are extremely high as 54.9 which is comparable with the literature. The effective electron mass along [001] is 0.256 which is one order of magnitude larger than the in-plane effective masses. The reason for the difference between holes and electrons lies in the properties of the Γ_6 in zinc-blende semiconductors. The wave function of the Γ_6 state is in a quantum bonding state between the s-orbitals of Indium that

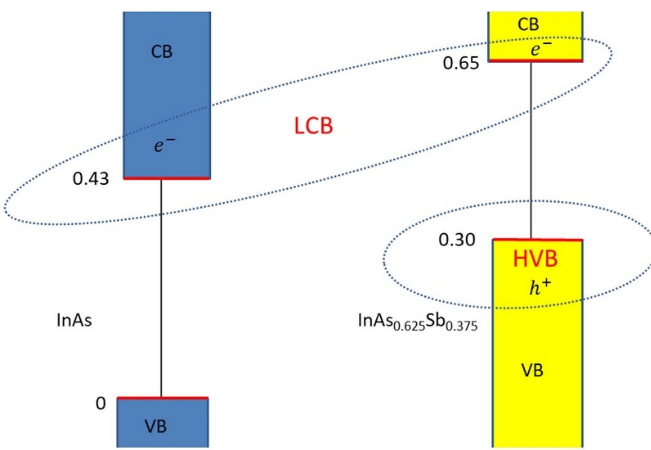

Figure 5. Type-II band bending using the gap of bulk InAs and $InAs_{0.625}Sb_{0.375}$ calculated for $c^{MBJ} = 1.180$. From the bulk data, we estimate the LCB and HVB of the supercell. The filled rectangulars represent the electronic bands connected by black lines representing the band gap. e^- and h^+ represent electrons and holes. The ovals represent the positions of LCB and HVB in the real space, while the HVB is mainly located in the In(As,Sb) side, the electrons are delocalized along the superlattice. The energy zero is fixed at the top of the valence band of InAs. The numerical values are in eV.

can be approximated as: $|\Gamma_6\rangle \approx \frac{1}{\sqrt{N}} \sum_{i=1,N} |5s\text{-In}_i\rangle$ where the index i runs on the N atoms of Indium present in the supercell, minor contributions from the s orbitals of the anions are also present. This bonding state is delocalized on both sides of the supercell. The band bending of the T2SL $InAs/InAs_{0.625}Sb_{0.375}$ is shown in figure 5 together with the atomic character of the electrons of the lowest conduction band (LCB) and HVB of the $InAs/InAs_{0.625}Sb_{0.375}$ supercell. The DFT results confirm that the orbital character of the LCB is mainly 5s-In while the orbital character of the HVB is mainly 5p-Sb. In summary, the electrons are delocalized along the SL owning a small mass, while the holes are localized in the In(As,Sb) side of the SL owning a huge effective mass. As a consequence the concentration and the distribution of the Sb doping mainly affects the hole carriers. The gap obtained from the band bending is 0.13 eV, which is in agreement with the literature [46] and in qualitative agreement with the more accurate results for the supercell presented in table 3.

In figure 4(d), the interband electronic transitions related to the excitations in the SL are described. The light–matter interactions can be explained by the complex dielectric function, i.e. the imaginary part is directly linked to the absorption. The observed peaks in the inset of figure 4(d) can be connected to the excitation of electrons from the valence band maximum to the conduction bands for a_{InAs} based SL, which are also indicated by the interband transitions in figure 4(d) with the transition number 1 at 115 meV and with the transition number 2 at 365 meV. These excitations can take place owing to the vertical transition from the valence band to the conduction bands at the Γ point of the Brillouin zone as indicated in figure 4(d). Since the gap depends on the lattice constant, we figured out that also the energies required to cause the interband transitions are affected by the different lattice constants.

4.2. Optical properties of the SL

Based on the relaxed structure, we have explored the optical properties of $InAs/InAs_{0.625}Sb_{0.375}$ SLs with the MBJ exchange-correlation functional. Again, the three different lattice constants are considered to calculate the optical properties as illustrated in figures 6, S3 and S4, respectively. For the SL, we observed that all the optical properties are anisotropic because of the reduction in symmetry [47]. Besides, the results in figures 6(a), S3 and S4 are almost identical, which shows that the small changes in in-plane lattice constant has a very small effect on the optical properties. Figures 6(a), S3(a) and S4(a) demonstrate the real and imaginary parts of the dielectric function for the three cases, respectively. Owing to the anisotropy, the values of static dielectric constants for SLs with the InAs, GaSb and AlSb lattice constant are (19.40, 15.57), (24.06, 12.20) and (30.00, 13.14) in the x and z-directions, respectively. Table 5 demonstrates the static dielectric constants $(\varepsilon_x, \varepsilon_z)$ and refractive indices (n_x, n_z) of $InAs/InAs_{0.625}Sb_{0.375}$ for lattice constants of InAs, GaSb and AlSb, respectively. The absorption coefficients of the SL for the three lattice constants are shown in figures 6(b), (c), S3(b), (c) and S4(b), (c). The first absorption peak appears near 0.115 eV and the second appears at 0.365 eV in the case of InAs lattice constant, for the GaSb case they appear at 0.092 eV and 0.316 eV while for the AlSb case the first and second peaks appear at 0.082 eV and 0.273 eV, respectively.

In figures 6(b), S3(b) and S4(b), we report the absorption spectra in the region between 0 and 8 eV. The absorption spectra strongly increase from the frequency of the energy gap until approximately 5 eV. Beyond 5 eV, the absorption spectrum reaches a plateau with moderate oscillations of the order of 15%. Including the electron–hole interaction, the plateau would be reached at lower frequencies. Similarly in figures 6(c), S3(c) and S4(c), we report the absorption spectra in the region between 0 and 2 eV that is the relevant region for IR detectors. We report the absorption coefficient when the electric field is polarized along the x-axis (α_{E_x}) and z-axis (α_{E_z}). We can immediately see how the absorption coefficient is much larger when the electric field is polarized along the x-axis, i.e. orthogonal to the growth axis. Defining θ as the angle between the polarization of the electric field and the z-axis, we have that the absorption coefficient $\alpha(\theta)$ is equal to:

$$\alpha(\theta) = \sin(\theta)\alpha_{E_x} + \cos(\theta)\alpha_{E_z}. \tag{1}$$

We have found characteristic absorption peaks in the low-energy regions that quantify the characteristic interband transitions. This employs the possibility of using these SLs for IR detection. Similar to the bulk case, the SL is also less reflective in the IR region (see figures 6(d), S3(d) and S4(d)). Also, the refractive indices are higher in the IR range as shown in figures 6(e), S3(e) and S4(e). Such less reflection of the photons and higher corresponding indices of refraction in the IR range of the electromagnetic spectrum suggests their applications in the IR detectors. It can be noticed that the static refractive indices n_0 are also anisotropic; these are (4.4, 3.4), (4.9, 3.5) and (5.5, 3.6) for InAs, GaSb and AlSb based lattice constants in the (x, z) directions (table 5). Moreover, the ELFs

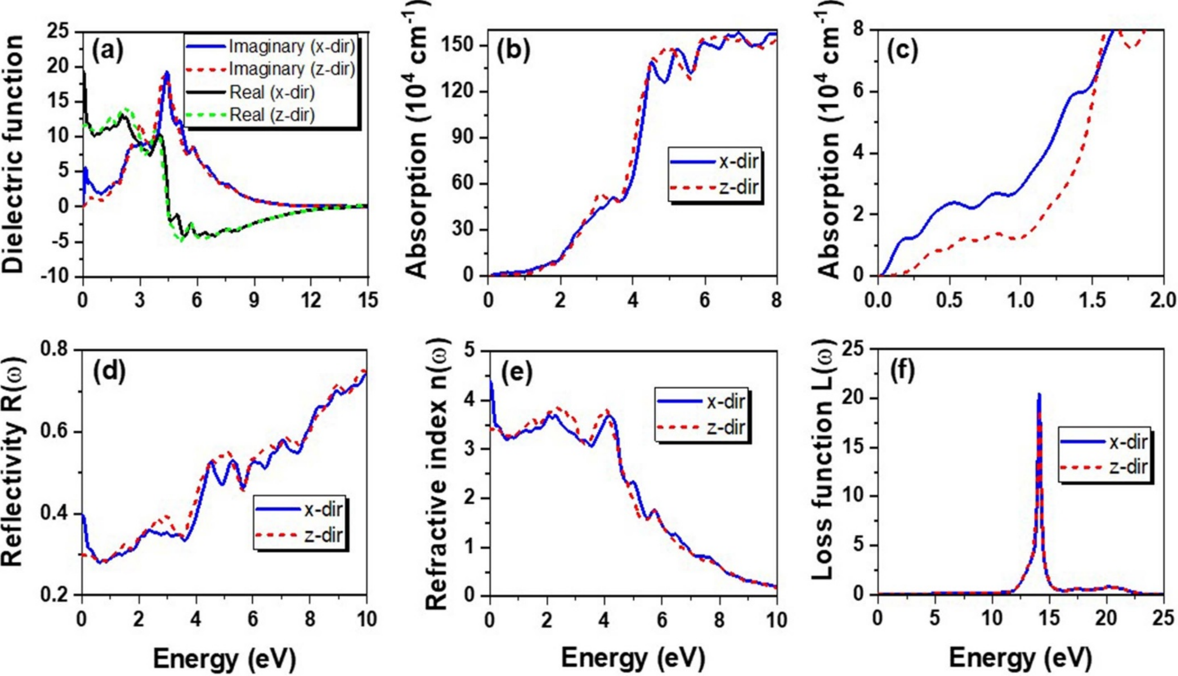

Figure 6. Frequency-dependent optical properties of $InAs/InAs_{0.625}Sb_{0.375}$ superlattice with lattice constant at T = 300 K that is $a_{InAs} = 6.0583$ Å. (a) Real and imaginary parts of the dielectric function. (b) Absorption spectra in the frequency-range between 0 and 8 eV. (c) Absorption spectra in the IR region. (d) Reflectivity. (e) Refractive index. (f) Energy loss function. The x-dir and z-dir indicate the directions of the electric field polarized perpendicular and parallel to z-axis of the SL.

Table 5. Static dielectric constants $(\varepsilon_x, \varepsilon_z)$ and refractive indices (n_x, n_z) of $InAs/InAs_{0.625}Sb_{0.375}$ for lattice constants of InAs, GaSb and AlSb, respectively, using the MBJ approach.

Lattice constant (Å)	ε_x	ε_z	n_x	n_z
InAs (6.0583)	19.4	15.6	4.40	3.40
GaSb (6.0959)	24.1	12.2	4.90	3.51
AlSb (6.1355)	30.0	13.1	5.51	3.60

for the three cases reveal almost identical behavior and show no energy loss up to 12 eV, particularly for the photons in the IR range as shown in figures 6(f), S3(f) and S4(f).

Since the most relevant physical property for the far-IR detectors is the absorption spectrum, finally, we compare the absorption spectra in the IR region for InAs bulk and the SLs in figure 7. It can be seen that the absorption strongly increases for SL in the IR regime as compared to InAs bulk. Also, the absorption is observed to increase as a function of the lattice constant and becomes maximum for the lattice constant of a_{AlSb}. The reason for the large absorption coefficient of the SL could be attributed to the presence of the two heavy-hole bands. Then, we can speculate that thicker SLs could produce even larger absorption spectra provided that the quality of the sample and the strain would be uniform along the SL. However, the uniform strain is limited by the critical thickness in the experimental realization.

To go beyond the independent-particle approximation employed here for the optical properties, we would need the using Bethe–Salpeter equation that includes the electron–hole interaction. The Bethe–Salpeter equation would produce a

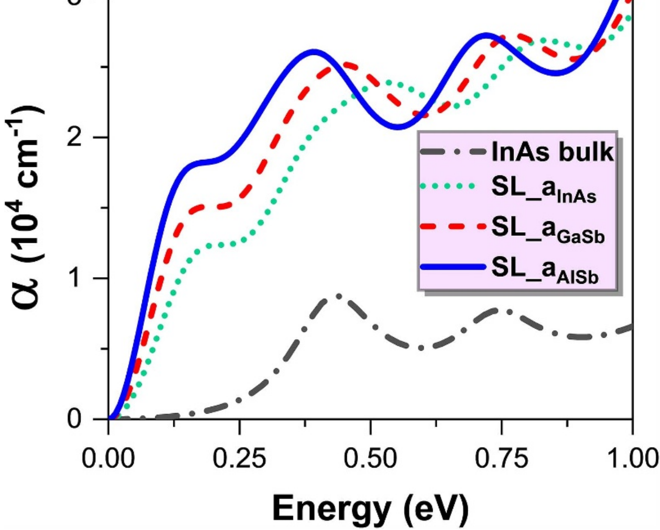

Figure 7. Absorption coefficient for an electric field polarized along the x-direction in the far-infrared regime between 0 and 1 eV. Spectra of InAs bulk (dash-dotted grey line) and $InAs/InAs_{0.625}Sb_{0.375}$ SLs for InAs (dotted green line), GaSb (dashed red line) and AlSb (solid blue line) substrate.

shift of the peak in the imaginary part to lower frequencies [48, 49]. The Bethe–Salpeter couples the electron and the hole, and thus takes into account the electron–hole interactions [50]. This approach has been very successful for the calculation of absorption spectra of a large variety of systems bearing large band gaps, such as wide band gap semiconductors

and insulators [51]. On the other hand, the small-gap semiconductors and metals, instead, screen this electron–hole interaction, and the resulting contribution can therefore be negligible. Since we are dealing with ultranarrow gap semiconductors, the MBJ potential is sufficient for our study.

5. Conclusions and outlook

We have investigated the electronic and optical properties of InAs and InSb bulk and their SLs. We perform a computationally demanding calculation for the realistic system combining a large SL, SCO, MBJ and optical properties. We focus on the $InAs/InAs_{0.625}Sb_{0.375}$ SL with the three lattice constants of the bulk InAs, GaSb and AlSb, respectively. It is observed that the electronic and optical properties effectively change due to the different symmetry present in the SL and with the lattice constant of the SL. In the SL, we notice a considerable decrease in both the energy gaps and the effective masses of the heavy-holes compared to the bulk phases of the parent compounds. As opposite to the tight-biding literature, we have found two heavy-hole bands with the in-plane effective mass increasing as far as we go further from the Fermi level. In the k_x–k_y plane, the effective masses of the heavy-holes in the SL become comparable with the one of the light-holes of the bulk. Along the growth axis, the effective mass of the hole becomes huge while the effective mass of electron increases less significantly. This happens since the electrons are delocalized in the entire SL while the holes are localized in the In(As,Sb) side of the SL. As future prospects, it would be helpful to simulate the randomness of the Sb distribution and the possible Sb interdiffusion in the InAs layer. This would require larger supercells and could not be done following this computational approach.

Our theoretical calculations demonstrate that the absorption spectra in the far-IR regime strongly increased in the case of SL with respect to bulk InAs and InSb. The absorption coefficient of the SL is larger if the electric field is polarized in the direction orthogonal to the growth axis. Moreover, the absorption spectrum as a function of the lattice constant is increased at low frequency. The appearance of multiple heavy-hole and a small energy gaps of the order of meVs produces a high absorption coefficient making these SLs employable for applications in far IR detectors. The large sensitivity of the optical properties to structural and chemical degrees of freedom opens the possibility of engineering the optical property of the InAs-based SL making them even more appealing for the construction of far IR detectors.

Data availability statement

The data that support the findings of this study are available upon reasonable request from the authors.

Acknowledgments

G H and G C contributed equally to this work. We thank T Story and M Birowska for useful discussions. The work is supported by the Foundation for Polish Science through the International Research Agendas program co-financed by the European Union within the Smart Growth Operational Programme. This work was financially supported by the National Science Center in the framework of the 'PRELUDIUM' (Decision No.: DEC-2020/37/N/ST3/02338). We acknowledge the access to the computing facilities of the Interdisciplinary Center of Modeling at the University of Warsaw, Grants G84-0, GB84-1 and GB84-7. We acknowledge the CINECA award under the ISCRA initiative IsC85 'TOPMOST' and IsC93 'RATIO' grant, for the availability of high-performance computing resources and support.

ORCID iDs

Ghulam Hussain https://orcid.org/0000-0003-1654-9156
Giuseppe Cuono https://orcid.org/0000-0002-1550-5429
Rajibul Islam https://orcid.org/0000-0001-9076-7843
Carmine Autieri https://orcid.org/0000-0002-5008-8165
Tomasz Dietl https://orcid.org/0000-0003-1090-4380

References

[1] Rogalski A, Martyniuk P and Kopytko M 2017 InAs/GaSb type-II superlattice infrared detectors: future prospect *Appl. Phys. Rev.* **4** 031304
[2] Rogalski A, Martyniuk P, Kopytko M, Madejczyk P and Krishna S 2020 InAsSb-based infrared photodetectors: thirty years later on *Sensors* **20** 24
[3] Ting D Z, Rafol S B, Khoshakhlagh A, Soibel A, Keo S A, Fisher A M, Pepper B J, Hill C J and Gunapala S D 2020 InAs/InAsSb type-II strained-layer superlattice infrared photodetectors *Micromachines* **11** 11
[4] Ting D Z, Khoshakhlagh A, Soibel A and Gunapala S D 2020 Long wavelength InAs/InAsSb infrared superlattice challenges: a theoretical investigation *J. Electron. Mater.* **49** 6936–45
[5] Martyniuk P, Michalczewski K, Tsai T Y, Wu C and Wu Y R 2020 Theoretical modeling of XBn T2SLs InAs/InAsSb/B-AlSb longwave infrared detector operating under thermoelectrical cooling *Opt. Quantum Electron.* **52** 6936–45
[6] Ting D Z, Soibel A, Khoshakhlagh A, Keo S A, Rafol S B, Fisher A M, Pepper B J, Luong E M, Hill C J and Gunapala S D 2019 Advances in III–V semiconductor infrared absorbers and detectors *Infrared Phys. Technol.* **97** 210–6
[7] Wu D, Durlin Q, Dehzangi A, Zhang Y and Razeghi M 2019 High quantum efficiency mid-wavelength infrared type-II $InAs/InAs_{1-x}Sb_x$ superlattice photodiodes grown by metal-organic chemical vapor deposition *Appl. Phys. Lett.* **114** 1
[8] Steenbergen E H *et al* 2011 Significantly improved minority carrier lifetime observed in a long-wavelength infrared III–V type-II superlattice comprised of InAs/InAsSb *Appl. Phys. Lett.* **99** 251110
[9] Klipstein P C, Livneh Y, Glozman A, Grossman S, Klin O, Snapi N and Weiss E 2014 Modeling InAs/GaSb and InAs/InAsSb superlattice infrared detectors *J. Electron. Mater.* **43** 8
[10] Moehle C M *et al* 2021 InSbAs two-dimensional electron gases as a platform for topological superconductivity *Nano Lett.* **21** 9990–6

[11] Pikulin D I and Hyart T 2014 Interplay of exciton condensation and the quantum spin Hall effect in InAs/GaSb bilayers *Phys. Rev. Lett.* **112** 176403

[12] Winkler G W, Wu Q, Troyer M, Krogstrup P and Soluyanov A A 2016 Topological phases in $InAs_{1-x}Sb_x$: from novel topological semimetal to Majorana wire *Phys. Rev. Lett.* **117** 076403

[13] Nguyen N M, Cuono G, Islam R, Autieri C, Hyart T and Brzezicki W 2022 Unprotected edge modes in quantum spin Hall insulator candidate materials (arXiv:2209.06912)

[14] Mikhailova M P, Moiseev K D and Yakovlev Y P 2004 Interface-induced optical and transport phenomena in type II broken-gap single heterojunctions *Semicond. Sci. Technol.* **19** R109–28

[15] Kresse G and Hafner J 1993 *Ab initio* molecular dynamics for liquid metals *Phys. Rev.* B **47** 558–61

[16] Kresse G and Furthmüller J 1996 Efficiency of *ab-initio* total energy calculations for metals and semiconductors using a plane-wave basis set *Comput. Mater. Sci.* **6** 15–50

[17] Kresse G and Furthmüller J 1996 Efficient iterative schemes for *ab initio* total-energy calculations using a plane-wave basis set *Phys. Rev.* B **54** 11169–86

[18] Kresse G and Joubert D 1999 From ultrasoft pseudopotentials to the projector augmented-wave method *Phys. Rev.* B **59** 1758–75

[19] Cuono G, Autieri C, Guarnaccia G, Avella A, Cuoco M, Forte F and Noce C 2019 Spin–orbit coupling effects on the electronic properties of the pressure-induced superconductor CrAs *Eur. Phys. J. Spec. Top.* **228** 631–41

[20] Kim Y-S, Hummer K and Kresse G 2009 Accurate band structures and effective masses for InP, InAs and InSb using hybrid functionals *Phys. Rev.* B **80** 035203

[21] Cuono G, Autieri C and Dietl T 2022 In manuscript

[22] Geller C B, Wolf W, Picozzi S, Continenza A, Asahi R, Mannstadt W, Freeman A J and Wimmer E 2001 Computational band-structure engineering of III–V semiconductor alloys *Appl. Phys. Lett.* **79** 368–70

[23] Tran F and Blaha P 2009 Accurate band gaps of semiconductors and insulators with a semilocal exchange-correlation potential *Phys. Rev. Lett.* **102** 226401

[24] Camargo-Martínez J A and Baquero R 2012 Performance of the modified Becke-Johnson potential for semiconductors *Phys. Rev.* B **86** 195106

[25] Islam R, Cuono G, Nguyen N M, Noce C and Autieri C 2019 Topological transition in $Pb_{1-x}Sn_xSe$ using meta-GGA exchange-correlation functional *Acta Phys. Pol.* A **136** 4

[26] Goyal A, Gorai P, Toberer E and Stevanovic V 2017 *npj Comput. Mater.* **3** 42

[27] Autieri C, Śliwa C, Islam R, Cuono G and Dietl T 2021 Momentum-resolved spin splitting in Mn-doped trivial CdTe and topological HgTe semiconductors *Phys. Rev.* B **103** 115209

[28] Śliwa C, Autieri C, Majewski J A and Dietl T 2021 Superexchange dominates in magnetic topological insulators *Phys. Rev.* B **104** L220404

[29] Islam R, Ghosh B, Cuono G, Lau A, Brzezicki W, Bansil A, Agarwal A, Singh B, Dietl T and Autieri C 2022 Topological states in superlattices of HgTe class of materials for engineering three-dimensional flat bands *Phys. Rev. Res.* **4** 023114

[30] Silva J, Blas A and Hoat D 2019 Theoretical study of electronic and optical properties of antiferromagnetic $\beta-$MnS using the modified Becke-Johnson (mBJ) potential *J. Phys. Chem. Solids* **128** 310–5

[31] Rauch T, Marques M A L and Botti S 2020 Local modified Becke-Johnson exchange-correlation potential for interfaces, surfaces and two-dimensional materials *J. Chem. Theory Comput.* **16** 2654–60

[32] Yu M, Yang S, Wu C and Marom N 2020 Machine learning the Hubbard U parameter in DFT+U using Bayesian optimization *npj Comput. Mater.* **6** 180

[33] Vurgaftman I, Meyer J R and Ram-Mohan L R 2001 Band parameters for III–V compound semiconductors and their alloys *J. Appl. Phys.* **89** 5815–75

[34] Shur M S 1996 *Handbook Series on Semiconductor Parameters* vol 1 (Singapore: World Scientific)

[35] Chen A-B and Sher A 1995 *Semiconductor Alloys: Physics and Materials Engineering* (New York: Springer Science & Business Media)

[36] Sohrabi L, Boochani A, Sebt S A and Elahi S M 2017 Structural, electronic and optical properties of InAs phases: by GGA-PBG and GGA-EV approximations *J. Chem. Res.* **41** 172–82

[37] Philipp H and Ehrenreich H 1963 Optical properties of semiconductors *Phys. Rev.* **129** 1550

[38] Ziane M I, Bensaad Z, Labdelli B and Bennacer H 2014 First-principles study of structural, electronic and optical properties of III-arsenide binary GaAs and InAs and III-nitrides binary GaN and InN: improved density-functional-theory study *Sens. Transducers* **27** 374

[39] Aspnes D E and Studna A A 1983 Dielectric functions and optical parameters of Si, Ge, GaP, GaAs, GaSb, InP, InAs and InSb from 1.5 to 6.0 eV *Phys. Rev.* B **27** 985–1009

[40] Namjoo S and Puschnig P 2022 Optical properties of InAs, InSb and $InAs_xSb_{1-x}$ (x=0.25, 0.5, 0.75) alloys under strain *Comput. Condens. Matter* **30** e00610

[41] Namjoo S, Rozatian A S H, Jabbari I and Puschnig P 2015 Optical study of narrow band gap $InAs_xSb_{1-x}$ ($x = 0$, 0.25, 0.5, 0.75, 1) alloys *Phys. Rev.* B **91** 205205

[42] Smith D L and Mailhiot C 1987 Proposal for strained type II superlattice infrared detectors *J. Appl. Phys.* **62** 2545–8

[43] Manyk T, Michalczewski K, Murawski K, Martyniuk P and Rutkowski J 2019 InAs/InAsSb strain-balanced superlattices for longwave infrared detectors *Sensors* **19** 1907

[44] Smith D L and Mailhiot C 1990 Theory of semiconductor superlattice electronic structure *Rev. Mod. Phys.* **62** 173–234

[45] Tsai T-Y, Michalczewski K, Martyniuk P, Wu C-H and Wu Y-R 2020 Application of localization landscape theory and the $\boldsymbol{k}\cdot\boldsymbol{p}$ model for direct modeling of carrier transport in a type II superlattice InAs/InAsSb photoconductor system *J. Appl. Phys.* **127** 033104

[46] Kroemer H 2004 The 6.1 Å family InAs, GaSb, AlSb) and its heterostructures: a selective review *Physica* E **20** 196–203

[47] Jiang M, Xiao H, Peng S, Qiao L, Yang G, Liu Z and Zu X 2020 Effects of stacking periodicity on the electronic and optical properties of GaAs/AlAs superlattice: a first-principles study *Sci. Rep.* **10** 1–7

[48] Sajjad M, Singh N and Schwingenschlögl U 2018 Strongly bound excitons in monolayer PtS_2 and $PtSe_2$ *Appl. Phys. Lett.* **112** 043101

[49] Varrassi L, Liu P, Yavas Z E, Bokdam M, Kresse G and Franchini C 2021 Optical and excitonic properties of transition metal oxide perovskites by the Bethe-Salpeter equation *Phys. Rev. Mater.* **5** 074601

[50] Reining L 2016 Linear response and more: the Bethe-Salpeter equation *Quantum Materials: Experiments and Theory (Modeling and Simulation* vol 6*)* ed E Pavarini, E Koch, J van den Brink and G Sawatzky (Forschungszentrum Julich) ch 10 (available at: www.cond-mat.de/events/correl16)

[51] Sottile F 2003 Response functions of semiconductors and insulators: from the Bethe-Salpeter equation to time-dependent density functional theory *PhD Thesis* Ecole Polytechnique X

Supplementary Materials: Electronic and optical properties of InAs/InAs$_{0.625}$Sb$_{0.375}$ superlattices and their application for far-infrared detectors

Ghulam Hussain,[1,*] Giuseppe Cuono,[1,†] Rajibul Islam,[1] Artur Trajnerowicz,[2] Jarosław Jureńczyk,[2] Carmine Autieri,[1,3,‡] and Tomasz Dietl[1,4]

[1] *International Research Centre MagTop, Institute of Physics, Polish Academy of Sciences, Aleja Lotników 32/46, PL-02668 Warsaw, Poland*
[2] *VIGO System S.A. 129/133 Poznanska Str., 05-850 Ozarow Mazowiecki, Poland*
[3] *Consiglio Nazionale delle Ricerche CNR-SPIN, UOS Salerno, I-84084 Fisciano (Salerno), Italy*
[4] *WPI-Advanced Institute for Materials Research, Tohoku University, Sendai 980-8577, Japan*

(Dated: January 8, 2023)

I. COMPUTATIONAL DETAILS

We have performed the bulk calculations using 10×10×10 k-points centred in Γ. The values of the lattice parameters at $T = 0\,\mathrm{K}$ are: $a_{\mathrm{InAs}} = 6.05008\,\text{Å}$ and $a_{\mathrm{InSb}} = 6.46896\,\text{Å}$[1]. Due to the large value of the out-of-plane SL period, the k_z range in the SL first Brillouin zone is rather small. We have carried out the InAs/InAs$_{0.625}$Sb$_{0.375}$ SL calculations using 10×10×1 k-points centred at Γ . Before calculating the electronic and optical properties of the SL, we have performed the structural relaxation of the internal degrees of freedom within GGA without SOC. The reliability of the structural relaxation without SOC was proved in the literature[2] and tested by us for simple cases.

We use the lattice constants and the optimal doping concentration from the experimental system. We construct a supercell with a single atom species in the subsequent layers, so that the InAs$_{5/8}$Sb$_{3/8}$ consists of eight unit cells, with three Sb and five As layers, respectively. We performed three different calculations for the SL using InAs, GaSb and AlSb in-plane lattice constants at room temperature. This allows us to investigate the properties of SL close to the substrate and the fully relaxed one far from the substrate.

The optical properties are obtained by using the frequency-dependent dielectric function $\epsilon(\omega)$ written as:

$$\epsilon(\omega) = \epsilon_1(\omega) + i\epsilon_2(\omega)$$

where ω is the photon angular frequency, while $\epsilon_1(\omega)$ and $\epsilon_2(\omega)$ represent the real and imaginary parts of the complex dielectric function, respectively. The imaginary part can be calculated in random phase approximation neglecting local field effects via the output of the DFT calculations using the following formula:

$$\epsilon_2(\omega) = \frac{\nu e^2}{2\pi h m^2 \omega^2} \int d^3k \sum_{mn'} f_{n,\mathbf{k}}(1 - f_{n',\mathbf{k}})$$
$$| < n, \mathbf{k}|\mathbf{p}|n', \mathbf{k} > |^2 \times \delta(E_{n,\mathbf{k}} - E_{n',\mathbf{k}} - \hbar\omega) \quad (1)$$

where f is the Fermi-Dirac distribution, $\mathbf{p}$ is the momentum operator, $E_{n,\mathbf{k}}$ is the energy spectrum as a function of the number of bands n and wave vector $\mathbf{k}$. The real

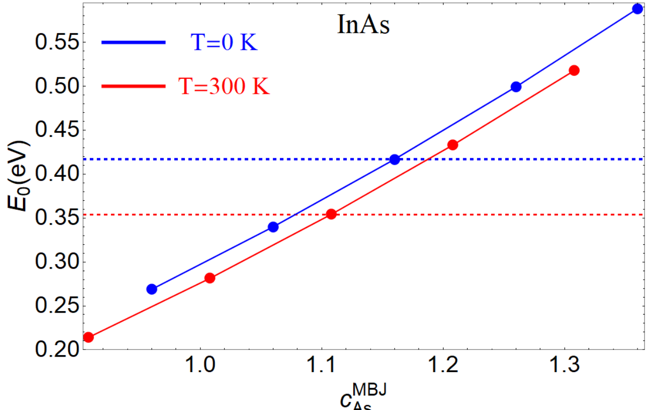

FIG. 1. Band gap at Γ point for InAs as a function of c_{As}^{MBJ}, and with $c_{In}^{MBJ} = 1.180$. The blue line indicates the band gap at $T = 0\,\mathrm{K}$, while the red line the band gap at $T = 300\,\mathrm{K}$. The experimental band gap is represented by the horizontal blue dashed line in the case of $T = 0\,\mathrm{K}$, while by the horizontal red dashed line in the case of $T = 300\,\mathrm{K}$.

part of the optical conductivity can be calculate using the Kramers-Kronig transformation:

$$\epsilon_1(\omega) = 1 + \frac{2}{\pi} P \int_0^\infty \frac{\epsilon_2(\omega')\omega'}{\omega'^2 - \omega^2} d\omega' \quad (2)$$

This approach is known to overestimate the dielectric constant[3], however the large supercell and the inclusion of the SOC does not allow us to go beyond. The absorption coefficient $\alpha(\omega)$ can be derived from the $\epsilon_1(\omega)$ and $\epsilon_2(\omega)$ as follows:

$$\alpha = \frac{\sqrt{2}\omega}{c} \left(\sqrt{\epsilon_1^2 + \epsilon_2^2} - \epsilon_1 \right)^{1/2}$$

where c is the speed of light.

We employed the independent-particle approximation with a broadening of 50 meV for the imaginary part of the dielectric function. We have set the number of frequency points when calculating the dielectric function NEDOS=30000 for the bulk and NEDOS=40000 for the SL. This computational setup allows us to perform accurate optical calculations for the superlattice within a reasonable computational cost. We use a number

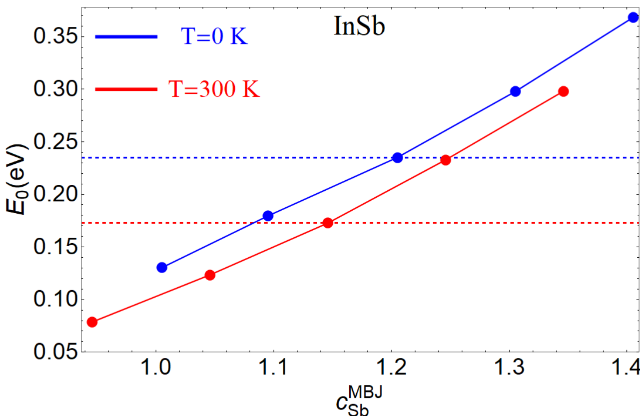

FIG. 2. Band gap at Γ point for InSb as a function of c_{Sb}^{MBJ}, and with c_{In}^{MBJ}=1.180. The blue line indicates the band gap at T=0 K, while the red line the band gap at T=300 K. The experimental band gap is represented by the horizontal blue dashed line in the case of T=0 K, while by the horizontal red dashed line in the case of T=300 K.

of 252 unoccupied bands for an energy window in the conduction bands of 6 eV in the case of the superlattice. The optical properties were already calculated successfully using MBJ for bulk semiconductors like MnS, GaN, Si, MnO, GaAs etc.[4], but we go beyond calculating superlattices in presence of spin-orbit.

II. BULK PROPERTIES

A. Electronic properties of the InAs and InSb bulk

For the bulk, we used the MBJ exchange-correlation functional wherein the parameter c^{MBJ} was adjusted to reproduce the experimental band gaps at the Γ point, which are 0.417 eV for InAs and 0.235 eV for InSb, respectively at temperature $T = 0$,[1] and decrease to 0.354 eV for InAs and 0.173 eV for InSb at 300 K.[5] From our calculations, we noticed that the gap is rather sensitive to the value of the lattice parameter. We should choose one value of c^{MBJ} for each of the three elements In, As and Sb. We can use the two band gaps of InAs and InSb to determine the c^{MBJ} values, therefore, we need to choose an arbitrary value for one of the elements. We decide to fix $c_{\mathrm{In}}^{\mathrm{MBJ}}$ of the common element to 1.180 that is a reasonable value for these compounds, so we can adjust the magnitudes of the single parameters $c_{\mathrm{As}}^{\mathrm{MBJ}}$ and $c_{\mathrm{Sb}}^{\mathrm{MBJ}}$ in order to reproduce the experimental values of the band gap for InAs and InSb, respectively. We repeat the procedure at 0 and 300 K. In Figs. S1 and S2 we show the computed band gap at the Γ point for InAs and InSb as a function of $c_{\mathrm{As}}^{\mathrm{MBJ}}$ and $c_{\mathrm{Sb}}^{\mathrm{MBJ}}$ for experimental lattice parameters at $T = 0$ and 300 K, respectively. As seen, the experimental band gaps are reproduced assuming $c_{\mathrm{As}}^{\mathrm{MBJ}} = 1.160$ for InAs and $c_{\mathrm{Sb}}^{\mathrm{MBJ}} = 1.205$ for InSb at 0 K while we need $c_{As}^{\mathrm{MBJ}} = 1.108$ for InAs and $c_{\mathrm{Sb}}^{\mathrm{MBJ}} = 1.146$ for InSb at 300 K. In this way, we have obtained information on the behaviour and the possible range of c^{MBJ} for the bulk systems.

Using the values of the c^{MBJ} obtained from the bulk, the superlattice shows a metallic phase, then, we assume that c^{MBJ} is not a transferable quantity. Therefore, we slightly increase its value and use a single value of $c^{\mathrm{MBJ}} = 1.22$ for all atoms of the superlattice.

III. OPTICAL PROPERTIES OF SUPERLATTICE

In Figs. S3 and S4 we show the optical spectra for InAs/$\mathrm{InAs_{0.625}Sb_{0.375}}$ obtained at a_{GaSb}=6.096 Å and a_{AlSb}=6.1355 Å, respectively.

---

* ghussain@magtop.ifpan.edu.pl
† gcuono@magtop.ifpan.edu.pl
‡ autieri@magtop.ifpan.edu.pl

[1] I. Vurgaftman, J. R. Meyer, and L. R. Ram-Mohan, “Band parameters for III–V compound semiconductors and their alloys,” *Journal of Applied Physics*, vol. 89, no. 11, pp. 5815–5875, 2001.

[2] D. Kriegner, C. Panse, B. Mandl, K. A. Dick, M. Keplinger, J. M. Persson, P. Caroff, D. Ercolani, L. Sorba, F. Bechstedt, J. Stangl, and G. Bauer, “Unit cell structure of crystal polytypes in InAs and InSb nanowires,” *Nano Letters*, vol. 11, no. 4, pp. 1483–1489, 2011. PMID: 21434674.

[3] M. Gajdoš, K. Hummer, G. Kresse, J. Furthmüller, and F. Bechstedt, “Linear optical properties in the projector-augmented wave methodology,” *Phys. Rev. B*, vol. 73, p. 045112, Jan 2006.

[4] F. Tran and P. Blaha, “Accurate band gaps of semiconductors and insulators with a semilocal exchange-correlation potential,” *Physical review letters*, vol. 102, no. 22, p. 226401, 2009.

[5] O. Madelung, U. Rossler, and M. Schulz, vol. 41A1b. Springer-Verlag, Berlin, 2002.

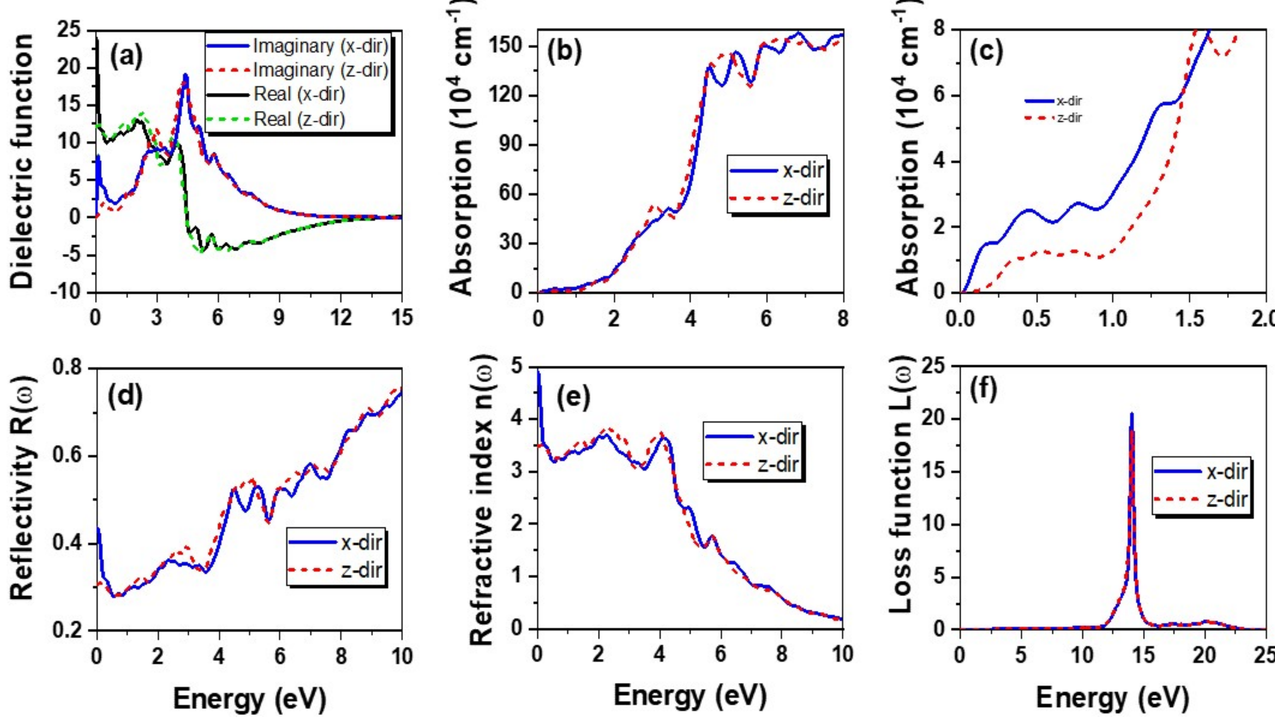

FIG. 3. Frequency-dependent optical properties of $InAs/InAs_{0.625}Sb_{0.375}$ superlattice with lattice constant at T=300 K that is a_{GaSb}=6.0959 Å. (a) Real and imaginary parts of the dielectric function. (b) Absorption spectra in the frequency-range between 0 and 8 eV. (c) Absorption spectra in the IR region. (d) Reflectivity. (e) Refractive index. (f) Energy loss function. The x-dir and z-dir indicate the directions of the electric field polarized perpendicular and parallel to c-axis of the SL.

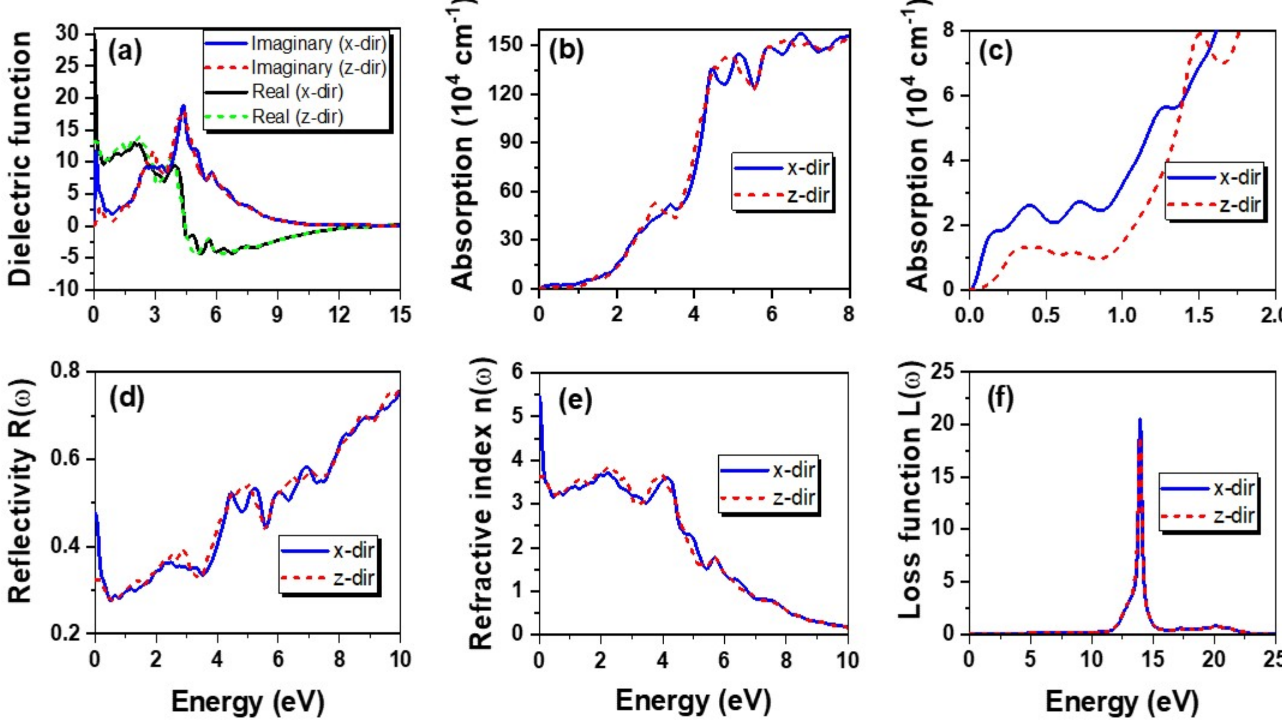

FIG. 4. Frequency-dependent optical properties of $InAs/InAs_{0.625}Sb_{0.375}$ superlattice with lattice constant at T=300 K that is a_{AlSb}=6.1355 Å. Real and imaginary parts of the dielectric function. (b) Absorption spectra in the frequency-range between 0 and 8 eV. (c) Absorption spectra in the IR region. (d) Reflectivity. (e) Refractive index. (f) Energy loss function. The x-dir and z-dir indicate the directions of the electric field polarized perpendicular and parallel to c-axis of the SL.

3.3 PAPER II: 2D materials and heterostructures

The exceptional crystal structures of 2D TMDs and their outstanding electronic attributes make them potential materials in applications including electronics, photonics, and optoelectronics [79-82]. Intriguingly, upon integration of 2D materials with other 2D structures in the form of heterostructures are exemplified to be quite appealing. Specifically, the 2D TMDs could be skillfully bring-together thereby fabricating various heterostructures or superlattices possessing exotic properties that cannot be acquired from isolated 2D material, thus providing the opportunities to explore and investigate the novel applications for the nanodevices [83-85]. The hybrid structures between the different 2D materials can be obtained using different approaches, for instance, the mechanical exfoliation followed by the pick-up-and-transfer technique can be used to create 2D layered heterostructures, but chemical vapor deposition (CVD) enables the direct growth of TMDs layers that are lattice aligned for the heterostructures. Moreover, the monolayer TMD on a wide scale can be synthesized on large scale with seeding promoter-assisted-CVD. Based on the choice of seeding promoter and its capacity to adhere to substrates, this strategy was subsequently adapted for the construction of a range of vertical and lateral hybrid-structures. Besides, it is demonstrated that the technique is independent of lattice mismatch among the combining materials (2D and TMD) to create vertical or lateral heterostructures [91-93, 137]. One-step or two-step CVD synthesis have both been used to effectively produce a number of lateral heterostructures, including MoS_2/WSe_2, NbS_2/MoS_2, $MoS_2/MoSe_2$, and $ReS_2/ReSe_2$, MoS_2/WS_2.

A novel class of 2D materials MA_2Z_4, (where M represents a Transition metal, A stands for group IV element, while Z is group V element) has received considerable attention owing to their exceptional properties [117]. The $MoSi_2N_4$ is first 2D material of this group, which was successfully grown using the CVD method over a big surface of 15 mm by 15 mm. This septuple-atomic-layer semiconducting material (N-Si-N-Mo-N-Si-N) may be viewed of as the three atom thick MoN_2 sandwiched between the two SiN layers with indirect band gap of about 1.94 eV. The elastic modulus of a monolayer of $MoSi_2N_4$ is about four times greater than that of a single layer of MoS_2, and the carrier mobilities of holes and electrons are correspondingly four to six times greater. Moreover, calculations using density functional theory predict the existence of a novel family called MA_2Z_4 (M is Transition metal, A is IV element, and Z is V element). The extraordinary attributes of these materials have been the subject of several research to date [118, 119, 121, 122, 124, 125, 138, 139]. Motivated by the previously reported 2D materials and their heterostructures, we investigate here the 2D monolayers XSi_2N_4 (X = Mo, W, and Ti), and the vertical and lateral heterostructures ($MoSi_2N_4/WSi_2N_4$, and $MoSi_2N_4/TiSi_2N_4$) of this new family. Both, the monolayers and heterostructures are thermodynamically stable with outstanding electronic properties. From the electronic band structures, we noticed that the band gap varies from the visible to infrared region employing their applications in different optoelectronic devices.

Applied Surface Science 590 (2022) 153131

Contents lists available at ScienceDirect

Applied Surface Science

journal homepage: www.elsevier.com/locate/apsusc

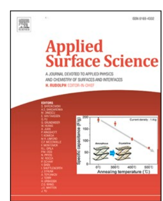

Full Length Article

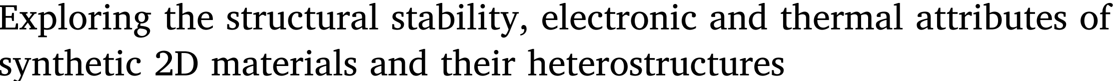

Exploring the structural stability, electronic and thermal attributes of synthetic 2D materials and their heterostructures

Ghulam Hussain [a,*], Mazia Asghar [b], Muhammad Waqas Iqbal [b], Hamid Ullah [b,*], Carmine Autieri [a]

[a] International Research Centre MagTop, Institute of Physics, Polish Academy of Sciences, Aleja Lotników 32/46, PL-02668 Warsaw, Poland
[b] Department of Physics, Riphah International University, Campus Lahore, Pakistan

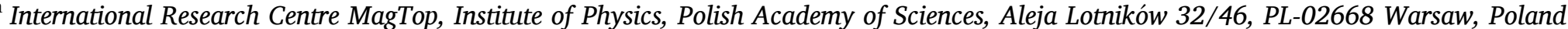

A B S T R A C T

Based on first-principles calculations, we have investigated the structural stability, electronic structures, and thermal properties of the monolayer XSi_2N_4 (X = Ti, Mo, W) and their lateral (LH) and vertical heterostructures (VH). We find that these heterostructures are energetically and dynamically stable due to high cohesive and binding energies, and no negative frequencies in the phonon spectra. The XSi_2N_4 (X = Ti, Mo, W) monolayers, the $TiSi_2N_4/MoSi_2N_4$-LH, $MoSi_2N_4/WSi_2N_4$-LH, and $MoSi_2N_4/WSi_2N_4$-VH possess a semiconducting nature with an indirect band gap ranging from 0.30 to 2.60 eV. At room temperature, the C_v values are found to be between 100 and 416 $JK^{-1}mol^{-1}$ for the monolayers and their heterostructures, suggesting the better ability to retain heat with respect to transition metal dichalcogenides. Our study unveils the excellent attributes of XSi_2N_4 2D monolayers and their heterostructures, proposing them as potential candidates in nano-electronics and thermoelectric applications.

1. Introduction

Due to the monolayer limit, the two-dimensional (2D) materials have distinct physical properties and thus are employable in a wide range of device applications [1–9]. Graphene, the first 2D material, has been widely studied since its discovery [3,10]. It was expected to be a suitable layered structure for the new generation of nanoelectronic devices thanks to its high carrier mobility. However, graphene's zero band gap reminds us that it cannot be effective in many device applications [11–13]. On the other hand, transition metal dichalcogenides (TMDCs) are explored to exhibit tunable band gaps, but on account of practical applications, their relatively low carrier mobilities cannot be neglected [1,14,15]. For instance, MoS_2 possesses carrier mobility of approximately 200 $cm^2V^{-1}s^{-1}$ for holes and 72 $cm^2V^{-1}s^{-1}$ for electrons [14], which are much lower in magnitude than that of graphene and even much smaller than Si (480 $cm^2V^{-1}s^{-1}$ for hole and 1350 $cm^2V^{-1}s^{-1}$ for electron) [14,16]. In recent years, from the fundamental and applicative point of view, we have assisted to tremendous efforts in the investigation of the topological and magnetic properties of the 2D materials and quasi-2D materials [17–25].

Recently, the discovery of novel 2D materials family, XA_2Z_4 (X = Transition metal, A = IV element, Z = V element) [26] has attracted broad consideration due to the outstanding properties they demonstrate. The first member of this assembly is the $MoSi_2N_4$ that was successfully produced via chemical vapor deposition (CVD) process with a large area of size 15 mm × 15 mm. This semiconducting material with a septuple-atomic-layer configuration (N-Si-N-Mo-N-Si-N) can be regarded as a MoN_2 layer sandwiched in two SiN layers, exhibiting an indirect band gap of almost 1.94 eV. The monolayer of $MoSi_2N_4$ depicts an elastic modulus that is roughly four times larger than MoS_2, and the carrier mobilities of holes and electrons are also four to six times that of a single layer of MoS_2. Moreover, a new family, namely XA_2Z_4 (X = Transition metal, A = IV element, Z = V element) is anticipated by density functional theory (DFT) calculation. So far, several studies have been carried out describing the exceptional features of these materials [27–34].

Designing vertically stacked or laterally stitched two-dimensional heterostructures between 2D materials is an effective technique to unravel new features and extend their applications to electronics, detectors, electroluminescence, and photovoltaics [35–45]. Several experimental techniques such as physical vapor transport, CVD, plasma-assisted deposition, thermal decomposition, and vapor phase growth method have been utilized to synthesize the lateral heterostructures (LH) and vertical heterostructures (VH) [41,46–51]. Recently, the vertically stacked bilayer of $MoSi_2N_4$ have been studied using first-principles calculations, which reports the effect of strain on the electronic band gap, the bilayer $MoSi_2N_4$ showed a decrease in the band gap as the vertical strain was increased; and at around 22% strain, the bilayer revealed a semiconducting to metal transition [31]. Also, the

* Corresponding authors.
E-mail addresses: ghussain@ifpan.edu.pl (G. Hussain), hamid.ullah@riphah.edu.pk (H. Ullah).

https://doi.org/10.1016/j.apsusc.2022.153131
Received 21 January 2022; Received in revised form 9 March 2022; Accepted 15 March 2022
Available online 23 March 2022
0169-4332/© 2022 Elsevier B.V. All rights reserved.

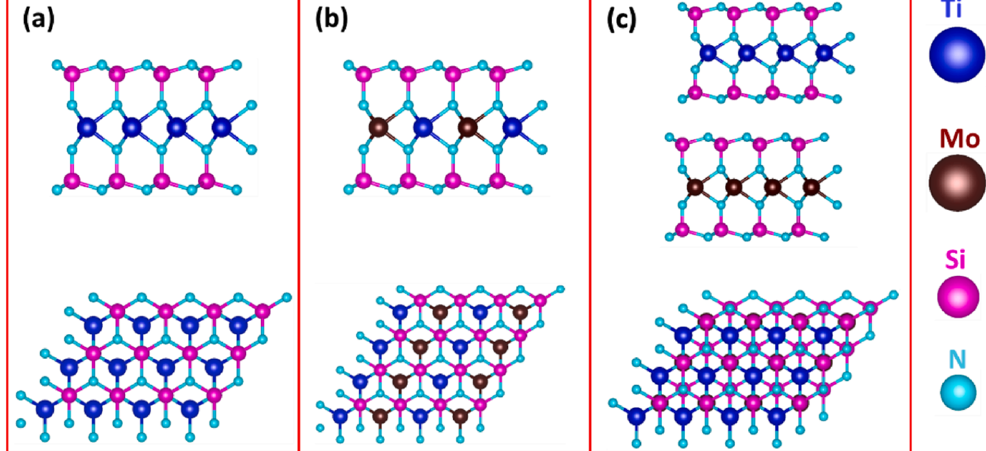

Fig. 1. Side and top views of the atomic structures of (a) XSi_2N_4 monolayer, (b) lateral heterostructure (LH), and (c) vertical heterostructure (VH).

band gap decreases as a function of the electric field for both the $MoSi_2N_4$, and WSi_2N_4 bilayers, respectively [28]. Likewise, the vertical heterostructures of $MoSi_2N_4$ and $MoGe_2N_4$ have been reported, where the electronic properties and ferroelectricity are investigated [29,30]. Nonetheless, the van der Waals heterostructures of this class are not explored thoroughly and demand a detailed study. In addition, the laterally stitched heterostructures of this novel family are not reported so far.

In this work using first-principle calculations, we carry out a detailed study of XSi_2N_4 (X = Ti, Mo, W) 2D monolayers and their lateral and vertical heterostructures such as $TiSi_2N_4/MoSi_2N_4$ and $MoSi_2N_4/WSi_2N_4$. All the compounds are investigated in their 2H crystal structure. The cohesive energies and the absence of imaginary phonon modes in the phonon dispersions exposed the structural stability of XSi_2N_4 systems and their lateral and vertical heterostructures. Since the electronic properties calculated by DFT are usually in poor agreement with the experiments, principally the band gap, the Hybrid functional (HSE06) is applied to accurately approximate the electronic band structures. Both, the density of states and electronic band structures of XSi_2N_4 2D materials and their LHs and VHs indicated trivial indirect band gaps. In contrast, a semiconducting to metallic transition is observed in the vertical heterostructure of $TiSi_2N_4/MoSi_2N_4$. Compared to parent XSi_2N_4 materials, the lateral and vertical heterostructures show the highest free energy and heat capacity values. Our theoretical investigations could pave the path for designing novel nanoelectronic devices based on XSi_2N_4 and their hetero-systems.

2. Methodology

We performed first-principles calculation via the Vienna ab initio simulation package (VASP) [52,53] using density functional theory (DFT). Both the Heyd-Scuseria-Ernzerhof (HSE06) and the generalized gradient approximation with PBE form [27] and [28] are adopted to calculate the electronic properties [54,55]. For relaxation, an energy cutoff of 500 eV and a mesh of 15 × 15 × 1 k-points were chosen. The periodic structures in the perpendicular direction of 2D material and heterostructure were separated with a vacuum layer of approximately 20 Å, which would avoid spurious interactions. Our calculations were converged by setting the convergence criteria to 0.01 eV/Å and energy 10^{-7} eV. To study the dynamical stability of XSi_2N_4 monolayers and that of LHs and VHs, PHONOPY code using a 4 × 4 × 1 supercell was employed for calculating the phonon band structures [56]. Also, the thermal properties such as the heat capacity, free energy and entropy were explored using phonon calculations.

3. Results and discussions

3.1. Structural stability

The optimized structures for XSi_2N_4 (X = Ti, Mo, W) monolayers and their heterostructures are visualized in Fig. 1, where the (a), (b) and (c) panels depict the monolayer, lateral heterostructure (LH) and vertical heterostructures (VH), respectively. It can be seen that XSi_2N_4 (X = Ti, Mo, W) possesses a honeycomb structure consisting of Ti/Mo/W, Si and N atoms. The side view illustrates that this structure is stacked by seven atomic layers of N-Si-N-X-N-Si-N that exhibits a sandwich structure of MoN_2 layer by two SiN bilayers. We noticed the optimized lattice constants for XSi_2N_4 (X = Ti, Mo, W) monolayers to be $a = b = 2.932$, 2.909 and 2.915 Å, respectively. These lattice constants are in perfect agreement with the calculated lattice parameters in the literature [26,27,57,58]. Here, we consider the lateral AA- stitching for the LHs (Fig. 1b) and vertical AB-stacking for the VHs (Fig. 1c), the heterostructures obtained are $TiSi_2N_4/MoSi_2N_4$-LH, $TiSi_2N_4/MoSi_2N_4$-VH, $MoSi_2N_4/WSi_2N_4$-LH, and $MoSi_2N_4/WSi_2N_4$-VH. Fig. 1(b) depicts the side and top views of these heterostructures exhibiting the stacking of seven atomic layers of N-Si-N-X-N-Si-N, where X represents alternative Mo, W and Ti atoms. The strongly bonding of seven-layers of atoms give rise to a sandwich structure, comprising alternative MoN_2 and TiN_2 (MoN_2 and WN_2) layers and two SiN bilayers. We noticed the optimized lattice constants for $MoSi_2N_4/WSi_2N_4$-LH and $TiSi_2N_4/MoSi_2N_4$-LH to be 5.824 and 5.841 Å, respectively. In the AA-stacking of VHs, all atoms i.e. the X, Si and N atoms of one monolayer of XSi_2N_4 are located exactly above the X, Si and N atoms of the other XSi_2N_4 layer. Whereas, in AB-stacking, all the atoms in the one XSi_2N_4 layer are staggered with respect to another XSi_2N_4 monolayer, as depicted in Fig. 1c. Based on total ground state energy calculations, the ground state is AB stacking [26,28,29].

In order to check the stability of XSi_2N_4 monolayers and that of LHs and VHs, we used the total ground state energies to compute the cohesive energies. In addition, the phonon dispersions are calculated to determine their dynamical stability, which can enable the use of the studied systems in the device application. In the monolayer case of XSi_2N_4, the cohesive energy is calculated by [59,60];

$$\mathbf{E}_c = \frac{1\mathbf{E}_X + 2\mathbf{E}_{Si} + 4\mathbf{E}_N - \mathbf{E}_{XSi_2N_4}}{1+2+4}$$

Here, E_X, E_{Si}, E_N and $E_{XSi_2N_4}$ are total ground state energies of isolated X, Si, N atoms and monolayer XSi_2N_4, respectively. The cohesive energies for $TiSi_2N_4$, $MoSi_2N_4$ and that of WSi_2N_4 are evaluated to be 5.562, 5.589 and 5.653 eV/atom, respectively. By comparing these values with that of graphene (7.46 eV/atom), MoS_2 (4.98 eV/atom) and

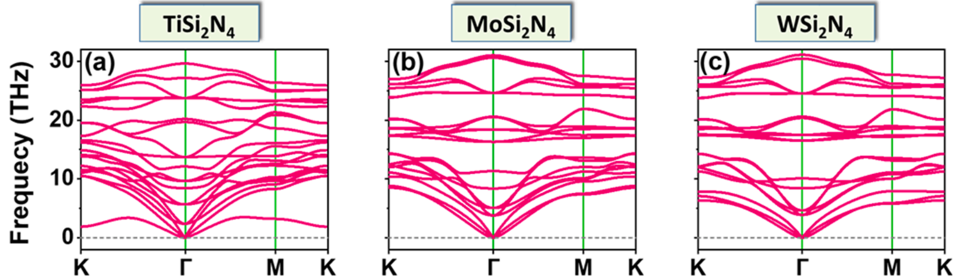

Fig. 2. Phonon bandstructures for XSi_2N_4 (X = Ti, Mo, W) monolayers revealing no imaginary modes.

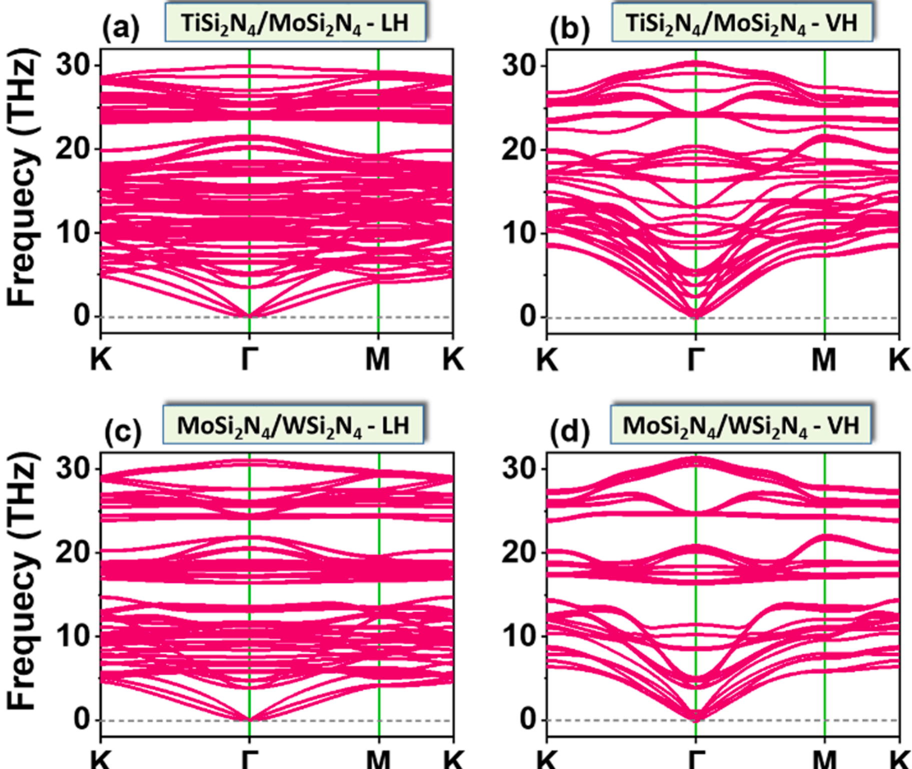

Fig. 3. Calculated phonon dispersion curves of the lateral and vertical heterostructures for (a) $TiSi_2N_4/MoSi_2N_4$-LH, (b) $TiSi_2N_4/MoSi_2N_4$-VH, (c) $MoSi_2N_4/WSi_2N_4$-LH and (d) $MoSi_2N_4/WSi_2N_4$-VH.

phosphorene (3.30 eV/atom) [61–63], we noted that they are smaller than graphene but larger than MoS_2, which indicate the better stability. For the heterostructures, the binding energies are estimated to determine the stability, it is given by [64];

$$E_b = E_{heterostructure} - E_{X^1Si_2N_4} - E_{X^2Si_2N_4}$$

Where$E_{heterostructure}$, denotes the total energy of the heterostructure while $E_{X^1Si_2N_4}, E_{X^2Si_2N_4}$ represent the ground state energies of the two monolayers involved in the formation of LH or VH. The binding energies are calculated as 0.859 and 0.104 eV (0.045 and 0.050 eV) for lateral heterostructures (vertical heterostructures) of $TiSi_2N_4/MoSi_2N_4$ and $MoSi_2N_4/WSi_2N_4$, respectively. The binding energies of vertical heterostructures are comparable with that of heterostructures of $MoGe_2N_4/MoSi_2N_4$ (ranging from 0.024 to 0.16 eV) [30], InSe/SiGe (0.034–0.052 eV) [65], and MoS_2/WS_2 (0.033 eV) [66], respectively.

To examine the dynamical stability of XSi_2N_4 (X = Ti, Mo, W) monolayers and that of heterostructures, we carried out the phonon dispersion calculations as shown in Figs. 2 and 3. The finite difference method is employed to calculate the phonon spectra using the Phonopy code [56] with VASP [67] as a calculator. From the phonon dispersion curves shown in Fig. 2, it is confirmed that all the three XSi_2N_4 (X = Ti, Mo, W) monolayers are dynamically stable due to the absence of imaginary modes. Similarly in Fig. 3, the calculated phonon band spectra along the Brillouin zone's high symmetry directions (K-Γ-M−K) for both the lateral and vertical heterostructures reveal no imaginary frequency at the Γ-point, indicating the dynamical stability of the corresponding systems. Interestingly, the soft acoustic mode of $TiSi_2N_4$ having a frequency of ~ 2 THz at the K-point (shown in Fig. 2a), becomes harder (increase in the frequency at same wave-vector) when $TiSi_2N_4$ is brought in combination with any XSi_2N_4 monolayer. This makes $TiSi_2N_4$ easier to synthesize in combination with other compounds. For $TiSi_2N_4/MoSi_2N_4$-LH and $TiSi_2N_4/MoSi_2N_4$-VH, the hardening of this mode can be seen in Fig. 3a and 3b, respectively. The hardening of ~ 2 THz acoustic mode occurring at the K-point can be ascribed to the enhanced coupling at this wave-vector [68,69].

3.2. Electronic properties

To understand the contribution of different orbitals from various elements that characterize our systems' electronic attributes, the total

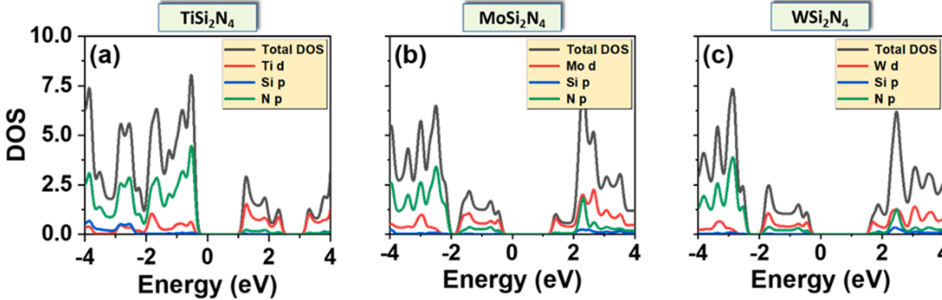

Fig. 4. Calculated TDOS and PDOS of (a) $TiSi_2N_4$, (b) $MoSi_2N_4$ and (c) WSi_2N_4 monolayers. The Fermi-level is set to zero energy.

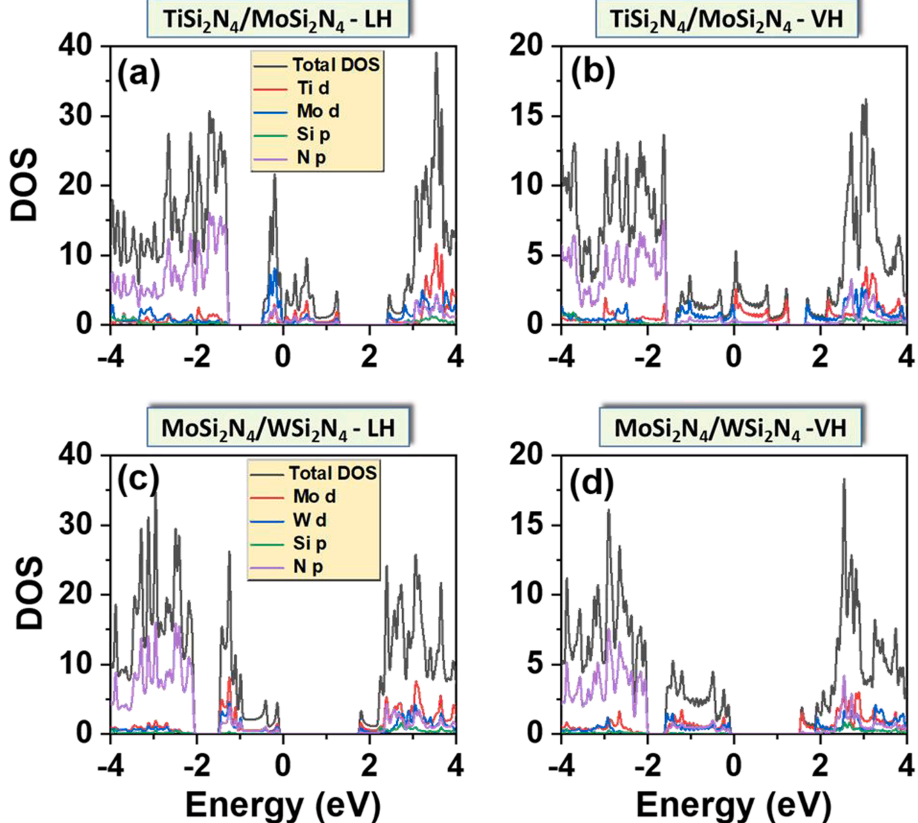

Fig. 5. Calculated TDOS and PDOS of (a) $TiSi_2N_4/MoSi_2N_4$-LH, (b) $TiSi_2N_4/MoSi_2N_4$-VH, (c) $MoSi_2N_4/WSi_2N_4$-LH, and (d) $MoSi_2N_4/WSi_2N_4$-VH. The Fermi-level is set to zero energy.

density of states (TDOS) and partial density of states (PDOS) are computed. Fig. 4 illustrates the TDOS and PDOS for the respective XSi_2N_4 monolayers. For the monolayer $TiSi_2N_4$, the valence band maximum (VBM) is mainly dominated by N atoms '*p*' orbitals with slight contribution from Ti-*d* orbitals, while the conduction band minima (CBM) is principally originated by the Ti-*d* orbital, as illustrated in Fig. 4a. In the case of $MoSi_2N_4$, and WSi_2N_4, however, both the VBMs and CBMs maximally arise due to the Mo-/W-*d* orbitals, which are located in the middle of each monolayer structure (Fig. 4b, c).

In Fig. 5, we investigate the TDOS and PDOS for the heterostructures including $TiSi_2N_4/MoSi_2N_4$-LH, $TiSi_2N_4/MoSi_2N_4$-VH, $MoSi_2N_4/WSi_2N_4$-LH, and $MoSi_2N_4/WSi_2N_4$-VH. Fig. 5(a), exhibits that the band gap decreases to a very small value of 0.137 eV for $TiSi_2N_4/MoSi_2N_4$-LH whereby the VBM is dominated by Mo-*d* orbitals with little contributions from N-*p* and Ti-d orbitals, whereas the CBM is maximally originated by N-*p* and Ti-*d* orbitals. Interestingly, the $TiSi_2N_4/MoSi_2N_4$-VH shows metallicity thereby appearing a considerable DOS at the Fermi level as shown in Fig. 5b. This metallic behavior of the VH is mainly contributed by Ti '*d*' orbitals and partly by Mo '*d*' and N '*p*' orbitals. Differently from these two heterostructures of $TiSi_2N_4/MoSi_2N_4$, the lateral and vertical heterostructures of $MoSi_2N_4/WSi_2N_4$ manifest large band gaps as shown in Fig. 5c and d. For $MoSi_2N_4/WSi_2N_4$-LH, both the VBM and CBM are dominated mainly by the 'd' orbitals of Mo and W. Similarly, the VBM of $MoSi_2N_4/WSi_2N_4$-VH maximally arise due to the '*d*' orbitals of Mo and W, while the CBM is contributed by Mo '*d*' orbitals only. In conclusion, all the structures including XSi_2N_4 materials and their heterostructures reveal trivial insulating behavior, except the VH of $TiSi_2N_4/MoSi_2N_4$, which is metallic.

The electronic band structures were calculated to further investigate the electronic properties of XSi_2N_4 (X = Ti, Mo, W) monolayers and their heterostructures. Since the electronic band gaps calculated by DFT are usually in poor agreement with the experiments and mostly underestimated [70–72], therefore, the Hybrid functional (HSE06) [54] is applied to approximate the electronic band structures. Fig. 6

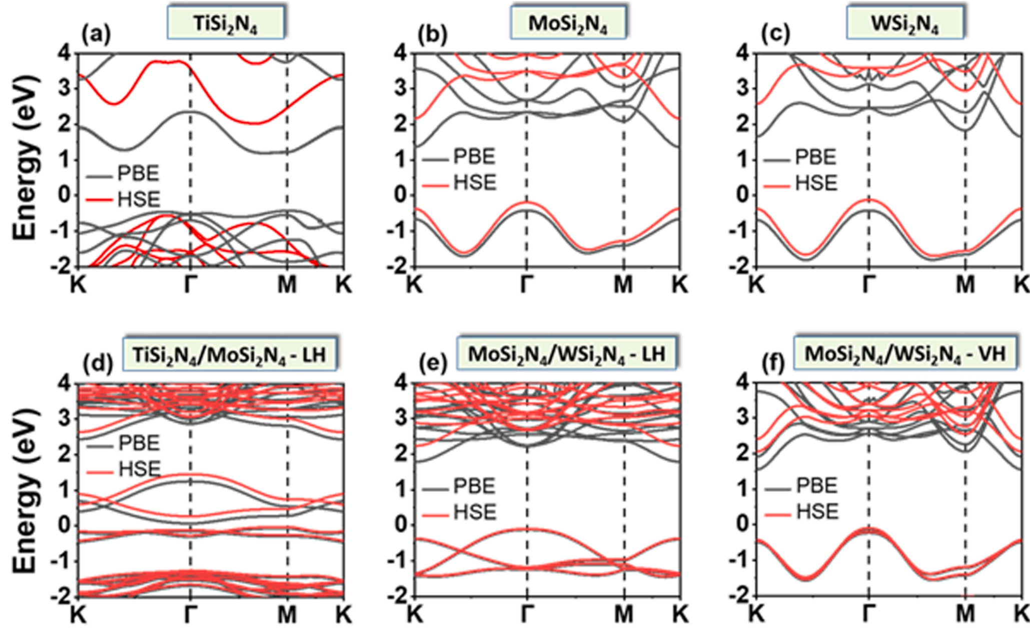

Fig. 6. Electronic band structures calculated through PBE (black color) and HSE06 (red color) for (a) $TiSi_2N_4$, (b) $MoSi_2N_4$, (c) WSi_2N_4, (d) $TiSi_2N_4/MoSi_2N_4$-LH, (e) $MoSi_2N_4/WSi_2N_4$-LH and (f) $MoSi_2N_4/WSi_2N_4$-VH. (For interpretation of the references to color in this figure legend, the reader is referred to the web version of this article.)

Table 1
Calculated electronic band gaps of XSi_2N_4 materials and their lateral and vertical heterostructures using PBE and HSE06.

Material	PBE Band gap (eV)	HSE Band gap (eV)
$TiSi_2N_4$	1.63	2.40
$MoSi_2N_4$	1.74	2.35
WSi_2N_4	2.12	2.60
$TiSi_2N_4$/ $MoSi_2N_4$ – LH	0.14	0.30
$MoSi_2N_4/WSi_2N_4$ – LH	1.90	2.34
$MoSi_2N_4/WSi_2N_4$ – VH	1.70	2.15

demonstrates the band structures of XSi_2N_4 materials and heterostructures computed through both PBE and HSE06 potentials. The XSi_2N_4 (X = Ti, Mo, W) monolayers possess an indirect band gap of 2.61 eV, 2.35 eV, and 2.69 eV for $TiSi_2N_4$, $MoSi_2N_4$, and WSi_2N_4, respectively, as shown in Fig. 6a, b, c. For the $TiSi_2N_4/MoSi_2N_4$-LH, the maximum of the valence band (VBM) appears at the M−point, while the minimum of the conduction band (CBM) occurs at the Γ-point (Fig. 6d). On the other hand, in the cases of $MoSi_2N_4/WSi_2N_4$-LH and $MoSi_2N_4/WSi_2N_4$-VH, the VBM emerges at Γ-point, whereas the CBM occurs at the K-point, as can be seen in Fig. 6e, f, suggesting that the indirect band gap nature still prevails. The values of the indirect band gaps are determined to be ~ 0.30, 2.34, and 2.15 eV for the $TiSi_2N_4/MoSi_2N_4$-LH, $MoSi_2N_4/WSi_2N_4$-LH, and $MoSi_2N_4/WSi_2N_4$-VH, respectively, which could make them promising for the application in solar cells and optoelectronic

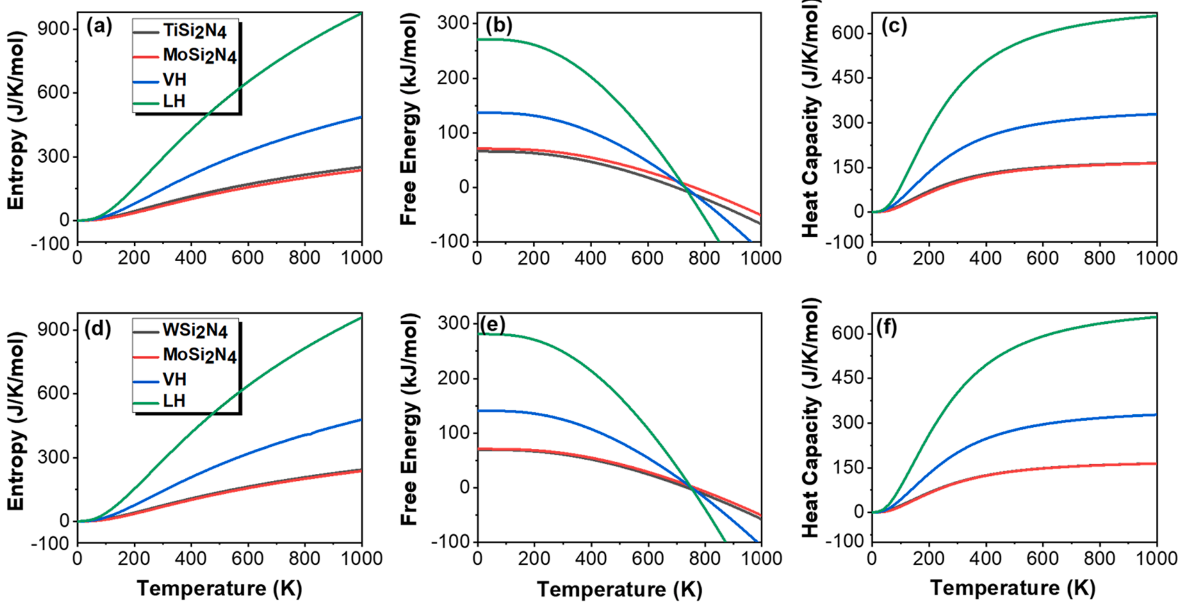

Fig. 7. Thermal properties such as entropy, free energy and heat capacity. The top panels (a), (b) and (c) represent $TiSi_2N_4$, $MoSi_2N_4$ and their lateral and vertical heterostructures, while the lower panel characterizes $MoSi_2N_4$, WSi_2N_4, and their lateral and vertical heterostructures.

devices [73–76]. The calculated band gap values are tabulated in Table 1, which are in agreement with the available literature [27,31,33]. A slight difference in band gaps may arise due to the difference in lattice parameters.

3.3. Thermal properties

Based on the stable phonon dispersions of XSi_2N_4 (X = Ti, Mo, W) monolayers and their heterostructures, the thermal characteristics including entropy (S), Helmholtz free energy (F), and heat capacity C_v are calculated as shown in Fig. 7. The entropy of all the systems rises steadily with the temperature, consistently with the fact that increasing the temperature gives rise to several microstates in the system W, which results in an increase in the entropy logarithmically according to the Boltzmann's entropy formula ($S = k_B \log W$, where k_B is the Boltzmann constant). On the other hand, the Helmholtz free energy, F, is observed to decline with temperature, as shown in Fig. 7b and 7e, which agrees with$F(T) = U(T) - TS(T)$; $U(T)$ is the lattice internal energy. Furthermore, we investigate the heat capacity C_v of XSi_2N_4 (X = Ti, Mo, W) monolayers and their heterostructures as a function of temperature as illustrated in Fig. 7c and 7f. Comparable heat capacities of $TiSi_2N_4$, $MoSi_2N_4$ and WSi_2N_4 are observed as reported in Fig. 7c and 7f. Intriguingly, the heat capacity increases for the VHs and further enhances for the LHs. At room temperature, the C_v values are estimated to be 106.1, 100.5, 100.8, 206.5, 415.6, 201.3 and 402.3 $JK^{-1}mol^{-1}$ for $TiSi_2N_4$, $MoSi_2N_4$, WSi_2N_4, $TiSi_2N_4/MoSi_2N_4$-VH, $TiSi_2N_4/MoSi_2N_4$-LH, $MoSi_2N_4/WSi_2N_4$-VH and $MoSi_2N_4/WSi_2N_4$-LH, respectively. Our estimated values of C_v are relatively higher than PbSe and PbTe [77,78] (which are thought to be excellent thermoelectric materials), suggesting the better ability of XSi_2N_4 (X = Ti, Mo, W) monolayers and their heterostructures to retain heat. The heat capacity of XSi_2N_4 (X = Ti, Mo, W) monolayers takes the lead to approach the Dulong-petit asymptotic value (i.e.$C_v = 3NR$, where N is the number of atoms and R is the universal gas constant) at around T ~560 K. Whereas, the VHs of $TiSi_2N_4/MoSi_2N_4$, and $MoSi_2N_4/WSi_2N_4$ approach this asymptote at a relatively higher temperature, near T ~650 K, and LHs of $TiSi_2N_4/MoSi_2N_4$, and $MoSi_2N_4/WSi_2N_4$ required a higher temperature of around T~750 K and T~850 K to approach this value. From this investigation, we found that C_v is consistent with the entropy we computed here since the variation of entropy corresponds to the integral of (C_v/T) over a given temperature range.

4. Conclusions

The structural stability, electronic properties and thermal characteristics of XSi_2N_4 (X = Ti, Mo, W) monolayers and their lateral and vertical heterostructures are explored using density functional theory. We noticed that interfacing two different 2D structures either laterally or vertically, significantly tunes the physical properties of the parent 2D monolayers that may have technological impact in many potential applications. The structural stability of these systems was confirmed by the cohesive energies which are based on the total ground state energies and the phonon dispersions revealing the dynamical stability. Apart from their stability, our results illustrated that the lateral and vertical heterostructures present outstanding electronic and thermal features. All the three monolayers i.e. $TiSi_2N_4$, $MoSi_2N_4$, and WSi_2N_4 revealed indirect band gaps. Remarkably, a semiconducting to metallic transition is observed in the VH of $TiSi_2N_4/MoSi_2N_4$, while the LH of $TiSi_2N_4/MoSi_2N_4$ manifested a small band gap. Both the lateral and vertical heterostructures of $MoSi_2N_4/WSi_2N_4$ revealed semiconducting nature with modifications in their band gaps with respect to the parent monolayers. Compared to the transition metal dichalcogenides, the monolayers XSi_2N_4 and their heterostructures bear the highest values for the free energy and heat capacity. The study suggests that both the XSi_2N_4 2D monolayers and their heterostructures could be promising in the next-generation optoelectronics and nanoelectronics.

CRediT authorship contribution statement

Ghulam Hussain: Data curation, Writing – original draft. **Mazia Asghar:** Conceptualization, Methodology. **Muhammad Waqas Iqbal:** Visualization, Investigation. **Hamid Ullah:** Writing – review & editing. **Carmine Autieri:** Supervision.

Declaration of Competing Interest

The authors declare that they have no known competing financial interests or personal relationships that could have appeared to influence the work reported in this paper.

Acknowledgments

This work is supported by the Foundation for Polish Science through the international research agendas program co-financed by the European Union within the smart growth operational program. We acknowledge the access to the computing facilities of the Interdisciplinary Center of Modeling at the University of Warsaw, Grants No. GB84-0 and No. GB84-7. The authors extend their appreciation to Riphah International University for funding this work under project number R-ORIC-21/FEAS-10.

References

[1] Q.H. Wang, K. Kalantar-Zadeh, A. Kis, J.N. Coleman, M.S. Strano, Electronics and optoelectronics of two-dimensional transition metal dichalcogenides, Nat. Nanotechnol. 7 (11) (2012) 699–712.
[2] W. Hou, H. Mi, R. Peng, S. Peng, W. Zeng, Q.u. Zhou, First-principle insight into Ga-doped MoS_2 for sensing SO_2, SOF_2 and SO_2F_2, Nanomaterials 11 (2) (2021) 314, https://doi.org/10.3390/nano11020314.
[3] K.S. Novoselov, A.K. Geim, S.V. Morozov, D. Jiang, Y. Zhang, S.V. Dubonos, I. V. Grigorieva, A.A. Firsov, Electric field effect in atomically thin carbon films, Science 306 (5696) (2004) 666–669.
[4] T. Yu, Z. Zhao, Y. Sun, A. Bergara, J. Lin, S. Zhang, H. Xu, L. Zhang, G. Yang, Y. Liu, Two-dimensional PC6 with direct band gap and anisotropic carrier mobility, J. Am. Chem. Soc. 141 (4) (2019) 1599–1605.
[5] L. Ci, L.i. Song, C. Jin, D. Jariwala, D. Wu, Y. Li, A. Srivastava, Z.F. Wang, K. Storr, L. Balicas, F. Liu, P.M. Ajayan, Atomic layers of hybridized boron nitride and graphene domains, Nat. Mater. 9 (5) (2010) 430–435.
[6] Y. Zhang, Y.-W. Tan, H.L. Stormer, P. Kim, Experimental observation of the quantum Hall effect and Berry's phase in graphene, Nature 438 (7065) (2005) 201–204.
[7] Y.i. Lin, T.V. Williams, J.W. Connell, Soluble, exfoliated hexagonal boron nitride nanosheets, The Journal of Physical Chemistry Letters 1 (1) (2010) 277–283.
[8] W. Wu, P. Lu, Z. Zhang, W. Guo, Electronic and magnetic properties and structural stability of BeO sheet and nanoribbons, ACS Appl. Mater. Interfaces 3 (12) (2011) 4787–4795.
[9] Z. Zhang, X. Liu, B.I. Yakobson, W. Guo, Two-dimensional tetragonal TiC monolayer sheet and nanoribbons, J. Am. Chem. Soc. 134 (47) (2012) 19326–19329.
[10] A.K. Geim, K.S. Novoselov, The rise of graphene, in: Nanoscience and technology: a collection of reviews from nature journals, World Scientific, 2010, pp. 11-19.
[11] K.S. Novoselov, A.K. Geim, S.V. Morozov, D. Jiang, M.I. Katsnelson, I. Grigorieva, S. Dubonos, Firsov, AA, Two-dimensional gas of massless Dirac fermions in graphene, nature 438 (2005) 197-200.
[12] A. Lherbier, A.R. Botello-Méndez, J.-C. Charlier, Electronic and transport properties of unbalanced sublattice N-doping in graphene, Nano Lett. 13 (2013) 1446–1450.
[13] J. Chen, J. Xi, D. Wang, Z. Shuai, Carrier mobility in graphyne should be even larger than that in graphene: a theoretical prediction, The journal of physical chemistry letters 4 (9) (2013) 1443–1448.
[14] Y. Cai, G. Zhang, Y.-W. Zhang, Polarity-reversed robust carrier mobility in monolayer MoS2 nanoribbons, J. Am. Chem. Soc. 136 (2014) 6269–6275.
[15] K.F. Mak, C. Lee, J. Hone, J. Shan, T.F. Heinz, Atomically thin MoS 2: a new direct-gap semiconductor, Phys. Rev. Lett. 105 (2010), 136805.
[16] G. Ludwig, R. Watters, Drift and conductivity mobility in silicon, Phys. Rev. 101 (1956) 1699.
[17] Y. Ren, Z. Qiao, Q. Niu, Topological phases in two-dimensional materials: a review, Rep. Prog. Phys. 79 (6) (2016) 066501, https://doi.org/10.1088/0034-4885/79/6/066501.
[18] H. Huang, Y. Xu, J. Wang, W. Duan, Emerging topological states in quasi-two-dimensional materials, Wiley Interdisciplinary Reviews: Computational Molecular Science 7 (4) (2017) e1296, https://doi.org/10.1002/wcms.1296.
[19] L. Kou, Y. Ma, Z. Sun, T. Heine, C. Chen, Two-dimensional topological insulators: Progress and prospects, The journal of physical chemistry letters 8 (2017) 1905–1919.

[20] X. Qian, J. Liu, L. Fu, J. Li, Quantum spin Hall effect in two-dimensional transition metal dichalcogenides, Science 346 (2014) 1344–1347.

[21] S. Kumari, D.K. Pradhan, N.R. Pradhan, P.D. Rack, Recent developments on 2D magnetic materials: challenges and opportunities, Emergent Materials (2021) 1–20.

[22] T. Van Thiel, W. Brzezicki, C. Autieri, J. Hortensius, D. Afanasiev, N. Gauquelin, D. Jannis, N. Janssen, D. Groenendijk, J. Fatermans, Coupling charge and topological reconstructions at polar oxide interfaces, Phys. Rev. Lett. 127 (2021), 127202.

[23] A. Lau, T. Hyart, C. Autieri, A. Chen, D.I. Pikulin, Designing Three-Dimensional Flat Bands in Nodal-Line Semimetals, Phys. Rev. X 11 (2021), 031017.

[24] W. Lei, W. Wang, X. Ming, S. Zhang, G. Tang, X. Zheng, H. Li, C. Autieri, Structural transition, metallization, and superconductivity in quasi-two-dimensional layered PdS_2 under compression, Physical Review B 101 (2020), 205149.

[25] W. Wang, B. Wang, Z. Gao, G. Tang, W. Lei, X. Zheng, H. Li, X. Ming, C. Autieri, Charge density wave instability and pressure-induced superconductivity in bulk $1T-NbS_2$, Physical Review B 102 (2020), 155115.

[26] Y.-L. Hong, Z. Liu, L. Wang, T. Zhou, W. Ma, C. Xu, S. Feng, L. Chen, M.-L. Chen, D.-M. Sun, Chemical vapor deposition of layered two-dimensional $MoSi_2N_4$ materials, Science 369 (2020) 670–674.

[27] X. Lv, Y. Xu, B. Mao, G. Liu, G. Zhao, J. Yang, Strain modulation of electronic and optical properties of monolayer $MoSi_2N_4$, Physica E 135 (2022) 114964, https://doi.org/10.1016/j.physe.2021.114964.

[28] Q. Wu, L. Cao, Y.S. Ang, L.K. Ang, Semiconductor-to-metal transition in bilayer $MoSi_2N_4$ and WSi_2N_4 with strain and electric field, Appl. Phys. Lett. 118 (2021), 113102.

[29] T. Zhong, Y. Ren, Z. Zhang, J. Gao, M. Wu, Sliding ferroelectricity in two-dimensional MoA $_2N_4$ (A= Si or Ge) bilayers: high polarizations and Moiré potentials, J. Mater. Chem. A (2021).

[30] D. Pham, Electronic properties of a two-dimensional van der Waals $MoGe_2N_4$/$MoSi_2N_4$ heterobilayer: effect of the insertion of a graphene layer and interlayer coupling, RSC Adv. 11 (2021) 28659–28666.

[31] H. Zhong, W. Xiong, P. Lv, J. Yu, S. Yuan, Strain-induced semiconductor to metal transition in MA_2Z_4 bilayers (M= Ti, Cr, Mo; A= Si; Z= N, P), Physical Review B 103 (2021), 085124.

[32] A. Bafekry, M. Faraji, M.M. Fadlallah, A.B. Khatibani, A. abdolahzadeh Ziabari, M. Ghergherehchi, S. Nedaei, S.F. Shayesteh, D. Gogova, Tunable electronic and magnetic properties of $MoSi_2N_4$ monolayer via vacancy defects, atomic adsorption and atomic doping, Applied Surface Science, 559 (2021) 149862.

[33] A. Bafekry, M. Faraji, D. Hoat, M. Shahrokhi, M. Fadlallah, F. Shojaei, S. Feghhi, M. Ghergherehchi, D. Gogova, $MoSi_2N_4$ single-layer: a novel two-dimensional material with outstanding mechanical, thermal, electronic and optical properties, J. Phys. D Appl. Phys. 54 (2021), 155303.

[34] R. Islam, B. Ghosh, C. Autieri, S. Chowdhury, A. Bansil, A. Agarwal, B. Singh, Tunable spin polarization and electronic structure of bottom-up synthesized $MoSi_2N_4$ materials, Physical Review B 104 (2021) L201112.

[35] L. Britnell, R.M. Ribeiro, A. Eckmann, R. Jalil, B.D. Belle, A. Mishchenko, Y.-J. Kim, R.V. Gorbachev, T. Georgiou, S.V. Morozov, Strong light-matter interactions in heterostructures of atomically thin films, Science 340 (2013) 1311–1314.

[36] W.J. Yu, Z. Li, H. Zhou, Y.u. Chen, Y. Wang, Y.u. Huang, X. Duan, Vertically stacked multi-heterostructures of layered materials for logic transistors and complementary inverters, Nat. Mater. 12 (3) (2013) 246–252.

[37] R. Moriya, T. Yamaguchi, Y. Inoue, S. Morikawa, Y. Sata, S. Masubuchi, T. Machida, Large current modulation in exfoliated-graphene/MoS_2/metal vertical heterostructures, Appl. Phys. Lett. 105 (8) (2014) 083119, https://doi.org/10.1063/1.4894256.

[38] W.J. Yu, Y. Liu, H. Zhou, A. Yin, Z. Li, Y.u. Huang, X. Duan, Highly efficient gate-tunable photocurrent generation in vertical heterostructures of layered materials, Nat. Nanotechnol. 8 (12) (2013) 952–958.

[39] P.T.K. Loan, W. Zhang, C.-T. Lin, K.-H. Wei, L.-J. Li, C.-H. Chen, Graphene/MoS_2 heterostructures for ultrasensitive detection of DNA hybridisation, Adv. Mater. 26 (28) (2014) 4838–4844.

[40] F. Withers, O. Del Pozo-Zamudio, A. Mishchenko, A.P. Rooney, A. Gholinia, K. Watanabe, T. Taniguchi, S.J. Haigh, A.K. Geim, A.I. Tartakovskii, K. S. Novoselov, Light-emitting diodes by band-structure engineering in van der Waals heterostructures, Nat. Mater. 14 (3) (2015) 301–306.

[41] M.-Y. Li, C.-H. Chen, Y. Shi, L.-J. Li, Heterostructures based on two-dimensional layered materials and their potential applications, Mater. Today 19 (6) (2016) 322–335.

[42] M. Yagmurcukardes, Y. Sozen, M. Baskurt, F.M. Peeters, H. Sahin, Interface-dependent phononic and optical properties of GeO/MoSO heterostructures, Nanoscale 14 (3) (2022) 865–874.

[43] E. Pomerantseva, Y. Gogotsi, Two-dimensional heterostructures for energy storage, Nat. Energy 2 (2017) 1–6.

[44] M. Yagmurcukardes, S. Ozen, F. İyikanat, F.M. Peeters, H. Sahin, Raman fingerprint of stacking order in $HfS_2-Ca(OH)_2$ heterobilayer, Physical Review B 99 (2019), 205405.

[45] X. Sun, C. Zhu, X. Zhu, J. Yi, Y. Liu, D. Li, A. Pan, Recent advances in two-dimensional heterostructures: From band alignment engineering to advanced optoelectronic applications, Adv. Electron. Mater. 7 (2021) 2001174.

[46] M.P. Levendorf, C.-J. Kim, L. Brown, P.Y. Huang, R.W. Havener, D.A. Muller, J. Park, Graphene and boron nitride lateral heterostructures for atomically thin circuitry, Nature 488 (7413) (2012) 627–632.

[47] X. Duan, C. Wang, J.C. Shaw, R. Cheng, Y.u. Chen, H. Li, X. Wu, Y. Tang, Q. Zhang, A. Pan, J. Jiang, R. Yu, Y.u. Huang, X. Duan, Lateral epitaxial growth of two-dimensional layered semiconductor heterojunctions, Nat. Nanotechnol. 9 (12) (2014) 1024–1030.

[48] W. Yang, G. Chen, Z. Shi, C.-C. Liu, L. Zhang, G. Xie, M. Cheng, D. Wang, R. Yang, D. Shi, K. Watanabe, T. Taniguchi, Y. Yao, Y. Zhang, G. Zhang, Epitaxial growth of single-domain graphene on hexagonal boron nitride, Nat. Mater. 12 (9) (2013) 792–797.

[49] Y. Shi, W.u. Zhou, A.-Y. Lu, W. Fang, Y.-H. Lee, A.L. Hsu, S.M. Kim, K.K. Kim, H. Y. Yang, L.-J. Li, J.-C. Idrobo, J. Kong, van der Waals epitaxy of MoS_2 layers using graphene as growth templates, Nano Lett. 12 (6) (2012) 2784–2791.

[50] Y.-C. Lin, N. Lu, N. Perea-Lopez, J. Li, Z. Lin, X. Peng, C.H. Lee, C.e. Sun, L. Calderin, P.N. Browning, M.S. Bresnehan, M.J. Kim, T.S. Mayer, M. Terrones, J. A. Robinson, Direct synthesis of van der Waals solids, ACS Nano 8 (4) (2014) 3715–3723.

[51] Y. Gong, J. Lin, X. Wang, G. Shi, S. Lei, Z. Lin, X. Zou, G. Ye, R. Vajtai, B. I. Yakobson, Vertical and in-plane heterostructures from WS_2/MoS_2 monolayers, Nat. Mater. 13 (2014) 1135–1142.

[52] P.E. Blöchl, Projector augmented-wave method, Physical review B 50 (24) (1994) 17953–17979.

[53] G. Kresse, J. Furthmüller, Efficient iterative schemes for ab initio total-energy calculations using a plane-wave basis set, Physical review B 54 (1996) 11169.

[54] J. Heyd, G.E. Scuseria, M. Ernzerhof, Hybrid functionals based on a screened Coulomb potential, J. Chem. Phys. 118 (2003) 8207–8215.

[55] J.P. Perdew, K. Burke, M. Ernzerhof, Generalized gradient approximation made simple, Phys. Rev. Lett. 77 (1996) 3865.

[56] A. Togo, I. Tanaka, First principles phonon calculations in materials science, Scr. Mater. 108 (2015) 1–5.

[57] A. Bafekry, M. Faraji, D.M. Hoat, M. Fadlallah, M. Shahrokhi, F. Shojaei, D. Gogova, M. Ghergherehchi, $MoSi_2N_4$ single-layer: a novel two-dimensional material with outstanding mechanical, thermal, electronic, optical, and photocatalytic properties, arXiv preprint arXiv:2009.04267, (2020).

[58] L.i. Tan, C. Nie, Z. Ao, H. Sun, T. An, S. Wang, Novel two-dimensional crystalline carbon nitrides beyond gC_3N_4: structure and applications, J. Mater. Chem. A 9 (1) (2021) 17–33.

[59] M. Marques, E. Gross, A primer in density functional theory, Lect. Notes Phys. 620 (2003) 144–184.

[60] R. LeSar, Introduction to computational materials science: fundamentals to applications, Cambridge University Press, 2013.

[61] J. Guan, Z. Zhu, D. Tománek, Phase coexistence and metal-insulator transition in few-layer phosphorene: a computational study, Phys. Rev. Lett. 113 (4) (2014), https://doi.org/10.1103/PhysRevLett.113.046804.

[62] P.-J. Chen, H.-T. Jeng, High applicability of two-dimensional phosphorous in Kagome lattice predicted from first-principles calculations, Sci. Rep. 6 (2016) 1–8.

[63] S. Ahmad, S. Mukherjee, A Comparative Study of Electronic Properties of Bulk MoS_2 and Its Monolayer Using DFT Technique: Application of Mechanical Strain on MoS2 Monolayer, Graphene 03 (04) (2014) 52–59.

[64] F.C. Hagemeister, C.J. Gruenloh, T.S. Zwier, Density functional theory calculations of the structures, binding energies, and infrared spectra of methanol clusters, The Journal of Physical Chemistry A 102 (1) (1998) 82–94.

[65] I. Eren, S. Ozen, Y. Sozen, M. Yagmurcukardes, H. Sahin, Vertical van der Waals heterostructure of single layer InSe and SiGe, The Journal of Physical Chemistry C 123 (51) (2019) 31232–31237.

[66] B. Amin, N. Singh, U. Schwingenschlögl, Heterostructures of transition metal dichalcogenides, Physical review B 92 (2015), 075439.

[67] J. Paier, M. Marsman, G. Kresse, Dielectric properties and excitons for extended systems from hybrid functionals, Physical Review B 78 (2008), 121201.

[68] J.M. Wesselinowa, Hardening and softening of soft phonon modes in ferroelectric thin films, Physical Review B 75 (2007), 045411.

[69] D. Phelan, M. Krogstad, N. Schreiber, R. Osborn, A. Said, H. Zheng, S. Rosenkranz, Acoustic phonon dispersion and diffuse scattering across the valence transition of $(Pr_{0.85}Y_{0.15})0.7Ca_{0.3}CoO_{3-\delta}$, Physical Review B 100 (2019), 054101.

[70] J. Heyd, J.E. Peralta, G.E. Scuseria, R.L. Martin, Energy band gaps and lattice parameters evaluated with the Heyd-Scuseria-Ernzerhof screened hybrid functional, J. Chem. Phys. 123 (2005), 174101.

[71] M. Alam, H.S. Waheed, H. Ullah, M.W. Iqbal, Y.-H. Shin, M.J. Iqbal Khan, H. I. Elsaeedy, R. Neffati, Optoelectronics properties of Janus SnSSe monolayer for solar cells applications, Physica B 625 (2022) 413487, https://doi.org/10.1016/j.physb:2021.413487.

[72] M.W. Iqbal, M. Asghar, N. Noor, H. Ullah, T. Zahid, S. Aftab, A. Mahmood, Analysis of ternary $AlGaX_2$ (X= As, Sb) compounds for opto-electronic and renewable energy devices using density functional theory, Phys. Scr. 96 (2021), 125706.

[73] L.A. Burton, Y.u. Kumagai, A. Walsh, F. Oba, DFT investigation into the underperformance of sulfide materials in photovoltaic applications, J. Mater. Chem. A 5 (19) (2017) 9132–9140.

[74] P. Cheng, T. Wu, J. Zhang, Y. Li, J. Liu, L. Jiang, X. Mao, R.-F. Lu, W.-Q. Deng, K. Han, $(C_6H_5C_2H_4NH_3)_2GeI_4$: a layered two-dimensional perovskite with potential for photovoltaic applications, The journal of physical chemistry letters 8 (18) (2017) 4402–4406.

[75] M. Afsari, A. Boochani, F. Shirdel, Electronic and optical properties of two propounded compound in photovoltaic applications, $CsPbI_3$ and $CH_3NH_3PbI_3$: By DFT, Optik 199 (2019) 163360, https://doi.org/10.1016/j.ijleo.2019.163360.

[76] S. Roy, P. Bermel, Electronic and optical properties of ultra-thin 2D tungsten disulfide for photovoltaic applications, Sol. Energy Mater. Sol. Cells 174 (2018) 370–379.
[77] A. Pashinkin, M. Mikhailova, A. Malkova, V. Fedorov, Heat capacity and thermodynamic properties of lead selenide and lead telluride, Inorg. Mater. 45 (2009) 1226–1229.
[78] D. Parkinson, J. Quarrington, The molar heats of lead sulphide, selenide and telluride in the temperature range 20 K to 260 K, Proc. Phys. Soc. London, Sect. A 67 (1954) 569.

3.4 PAPER III: Strain modulated electro-optical properties of laterally stitched 2D heterostructures

This article is the extension of paper II exclusively focusing on the laterally stitched 2D heterostructures $MoSi_2N_4/XSi_2N_4$ (X=W, Ti). These systems being energetically and dynamically stable with unique electronic features further motivated us to study the tuning of electronic and optical properties. Such heterostructures due to their unique quality of interfaces and their distinctive electrostatics have recently attracted a lot of research interest [94]. The parallel stitched heterostructures of 2D materials are superior to vertical and bulk hetero-systems in that they have larger depletion region, and therefore are more sensitive to charge fluctuation [98, 99], making them perfect for optoelectronic applications [100, 101].

While the $MoSi_2N_4/TiSi_2N_4$ lateral heterostructure (MTLH) exhibits a bandgap of 0.343 eV, the $MoSi_2N_4/WSi_2N_4$-lateral heterostructure (MWLH) reveals a bandgap of 2.35 eV. Further, the impact of biaxial strain on the electronic and optical characteristics of MWLH and MTLH revealed significant changes in their spectra. For instance, the compressive strain in MTLH results in a change from semiconducting to metallic, whereas that in MWLH results in an indirect to direct bandgap transition. Biaxial strain may also be used to successfully modify the spectra of absorbance, transmittance, and reflection. Our research sheds light on the strain engineering of electro-optical properties, opening the door for potential nano- and optoelectronic applications in the future.

Physica E 144 (2022) 115471

Contents lists available at ScienceDirect

Physica E: Low-dimensional Systems and Nanostructures

journal homepage: www.elsevier.com/locate/physe

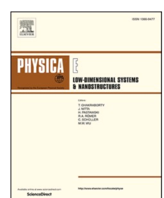

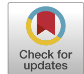

Strain modulated electronic and optical properties of laterally stitched $MoSi_2N_4/XSi_2N_4$ (X=W, Ti) 2D heterostructures

Ghulam Hussain [a,*], Mumtaz Manzoor [b], Muhammad Waqas Iqbal [b], Imran Muhammad [c], Asadollah Bafekry [d,e,**], Hamid Ullah [b,***], Carmine Autieri [a]

[a] International Research Centre MagTop, Institute of Physics, Polish Academy of Sciences, Aleja Lotników 32/46, PL-02668 Warsaw, Poland
[b] Department of Physics, Riphah International University, Campus Lahore, Pakistan
[c] School of Materials Science and Engineering, CAPT, Peking University, Beijing, 100871, China
[d] Department of Physics, University of Guilan, Rasht, 41335-1914, Iran
[e] Department of Physics, Rasht Branch, Islamic Azad University, Rasht, Iran

A B S T R A C T

We used first-principles calculations to investigate the laterally stitched monolayered $MoSi_2N_4/XSi_2N_4$ (X = W, Ti) two-dimensional heterostructures. The structural stability of such heterostructures is confirmed by the phonon spectra exhibiting no imaginary frequencies. From the electronic band structures, the $MoSi_2N_4/WSi_2N_4$-lateral heterostructure (MWLH) shows semiconducting nature with an indirect bandgap of 2.35 eV, while the $MoSi_2N_4/TiSi_2N_4$-lateral heterostructure (MTLH) reveals a bandgap of 0.343 eV. Moreover, the effect of biaxial strain on the electronic and optical properties of MWLH and MTLH is studied, which indicated substantial modifications in their electronic and optical spectra. For instance, the compressive strain in MWLH causes an indirect to direct bandgap transition, while that in MTLH semiconducting to metallic transition. Besides, the absorbance, transmittance and reflectance spectra can effectively be tuned by means of biaxial strain. Our findings provide insights into the strain engineering of electronic and optical features, which could pave the way for future nano- and optoelectronic applications.

1. Introduction

The isolation of freestanding graphene from graphite crystal [1–3], has given rise to tremendous research interest in layered two-dimensional (2D) materials owing to their excellent physical properties and remarkable potential in device applications [4–7]. Owing to the unique optoelectronic properties, high carrier mobility, and on/off ratio, the 2D transition metal dichalcogenides [8–11] and phosphorene [12–15] are widely explored in the last decade. In order to fully exploit these semiconducting layered structures in the nano- and optoelectronics, the tuning of the bandgap is crucial and plays a vital role in the device application. One of the approaches to modulate the bandgap is to apply a tensile or compressive strain to the 2D layered materials [16–20]. This way, one can tune the physical properties of 2D and quasi 2D materials such that strain-sensitive devices could be realized [9, 21–30]F. In 2020, the two 2D layered materials $MoSi_2N_4$ and WSi_2N_4 were experimentally synthesized with chemical vapor deposition (CVD) method [31]. The results demonstrated semiconducting characteristics with outstanding mechanical strength and ambient stability. Also, an intrinsic mobility of 270 $cm^2\ V^{-1}s^{-1}$ for the electrons and of 1200 $cm^2\ V^{-1}s^{-1}$ for the holes were calculated for $MoSi_2N_4$, which is about four times greater than MoS_2 [31,32]. With such remarkable features, $MoSi_2N_4$ and its other group members MA_2Z_4 2D monolayers (where M stands for transition metal Mo, W or Ti, A for Si or Ge and Z represents N, P, or As) are widely studied recently [33–44]. Also, the effect of strain in this class is investigated, highlighting the modification of their electronic and optical properties [43,45–49]. Nevertheless, exploring the biaxial strain in lateral heterostructures (LH) of this class is essential for future applications, which is missing and not reported to date.

In this paper, we study the structural stability, the electronic and optical properties of the $MoSi_2N_4/WSi_2N_4$-lateral heterostructure (MWLH) and $MoSi_2N_4/TiSi_2N_4$-lateral heterostructure (MTLH) using first-principles calculations. Our results illustrate significant modifications in the electronic band structures with the application of mechanical strain, for instance, the MWLH demonstrates a considerable decrease (increase) in the bandgaps when tensile strain (compressive

* Corresponding author.
** Corresponding author. Department of Physics, University of Guilan, Rasht, 41335-1914, Iran.
*** Corresponding author.
E-mail addresses: ghussain@ifpan.edu.pl (G. Hussain), bafekry.asad@gmail.com (A. Bafekry), hamid.ullah@riphah.edu.pk (H. Ullah).

https://doi.org/10.1016/j.physe.2022.115471
Received 27 June 2022; Received in revised form 9 August 2022; Accepted 10 August 2022
Available online 20 August 2022
1386-9477/© 2022 Elsevier B.V. All rights reserved.

strain) is applied, and intriguingly, indirect to direct gap semiconductor transition appears via a compressive strain. Likewise, the bandgap for MTLH increases with tensile strain, and a semiconducting to metallic transition can be achieved via compression. Moreover, the optical properties are substantially modulated through the application of biaxial strain. The tuning of electronic and optical features in the laterally stitched monolayered heterostructures via strain engineering could offer interesting possibilities in nano- and optoelectronics.

2. Methodology

The first-principles calculations were performed via the Vienna ab initio simulation package (VASP) [50,51] using relativistic density functional theory (DFT). The core and the valence electrons were treated within the projector augmented wave (PAW) method [50] with a cutoff of 550 eV for the plane-wave basis. For relaxation, a mesh of $15 \times 15 \times 1$ k-points was chosen. The periodic images of heterostructures were separated by a vacuum layer of ~20 Å in the perpendicular direction to the plane of monolayered LH. This would avoid spurious interactions among the periodic images. Due to the importance of spin-orbit coupling, maximum calculations were performed with the relativistic effects taken into account. We set the convergence criteria to 0.01 eV/Å and energy 10^{-7} per unitcell for our calculations. Also, the dynamical stability of $MoSi_2N_4/WSi_2N_4$-LH and $MoSi_2N_4/TiSi_2N_4$-LH was investigated through PHONOPY code using a $4 \times 4 \times 1$ supercell [52].

The dielectric function is dependent on the thickness of the vacuum when the two-dimensional materials are simulated with sufficiently large distances between the periodic images to avoid the interactions between the 2D layers in DFT calculations [53,54]. This thickness problem is circumvented by characterizing the optical properties of 2D materials using the optical conductivity $\sigma_{2D}(\omega)$. From the Maxwell equation, one can express the 3D optical conductivity as [55]; $\sigma_{3D}(\omega) = i[1 - \varepsilon(\omega)]\varepsilon_o\omega$, here $\varepsilon(\omega)$ represents the complex dielectric function $\varepsilon(\omega) = \varepsilon_1(\omega)+i\varepsilon_2(\omega)$, ε_o denotes the permittivity of vacuum layer, and ω signifies the frequency of the incident photon. The 2D optical conductivity $\sigma_{2D}(\omega)$ is related to $\sigma_{3D}(\omega)$ as [55,56]; $\sigma_{2D}(\omega) = L\sigma_{3D}(\omega)$, where L characterizes the slab thickness. The normalized absorbance $A(\omega)$, transmittance $T(\omega)$ and reflectance $R(\omega)$, do not depend on the polarization of light for a freestanding 2D layer if normal incidence is considered [55,56].

$$A = \frac{Re\,\tilde{\sigma}}{|1+\tilde{\sigma}/2|^2}$$

$$T = \frac{1}{|1+\tilde{\sigma}/2|^2} \quad (1)$$

$$R = \left|\frac{\tilde{\sigma}/2}{1+\tilde{\sigma}/2}\right|^2$$

where $\tilde{\sigma}(\omega) = \sigma_{2D}(\omega)/\varepsilon_o c$ represents the normalized conductivity and c is the speed of light. The above equations are valid for semiconducting 2D materials with the constraint of $T + A + R = 1$.

3. Results and discussions

3.1. Structure and stability

The laterally stitched monolayered heterostructures ($MoSi_2N_4/WSi_2N_4$ and $MoSi_2N_4/TiSi_2N_4$) crystallize in the hexagonal honeycomb structure. Fig. 1(a) depicts the side and top views of these heterostructures exhibiting the stacking of seven atomic layers of N–Si–N-M-N-Si-N, where M = Mo, W and Ti. The strong bonding of these seven layers of atoms gives rise to a sandwich structure, comprising alternative MoN_2 and WN_2 (MoN_2 and TiN_2) layers and two SiN bilayers. We noticed the optimized lattice constants for MWLH and MTLH to be 5.824 and 5.841 Å, respectively. The dynamical stability of MWLH and MTLH is studied through the phonon dispersion calculations as shown in Fig. 1(b), and (c). We employed the finite difference method to calculate the phonon spectra using the Phonopy code [52] with VASP [57] as a calculator. Due to the interface heterostructure, we have a Brillouin zone where the K- and M-points are not all equivalent. We have two inequivalent M-points and two inequivalent K-points like in uniaxially strained graphene [58]. We define these points as M1, M2, K1 and K2. From the phonon band structures along the Brillouin zone's high-symmetry

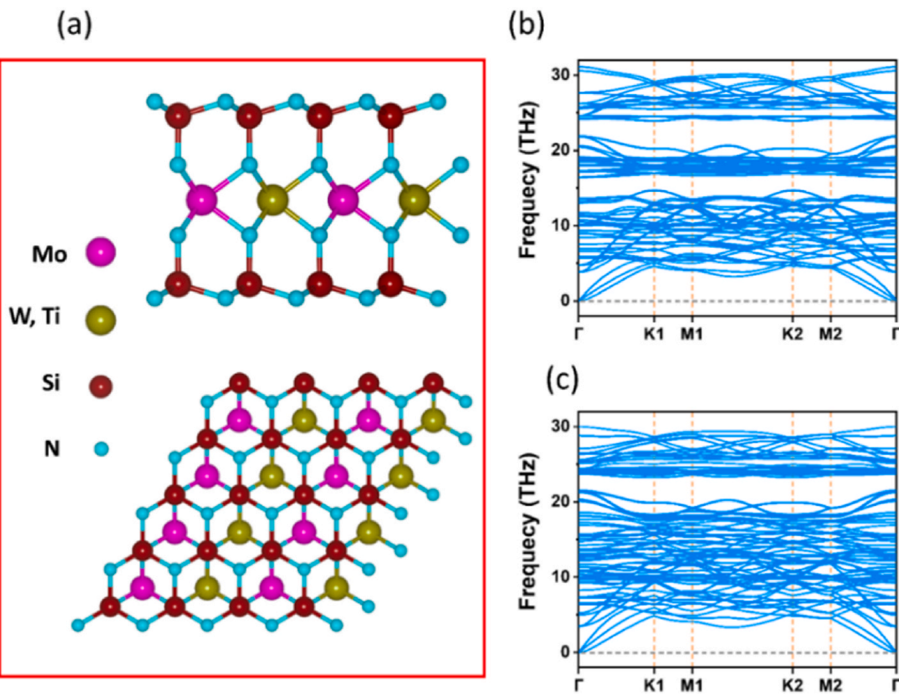

Fig. 1. (a) Side and top views for optimized structure of laterally stitched monolayered heterostructures. (b, c) Phonon spectra of MWLH and MTLH along the path Γ-K1-M1-K2-M2- Γ. The phonon spectra indicate that both MWLH and MTLH are dynamically stable.

directions Γ-K1-M1-K2-M2- Γ shown in Fig. 1(b) and (c), we can see no imaginary frequencies. From similar results along other directions of the **k**-space, it is established that both the MWLH and MTLH systems are dynamically stable due to the absence of imaginary phonon frequencies in the entire hexagonal Brillouin zone.

3.2. Electronic properties

We report the electronic bandstructure of the MWLH and MTLH on the complete k-path including M1, M2, K1 and K2, as illustrated in Fig. 2 (a) and Supplementary Fig. S1. Our results show that the conduction band minimum (CBM) appears at K1 and K2, whereas the valence band maximum (VBM) is at Γ-point, signifying the indirect nature of the bandgap for MWLH. Since we have established that the band structure of the system at M1 and M2 as well as at K1 and K2 is almost equivalent, in the rest of the paper we will focus on the reduced **k**-path that includes just M1 and K1, and that will be renamed as M and K in the rest of the paper. Fig. 2(a) manifests that CBM (at K1/K2) and VBM (at Γ-point) in MWLH are almost equally contributed by Mo and W orbitals. The size of the dot shows the amount of contribution from each atom (Mo states are denoted by purple dots, while W states are shown by green dots), the bigger the size of the dot, the more the orbitals of that atom contribute. Likewise, the band structure for the MTLH on the complete k-path (Γ-K1-M1- Γ-K2-M2) is shown in Fig. S1(a). However, the structure shows metallic behavior, where the conduction and valence bands cross the Fermi-level along Γ-K2 direction. Since the PAW method based on PBE underestimates the electronic bandgap, therefore more accurate method such as HSE06 is used to calculate the bandstructure. In Fig. 2(b), we compare the electronic band structures for MWLH obtained through the generalized gradient approximation with PBE form and Heyd-Scuseria-Ernzerhof (HSE06) denoted by black and blue colors, respectively. The bandgaps are approximated to be 1.92 eV for PBE and 2.35 eV based on HSE06 functionals. Similarly, for MTLH (Fig. S1(b)), the HSE06 corrects the bandstructure, where the valence band maximum is found at M1, while the conduction band minimum appears along Γ-K2 direction presenting the indirect nature of the bandgap.

To investigate qualitatively, the effect of biaxial strain on the electronic properties of the monolayered MWLH, the electronic band structures are computed along the reduced **k**-path K-Γ-M-K, where K═K1 and M = M1 using PBE potential. We accomplished this by applying successive compressive and tensile strains to the monolayered heterostructures ranging from −5 to 5%, respectively. The variation of electronic band structures is studied in detail and the most important results are demonstrated in Fig. 3 for MWLH. Fig. 3(a) illustrates the band structure for strainless MWLH, the valence band maximum (VBM) occurs at 'Γ' point, while the conduction band minimum (CBM) appears at 'K' point of the Brillouin zone suggesting the indirect nature of the bandgap. The red, green and purple dots in the bandstructure plots indicate the position of VBM and CBM. We then apply tensile and compressive strains in the range of −5 to 5%, to inspect their influence on the band structure. As expected, the interatomic distances are greatly modified. The bond lengths of Mo–N ($d_{Mo\text{-}N}$), W–N ($d_{W\text{-}N}$), and also that of Si–N ($d_{Si\text{-}N}$) vary considerably with the biaxial strain (Table 1). These variations in the bond lengths have a substantial impact on the electronic band structures of the strained systems. Upon applying the tensile strain, we noticed that the electronic bandgap significantly decreases from 1.92 eV (unstrained) to 0.95 eV (5% strained) as the value of strain increased. However, it still preserves the nature of the indirect bandgap up to 10%. This evolution in the bandgap is associated with the shifting of the energy states of the conduction band at the K point of the Brillouin zone. From the analysis of the partial density of states (shown in the supplementary materials, Fig. S2(a)), it is evidenced that these states are mainly dominated by the 'd' orbitals of Mo and W. Due to the application of biaxial strain, the bond lengths among the atoms change significantly which causes a different superposition of atomic orbitals, which results in the shift of energy states. A similar trend of variation in the electronic band structure has previously been observed in the layered structure of MoS_2, when the distance between the Si–Mo–S sheets and their number were changed [59]. Fig. 3 (e)–(g) depict the electronic band structures of MWLHs for biaxial compressive strain. Up to −4% compression, we found a monotonic increase in the bandgap, however, beyond that, the bandgap started to decrease (ranging from 2.14 to 2.4 eV). In addition, the indirect bandgap behavior was retained up to −2% compression, nonetheless, the nature of the bandgap changes from indirect to direct at approximately −3% compressive strain. During the transition, we noted that VBM shifts from 'Γ' to the 'K' point in the Brillouin zone. The variation of the bandgap and the transition from indirect to direct bandgap semiconductor is caused due to the shifting of energy states near the VBM and CBM at the high-symmetry **k**-point of the Brillouin zone. To determine the type of orbitals that are involved in causing these variations, the partial density of states (PDOS) for unstrained and strained (−3%) is computed as shown in the supplementary materials Fig. S2(a), and (b), which specify the contribution of orbitals from different atoms. For strainless MWLH, we noted that the energy states near the VBM and CBM originated mainly from the Mo-/W-d orbitals with little contribution N-p orbitals. However, at the transition point (−3%), the N-p orbitals of VBM at the 'K' become dominant with respect to the Mo-/W-d orbitals. Fig. 2(h) shows the overall modulation of the electronic energy bandgap by the biaxial strain. The black, cyan and orange circles represent the strainless, compression and tensile strains' studies, respectively. The main reason behind the strain-induced band structure engineering is the changes in the interatomic distances via lattice expansion or compression, see Table 1. Using the hybrid functionals, we obtain more accurate band structures by correctly approximating the bandgap and band order as compared to the PBE functional. We find that PBE shows metallic behavior for the MTLH structure, where

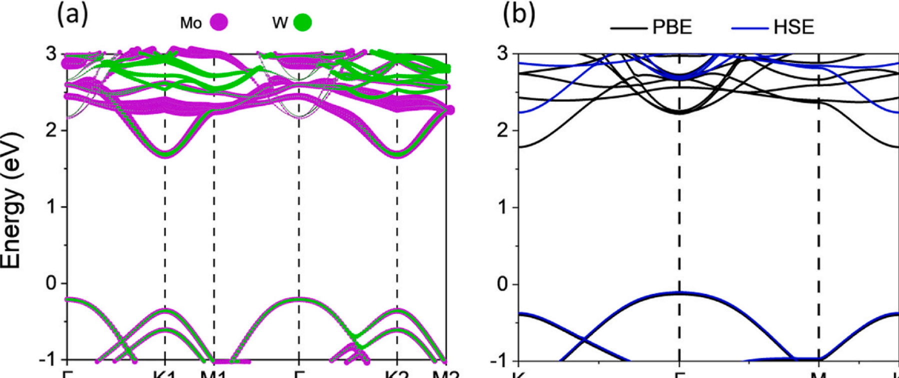

Fig. 2. (a) Projected bandstructure of MWLH along the complete k-path (Γ-K1-M1- Γ-K2-M2), the Mo (purple) and W (green) atoms almost share equal contributions to the VBM and CBM. (b) Electronic bandstructures of MWLH calculated with PBE (black) and HSE06 (blue).

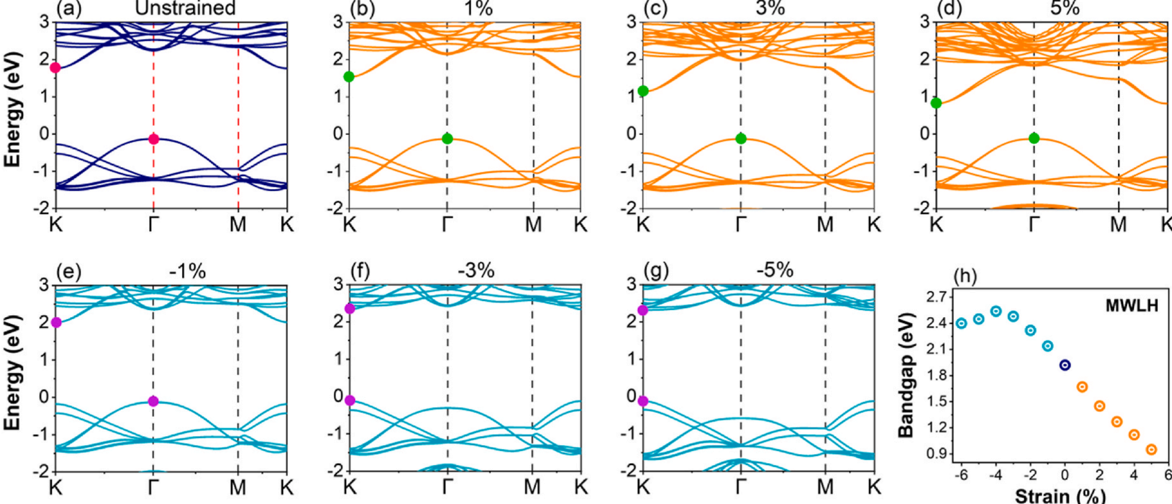

Fig. 3. Electronic band structures of MWLHs along the reduced k-path (K-Γ-M-K), with spin-orbit coupling taken into account. The navy line in (a) demonstrates the bandstructure of unstrained MWLH, while the orange curves in (b), (c) and (d) show the bandstructures for successive tensile biaxial strains. Figures (e)–(g) represent the bandstructures of MWLH against compression. The red, green and purple dots indicate the position of VBM and CBM. (h) The trend of electronic bandgap against the compression and tensile strains, respectively.

Table 1
Calculated interatomic distances of W–N ($\mathbf{d_{W\text{-}N}}$), Mo–N ($\mathbf{d_{Mo\text{-}N}}$), and Si–N ($\mathbf{d_{Si\text{-}N}}$) for lateral heterostructure of $MoSi_2N_4$/WSi_2N_4 as a function of the applied strain.

Tensile strain (%)	$d_{W\text{-}N}$ (Å)	$d_{Mo\text{-}N}$ (Å)	$d_{Si\text{-}N}$ (Å)	Compression (%)	$d_{W\text{-}N}$ (Å)	$d_{Mo\text{-}N}$ (Å)	$d_{Si\text{-}N}$ (Å)
0.00	2.09	2.10	1.76	0.00	2.09	2.10	1.76
1.00	2.10	2.12	1.77	−1.00	2.09	2.09	1.74
2.00	2.11	2.13	1.78	−2.00	2.08	2.08	1.73
3.00	2.12	2.14	1.79	−3.00	2.07	2.07	1.72
4.00	2.13	2.15	1.81	−4.00	2.06	2.06	1.71
5.00	2.14	2.16	1.82	−5.00	2.05	2.05	1.69

the conduction and valence bands cross the Fermi-level along Γ-K2 direction (Fig. S1(a)). On the other hand, the HSE06 corrects the band structure, where the valence band maximum is found at M1, while the conduction band minimum appears along Γ-K2 direction presenting the indirect nature of the bandgap (Fig. S1(b)). Therefore, we apply HSE06 to investigate the effect of biaxial strain on the electronic properties of MTLH, the electronic band structures are computed along the reduced k-path M1-Γ-K2 as shown in Fig. S3. It is noticed that the electronic bandgap for MTLH successively increases with bi-axial tensile strain. Contrary, the bandgap decreases with compression and becomes metallic at −4%.

Since $MoSi_2N_4$ materials are known to host gapped states in a pair of valleys, which are found at the corners of the Brillouin zone [60–62]. Owing to the breaking of inversion symmetry in these monolayers, the spin states become separate in energy resulting in spin-valley couplings near the Fermi level and orbital magnetic moments and valley-contrasting Berry curvatures [63–68]. By performing the band-structure calculations without including spin-orbit coupling (SOC), the states at all the high-symmetry points were observed to be two-fold spin degenerate (as shown in Fig. S4). However, by including SOC, the top of the valence bands at K display spin-splitting of ~125 meV. In contrast, the valence bands occurring at 'M' and 'Γ' points maintain their two-fold spin degeneracy. We noted that the spin states remain separate in energy at 'K', and are not influenced by the biaxial strain indicating the robustness of spin-splitting via SOC. This offers a wide range of potential applications in valleytronics and optoelectronics [59,60,66,68].

3.3. Strain modulated optical properties

2D materials are usually known to sustain lattice strains, providing the possibility to effectively tune their properties via strain engineering. In this section, we report the impact of the biaxial strain on the optical properties of MWLH. The application of tensile or compressive strains on the MWLHs subsequently modulates the optical properties. The dielectric function $\varepsilon(\omega)$ for the heterostructure in the supercell geometry having a vacuum level on both sides is estimated using random phase approximation (RPA) level. Afterward, we converted the $\varepsilon(\omega)$ to in-plane conductivity $\sigma_{2D}(\omega)$, and then employed Eq. (1) to estimate the absorbance, transmittance and reflectance [69]. In Fig. 4(a) and (d), the optical absorbance spectra of MWLH for the respective tensile and compressive strains are demonstrated. For the unstrained case, we noticed almost 0% absorbance up to 1.5 eV, however, beyond that the absorption successively increases. A red-shift (blue-shift) in the absorbance of the heterostructure can be observed with increasing the tensile strain (compressive strain), suggesting the sensitivity and fine-tuning of the optical properties of these structures through biaxial strain. The first peak of the absorbance spectrum occurs at ~2.25 eV for strainless MWLH (specified by the black curve in Fig. 4). This can be related to the direct optical transition at 'K' point of the Brillouin zone (see the band structure plot of Fig. 2(a)) [70]. The first absorption peak appearing at 2.25 eV for unstrained MWLH, is redshifted to 2.16, 2.01, 1.89, 1.77, and 1.68 eV by applying 1%, 2%, 3%, 4%, and 5% tensile strains, respectively. On the contrary, for compressive strains −1%, −2%, −3%, −4%, and −5%, the trend follows a blue-shift with the order, 2.40, 2.55, 2.69, 2.79, and 2.84 eV, respectively. This trend is in agreement with other theoretical studies, where the influence of strain on optical properties is investigated [71,72]. Fig. 4(b, e) presents the transmittance as a function of the biaxial strain for MWLH. The transmittance is almost 100% up to 1.5 eV, which then decreases afterward. The trend of variation in its magnitude as a function of strain is illustrated. In Fig. 4(c), (f), the reflectance spectra as a function of strain are shown, indicating negligible reflectance of the incident light. Furthermore, the effect of the biaxial strain on the optical properties of MTLH is studied. The imaginary part of the dielectric function for MTLH is calculated for different biaxial strains shown in Fig. S5, revealing distinct absorption peaks corresponding to the interband transitions, respectively. Applying biaxial strain to the layered heterostructures is an effective approach to tuning the optoelectronic features of 2D laterally stitched monolayered

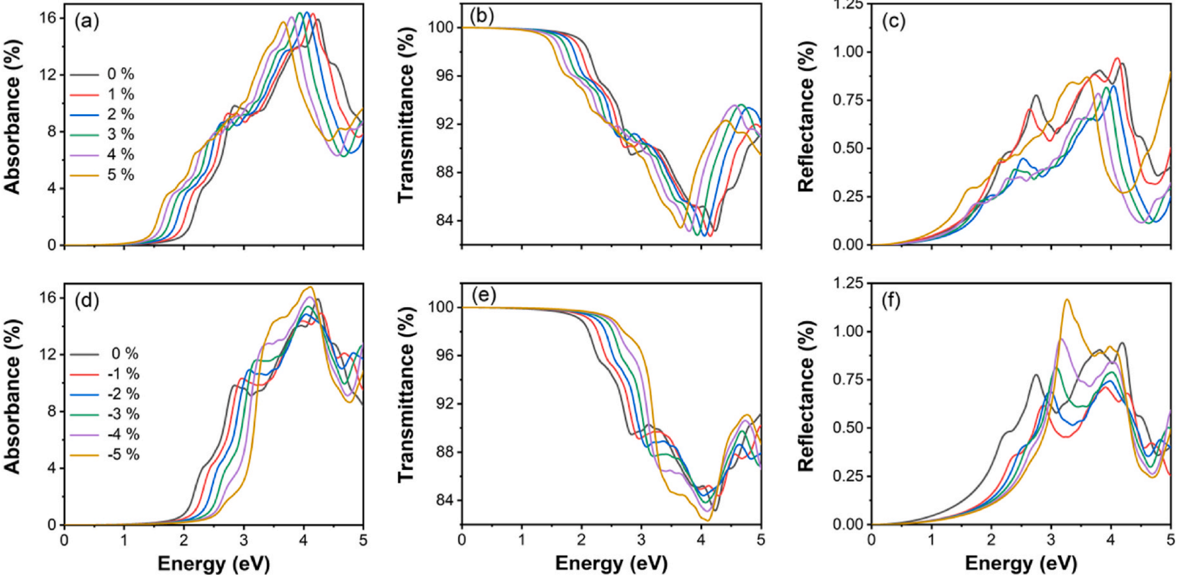

Fig. 4. The optical properties of MWLH as a function of bi-axial strain, the values of strains are shown in the insets of leftmost panel. (a, b, c) present the optical absorbance, transmittance and reflectance for the successive tensile strains, while (d, e, f) show the optical spectra when compressive strain is applied to the heterostructure.

heterostructures. The controlled modification of the optical properties via biaxial strain can offer tremendous applications in optoelectronic devices [73–75].

4. Conclusions

In summary, based on the first-principles calculations, we investigated the structural stability, the strain modulated electronic band structures and optical properties of lateral $MoSi_2N_4/XSi_2N_4$ (X = W, Ti) 2D heterostructures. Our results suggested that the $MoSi_2N_4/WSi_2N_4$ and $MoSi_2N_4/TiSi_2N_4$ lateral heterostructures are dynamically stable. It is concluded that the electronic and optical properties of MWLH and MTLH can effectively be tuned using bi-axial strain engineering. The most significant outcome is that one can easily modulate the electronic band structures of MWLH and MTLH, thereby inducing transitions from indirect to direct bandgap semiconductor, and semiconductor to metallic, respectively. These modifications in the electronic band structures and optical spectra are associated with the changes in the bond lengths because of biaxial strain, principally that of Mo–N ($d_{Mo\text{-}N}$), W–N ($d_{W\text{-}N}$), Ti–N ($d_{Ti\text{-}N}$), and Si–N ($d_{Si\text{-}N}$). The designing of stable lateral heterostructures and the tuning of their electronic and optical attributes via strain engineering could be very promising in optoelectronics devices.

5. Note

The authors declare no competing financial interest.

Declaration of competing interest

The authors declare that they have no known competing financial interests or personal relationships that could have appeared to influence the work reported in this paper.

Data availability

Data will be made available on request.

Acknowledgments

We acknowledge Oleksandr I. Malyi for useful suggestions. This work is supported by the Foundation for Polish Science through the international research agendas program co-financed by the European Union within the smart growth operational program. We acknowledge the access to the computing facilities of the Interdisciplinary Center of Modeling at the University of Warsaw, Grants No. G75-10, No. GB84-0, and No. GB84-7. The authors extend their appreciation to Riphah International University for funding this work under project number R-ORIC-21/FEAS-10.

Appendix A. Supplementary data

Supplementary data to this article can be found online at https://doi.org/10.1016/j.physe.2022.115471.

References

[1] K.S. Novoselov, A.K. Geim, S.V. Morozov, D. Jiang, M.I. Katsnelson, I. Grigorieva, S. Dubonos, A.A. Firsov, Two-dimensional gas of massless Dirac fermions in graphene, Nature 438 (2005) 197–200.
[2] K.S. Novoselov, A.K. Geim, S.V. Morozov, D.-e. Jiang, Y. Zhang, S.V. Dubonos, I. V. Grigorieva, A.A. Firsov, Electric field effect in atomically thin carbon films, Science 306 (2004) 666–669.
[3] K.S. Novoselov, D. Jiang, F. Schedin, T. Booth, V. Khotkevich, S. Morozov, A. K. Geim, Two-dimensional atomic crystals, Proc. Natl. Acad. Sci. USA 102 (2005) 10451–10453.
[4] G.R. Bhimanapati, Z. Lin, V. Meunier, Y. Jung, J. Cha, S. Das, D. Xiao, Y. Son, M. S. Strano, V.R. Cooper, Recent advances in two-dimensional materials beyond graphene, ACS Nano 9 (2015) 11509–11539.
[5] C. Tan, X. Cao, X.-J. Wu, Q. He, J. Yang, X. Zhang, J. Chen, W. Zhao, S. Han, G.-H. Nam, Recent advances in ultrathin two-dimensional nanomaterials, Chem. Rev. 117 (2017) 6225–6331.
[6] C. Tan, Z. Lai, H. Zhang, Ultrathin two-dimensional multinary layered metal chalcogenide nanomaterials, Adv. Mater. 29 (2017), 1701392.
[7] H. Zhang, Ultrathin two-dimensional nanomaterials, ACS Nano 9 (2015) 9451–9469.
[8] A. Splendiani, L. Sun, Y. Zhang, T. Li, J. Kim, C.-Y. Chim, G. Galli, F. Wang, Emerging photoluminescence in monolayer MoS_2, Nano Lett. 10 (2010) 1271–1275.
[9] B. Radisavljevic, A. Radenovic, J. Brivio, V. Giacometti, A. Kis, Single-layer MoS_2 transistors, Nat. Nanotechnol. 6 (2011) 147–150.
[10] K.F. Mak, C. Lee, J. Hone, J. Shan, T.F. Heinz, Atomically thin MoS_2: a new direct-gap semiconductor, Phys. Rev. Lett. 105 (2010), 136805.

[11] S. Aftab, M.W. Iqbal, A.M. Afzal, M.F. Khan, G. Hussain, H.S. Waheed, M. A. Kamran, Formation of an $MoTe_2$ based Schottky junction employing ultra-low and high resistive metal contacts, RSC Adv. 9 (2019) 10017–10023.

[12] H. Liu, A.T. Neal, Z. Zhu, Z. Luo, X. Xu, D. Tománek, P.D. Ye, Phosphorene: an unexplored 2D semiconductor with a high hole mobility, ACS Nano 8 (2014) 4033–4041.

[13] J. Qiao, X. Kong, Z.-X. Hu, F. Yang, W. Ji, High-mobility transport anisotropy and linear dichroism in few-layer black phosphorus, Nat. Commun. 5 (2014) 1–7.

[14] L. Li, Y. Yu, G.J. Ye, Q. Ge, X. Ou, H. Wu, D. Feng, X.H. Chen, Y. Zhang, Black phosphorus field-effect transistors, Nat. Nanotechnol. 9 (2014) 372–377.

[15] S.P. Koenig, R.A. Doganov, H. Schmidt, A. Castro Neto, B. Özyilmaz, Electric field effect in ultrathin black phosphorus, Appl. Phys. Lett. 104 (2014), 103106.

[16] R. Roldán, A. Castellanos-Gomez, E. Cappelluti, F. Guinea, Strain engineering in semiconducting two-dimensional crystals, J. Phys. Condens. Matter 27 (2015), 313201.

[17] Z. Peng, X. Chen, Y. Fan, D.J. Srolovitz, D. Lei, Strain engineering of 2D semiconductors and graphene: from strain fields to band-structure tuning and photonic applications, Light, Science & Applications 9 (2020) 1–25.

[18] E. Scalise, M. Houssa, G. Pourtois, V. Afanas'ev, A. Stesmans, Strain-induced semiconductor to metal transition in the two-dimensional honeycomb structure of MoS_2, Nano Res. 5 (2012) 43–48.

[19] D. Çakır, H. Sahin, F.M. Peeters, Tuning of the electronic and optical properties of single-layer black phosphorus by strain, Phys. Rev. B 90 (2014), 205421.

[20] M.W. Iqbal, K. Shahzad, R. Akbar, G. Hussain, A review on Raman finger prints of doping and strain effect in TMDCs, Microelectron. Eng. 219 (2020), 111152.

[21] R. Fei, L. Yang, Strain-engineering the anisotropic electrical conductance of few-layer black phosphorus, Nano Lett. 14 (2014) 2884–2889.

[22] A. Rodin, A. Carvalho, A.C. Neto, Strain-induced gap modification in black phosphorus, Phys. Rev. Lett. 112 (2014), 176801.

[23] H. Pan, Y.-W. Zhang, Edge-dependent structural, electronic and magnetic properties of MoS 2 nanoribbons, J. Mater. Chem. 22 (2012) 7280–7290.

[24] W.S. Yun, S. Han, S.C. Hong, I.G. Kim, J. Lee, Thickness and strain effects on electronic structures of transition metal dichalcogenides: 2H-MX_2 semiconductors (M= Mo, W; X= S, Se, Te), Phys. Rev. B 85 (2012), 033305.

[25] H. Zhan, D. Guo, G. Xie, Two-dimensional layered materials: from mechanical and coupling properties towards applications in electronics, Nanoscale 11 (2019) 13181–13212.

[26] C. Autieri, G. Cuono, C. Noce, M. Rybak, K.M. Kotur, C.E. Agrapidis, K. Wohlfeld, M. Birowska, Limited ferromagnetic interactions in monolayers of MPS_3 (M= Mn and Ni), J. Phys. Chem. C 126 (2022) 6791–6802.

[27] W. Lei, W. Wang, X. Ming, S. Zhang, G. Tang, X. Zheng, H. Li, C. Autieri, Structural transition, metallization, and superconductivity in quasi-two-dimensional layered PdS_2 under compression, Phys. Rev. B 101 (2020), 205149.

[28] W. Wang, B. Wang, Z. Gao, G. Tang, W. Lei, X. Zheng, H. Li, X. Ming, C. Autieri, Charge density wave instability and pressure-induced superconductivity in bulk 1T−NbS_2, Phys. Rev. B 102 (2020), 155115.

[29] R. Basnet, K. Kotur, M. Rybak, C. Stephenson, S. Bishop, C. Autieri, M. Birowska, J. Hu, Controlling magnetic exchange and anisotropy by non-magnetic ligand substitution in layered MPX_3 (M= Ni, Mn; X= S, Se), Phys. Rev. Research 4 (2022), 023256.

[30] R. Islam, R. Verma, B. Ghosh, Z. Muhammad, A. Bansil, C. Autieri, B. Singh, Switchable Large-Gap Quantum Spin Hall State in Two-Dimensional MSi_2Z_4 Materials Class, 2022 arXiv preprint arXiv:2207.08407.

[31] Y.-L. Hong, Z. Liu, L. Wang, T. Zhou, W. Ma, C. Xu, S. Feng, L. Chen, M.-L. Chen, D.-M. Sun, Chemical vapor deposition of layered two-dimensional $MoSi_2N_4$ materials, Science 369 (2020) 670–674.

[32] Y. Cai, G. Zhang, Y.-W. Zhang, Polarity-reversed robust carrier mobility in monolayer MoS2 nanoribbons, J. Am. Chem. Soc. 136 (2014) 6269–6275.

[33] L. Cao, G. Zhou, Q. Wang, L. Ang, Y.S. Ang, Two-dimensional van der Waals electrical contact to monolayer $MoSi_2N_4$, Appl. Phys. Lett. 118 (2021), 013106.

[34] A. Bafekry, M. Faraji, D. Hoat, M. Shahrokhi, M. Fadlallah, F. Shojaei, S. Feghhi, M. Ghergherehchi, D. Gogova, $MoSi_2N_4$ single-layer: a novel two-dimensional material with outstanding mechanical, thermal, electronic and optical properties, J. Phys. Appl. Phys. 54 (2021), 155303.

[35] B. Mortazavi, B. Javvaji, F. Shojaei, T. Rabczuk, A.V. Shapeev, X. Zhuang, Exceptional piezoelectricity, high thermal conductivity and stiffness and promising photocatalysis in two-dimensional $MoSi_2N_4$ family confirmed by first-principles, Nano Energy 82 (2021), 105716.

[36] C.-c. Jian, X. Ma, J. Zhang, X. Yong, Strained MoSi2N4 monolayers with excellent solar energy absorption and carrier transport properties, J. Phys. Chem. C 125 (2021) 15185–15193.

[37] Q. Wang, L. Cao, S.-J. Liang, W. Wu, G. Wang, C.H. Lee, W.L. Ong, H.Y. Yang, L. K. Ang, S.A. Yang, Efficient Ohmic contacts and built-in atomic sublayer protection in $MoSi_2N_4$ and WSi_2N_4 monolayers, npj 2D Materials and Applications 5 (2021) 1–9.

[38] G. Hussain, A. Samad, M.U. Rehman, G. Cuono, C. Autieri, Emergence of Rashba Splitting and Spin-Valley Properties in Janus $MoGeSiP_2As_2$ and $WGeSiP_2As_2$ Monolayers, 2022 arXiv preprint arXiv:2206.09737.

[39] J. Yu, J. Zhou, X. Wan, Q. Li, High intrinsic lattice thermal conductivity in monolayer $MoSi_2N_4$, New J. Phys. 23 (2021), 033005.

[40] Z. Cui, Y. Luo, J. Yu, Y. Xu, Tuning the electronic properties of $MoSi_2N_4$ by molecular doping: a first principles investigation, Phys. E Low-dimens. Syst. Nanostruct. 134 (2021), 114873.

[41] A. Bafekry, M. Faraji, M.M. Fadlallah, A.B. Khatibani, A. abdolahzadeh Ziabari, M. Ghergherehchi, S. Nedaei, S.F. Shayesteh, D. Gogova, Tunable electronic and magnetic properties of $MoSi_2N_4$ monolayer via vacancy defects, atomic adsorption and atomic doping, Appl. Surf. Sci. 559 (2021), 149862.

[42] H. Yao, C. Zhang, Q. Wang, J. Li, Y. Yu, F. Xu, B. Wang, Y. Wei, Novel two-dimensional layered $MoSi_2Z_4$ (Z= P, as): new promising optoelectronic materials, Nanomaterials 11 (2021) 559.

[43] X. Lv, Y. Xu, B. Mao, G. Liu, G. Zhao, J. Yang, Strain modulation of electronic and optical properties of monolayer $MoSi_2N_4$, Phys. E Low-dimens. Syst. Nanostruct. 135 (2022), 114964.

[44] G. Hussain, M. Asghar, M.W. Iqbal, H. Ullah, C. Autieri, Exploring the structural stability, electronic and thermal attributes of synthetic 2D materials and their heterostructures, Appl. Surf. Sci. 590 (2022), 153131.

[45] H. Zhong, W. Xiong, P. Lv, J. Yu, S. Yuan, Strain-induced semiconductor to metal transition in MA_2Z_4 bilayers (M= Ti, Cr, Mo; A= Si; Z= N, P), Phys. Rev. B 103 (2021), 085124.

[46] Q. Wu, L. Cao, Y.S. Ang, L.K. Ang, Semiconductor-to-metal transition in bilayer MoSi2N4 and WSi_2N_4 with strain and electric field, Appl. Phys. Lett. 118 (2021), 113102.

[47] N. Ghobadi, M. Hosseini, S.B. Touski, Field-Effect Transistor Based on $MoSi_2N_4$ and WSi_2N_4 Monolayers under Biaxial Strain: A Computational Study of the Electronic Properties, IEEE Transactions on Electron Devices, 2022.

[48] X.-S. Guo, S.-D. Guo, Tuning transport coefficients of monolayer MoSi2N4 with biaxial strain, Chin. Phys. B 30 (2021), 067102.

[49] A. Bafekry, C. Stampfl, M. Naseri, M.M. Fadlallah, M. Faraji, M. Ghergherehchi, D. Gogova, S. Feghhi, Effect of electric field and vertical strain on the electro-optical properties of the $MoSi_2N_4$ bilayer: a first-principles calculation, J. Appl. Phys. 129 (2021), 155103.

[50] P.E. Blöchl, Projector augmented-wave method, Phys. Rev. B 50 (1994), 17953.

[51] G. Kresse, J. Furthmüller, Efficient iterative schemes for ab initio total-energy calculations using a plane-wave basis set, Phys. Rev. B 54 (1996), 11169.

[52] A. Togo, I. Tanaka, First principles phonon calculations in materials science, Scripta Mater. 108 (2015) 1–5.

[53] F. Hüser, T. Olsen, K.S. Thygesen, How dielectric screening in two-dimensional crystals affects the convergence of excited-state calculations: monolayer MoS_2, Phys. Rev. B 88 (2013), 245309.

[54] P. Cudazzo, I.V. Tokatly, A. Rubio, Dielectric screening in two-dimensional insulators: implications for excitonic and impurity states in graphane, Phys. Rev. B 84 (2011), 085406.

[55] L. Matthes, O. Pulci, F. Bechstedt, Optical properties of two-dimensional honeycomb crystals graphene, silicene, germanene, and tinene from first principles, New J. Phys. 16 (2014), 105007.

[56] L. Matthes, O. Pulci, F. Bechstedt, Influence of out-of-plane response on optical properties of two-dimensional materials: first principles approach, Phys. Rev. B 94 (2016), 205408.

[57] J. Paier, M. Marsman, G. Kresse, Dielectric properties and excitons for extended systems from hybrid functionals, Phys. Rev. B 78 (2008), 121201.

[58] V.M. Pereira, A.C. Neto, N. Peres, Tight-binding approach to uniaxial strain in graphene, Phys. Rev. B 80 (2009), 045401.

[59] T. Li, G. Galli, Electronic properties of MoS_2 nanoparticles, J. Phys. Chem. C 111 (2007) 16192–16196.

[60] S. Li, W. Wu, X. Feng, S. Guan, W. Feng, Y. Yao, S.A. Yang, Valley-dependent properties of monolayer $MoSi_2N_4$, WSi_2N_4, and $MoSi_2As_4$, Phys. Rev. B 102 (2020), 235435.

[61] H. Ai, D. Liu, J. Geng, S. Wang, K.H. Lo, H. Pan, Theoretical evidence of the spin–valley coupling and valley polarization in two-dimensional $MoSi_2X_4$ (X= N, P, and As), Phys. Chem. Chem. Phys. 23 (2021) 3144–3151.

[62] C. Yang, Z. Song, X. Sun, J. Lu, Valley pseudospin in monolayer $MoSi_2N_4$ and $MoSi_2As_4$, Phys. Rev. B 103 (2021), 035308.

[63] O. Gunawan, Y. Shkolnikov, K. Vakili, T. Gokmen, E. De Poortere, M. Shayegan, Valley susceptibility of an interacting two-dimensional electron system, Phys. Rev. Lett. 97 (2006), 186404.

[64] D. Xiao, W. Yao, Q. Niu, Valley-contrasting physics in graphene: magnetic moment and topological transport, Phys. Rev. Lett. 99 (2007), 236809.

[65] D. Gunlycke, C.T. White, Graphene valley filter using a line defect, Phys. Rev. Lett. 106 (2011), 136806.

[66] D. Xiao, G.-B. Liu, W. Feng, X. Xu, W. Yao, Coupled spin and valley physics in monolayers of MoS_2 and other group-VI dichalcogenides, Phys. Rev. Lett. 108 (2012), 196802.

[67] R. Islam, B. Ghosh, C. Autieri, S. Chowdhury, A. Bansil, A. Agarwal, B. Singh, Tunable spin polarization and electronic structure of bottom-up synthesized $MoSi_2N_4$ materials, Phys. Rev. B 104 (2021) L201112.

[68] C. Autieri, A. Bouhon, B. Sanyal, Gap opening and large spin–orbit splitting in (M= Mo, W; X= S, Se, Te) from the interplay between crystal field and hybridisations: insights from ab-initio theory, Phil. Mag. 97 (2017) 3381–3395.

[69] S. Gupta, S.N. Shirodkar, A. Kutana, B.I. Yakobson, In pursuit of 2D materials for maximum optical response, ACS Nano 12 (2018) 10880–10889.

[70] F. Dybała, M. Polak, J. Kopaczek, P. Scharoch, K. Wu, S. Tongay, R. Kudrawiec, Pressure coefficients for direct optical transitions in MoS_2, $MoSe_2$, WS_2, and WSe_2 crystals and semiconductor to metal transitions, Sci. Rep. 6 (2016) 1–12.

[71] S. Namjoo, P. Puschnig, Optical properties of InAs, InSb and $InAs_xSb_{1-x}$ (x= 0.25, 0.5, 0.75) alloys under strain, Computational Condensed Matter 30 (2022), e00610.

[72] M. Noorafshan, Effect of hydrostatic pressure on electronic structure and optical properties of InAs: a first principle study, Acta Phys. Pol. 137 (2020) 1153–1157.

[73] L.A. Burton, Y. Kumagai, A. Walsh, F. Oba, DFT investigation into the underperformance of sulfide materials in photovoltaic applications, J. Mater. Chem. 5 (2017) 9132–9140.

[74] P. Cheng, T. Wu, J. Zhang, Y. Li, J. Liu, L. Jiang, X. Mao, R.-F. Lu, W.-Q. Deng, K. Han, $(C_6H_5C_2H_4NH_3)_2GeI_4$: a layered two-dimensional perovskite with potential for photovoltaic applications, J. Phys. Chem. Lett. 8 (2017) 4402–4406.

[75] S. Roy, P. Bermel, Electronic and optical properties of ultra-thin 2D tungsten disulfide for photovoltaic applications, Sol. Energy Mater. Sol. Cell. 174 (2018) 370–379.

Supplementary materials

Strain modulated electronic and optical properties of laterally stitched $MoSi_2N_4/XSi_2N_4$ (X=W, Ti) 2D heterostructures

Ghulam Hussain,[a,*] Mumtaz Manzoor,[b] Muhammad Waqas Iqbal,[b] Imran Muhammad,[c] Asadollah Bafekry,[d,*] Hamid Ullah,[b,*] Carmine Autieri[a]

[a]International Research Centre MagTop, Institute of Physics, Polish Academy of Sciences, Aleja Lotników 32/46, PL-02668 Warsaw, Poland

[b]Department of Physics, Riphah International University, Campus Lahore, Pakistan

[c]School of Materials Science and Engineering, CAPT, Peking University, Beijing 100871, China

[d]Department of Physics, University of Antwerp, Groenenborgerlaan 171, B-2020 Antwerp, Belgium

E-mail: ghussain@ifpan.edu.pl, bafekry.asad@gmail.com, hamid.ullah@riphah.edu.pk

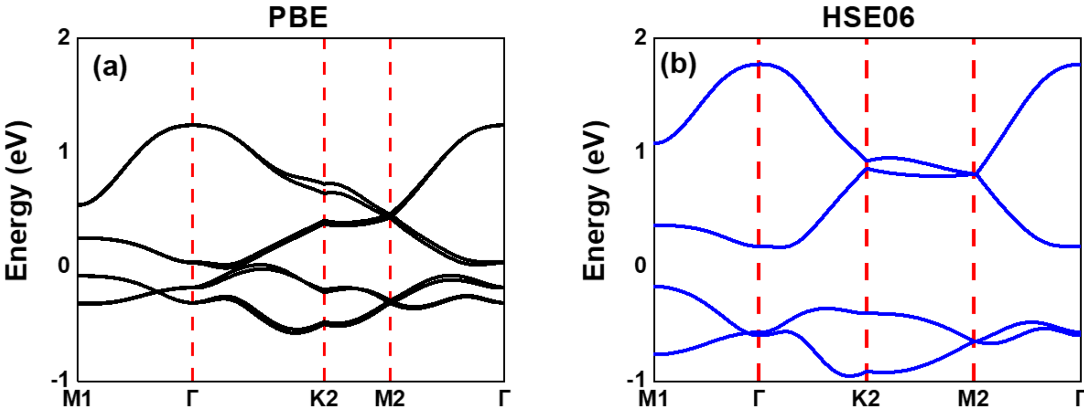

Figure S1 (a) Bandstructure of MTLH along the k-path (M1-Γ-K2-M2-Γ), the VBM and CBM cross the Fermi-level, indicating the metallic behavior. (b) HSE06 based bandstructure for MTLH.

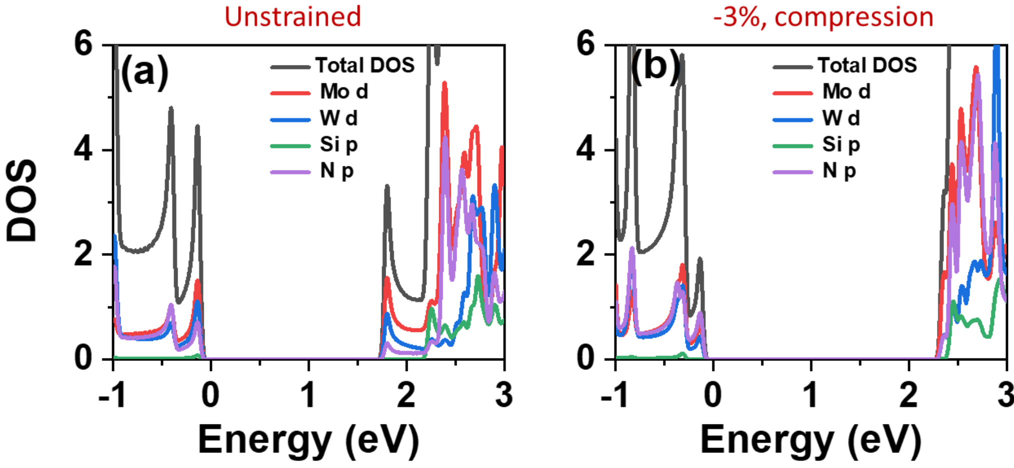

Figure S2 Partial density of states (PDOS), (a) Unstrained MWLH, (b) -3% strained MWLH.

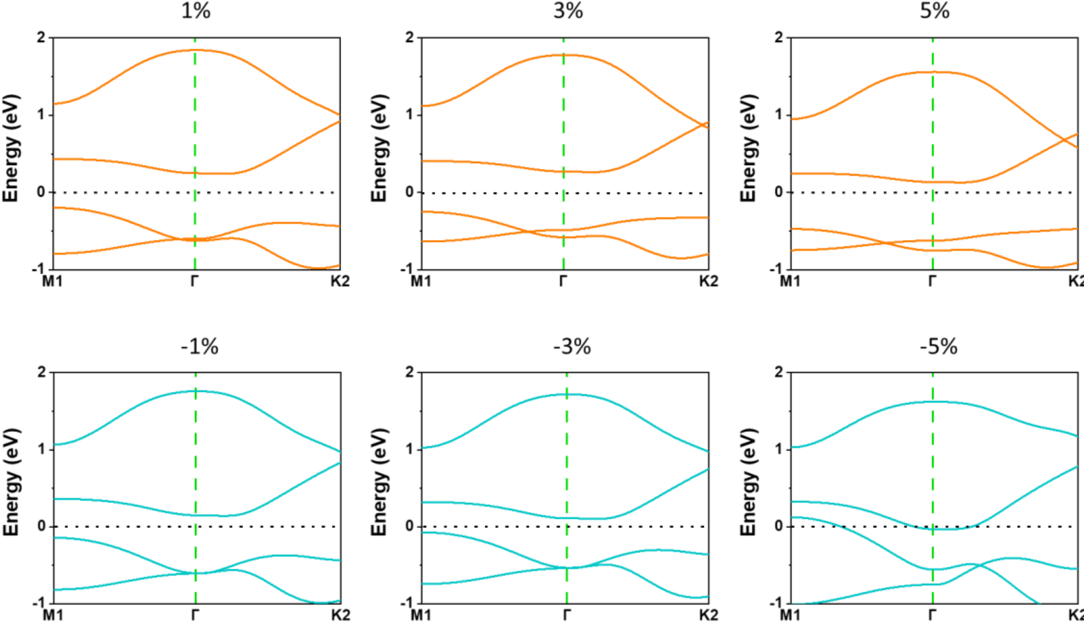

Figure S3 Strain modulated electronic band structures of MTLHs using HSE06. The magnitude of applied strain is indicated for each figure in percent. The black dashed line indicate the position of Fermi level (which is set to zero).

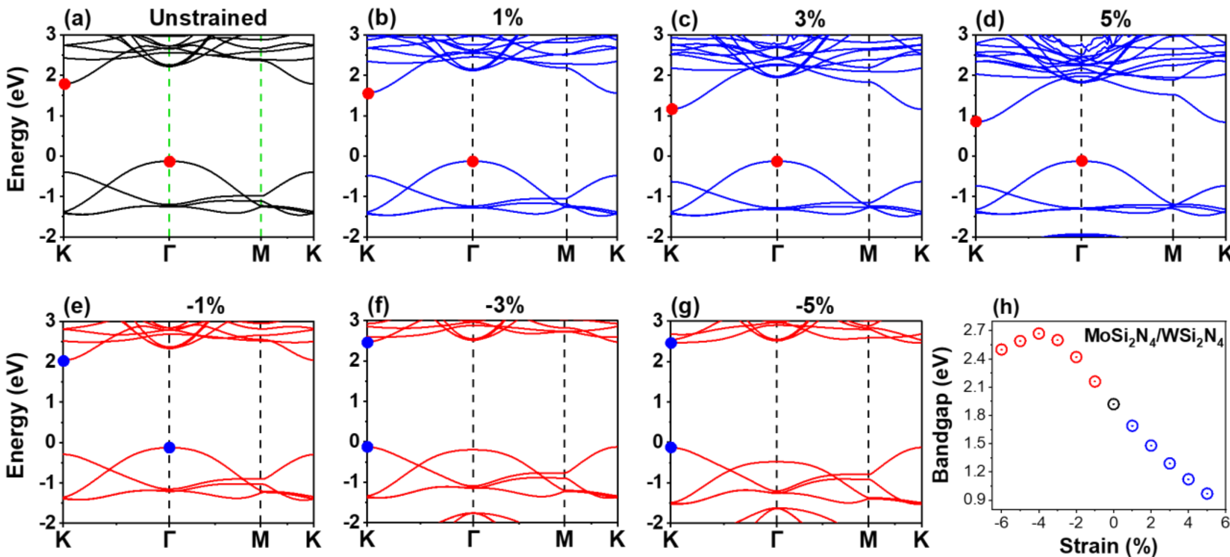

Figure S4 Electronic band structures of MWLHs without SOC. The black in (a) demonstrates the bandstructure of unstrained MWLH, while the blue curves in (b), (c) and (d) show the bandstructures for successive tensile biaxial strains. Figures (e)-(g) represent the bandstructures of MWLH against compression. (h) The trend of electronic bandgap versus biaxial strain.

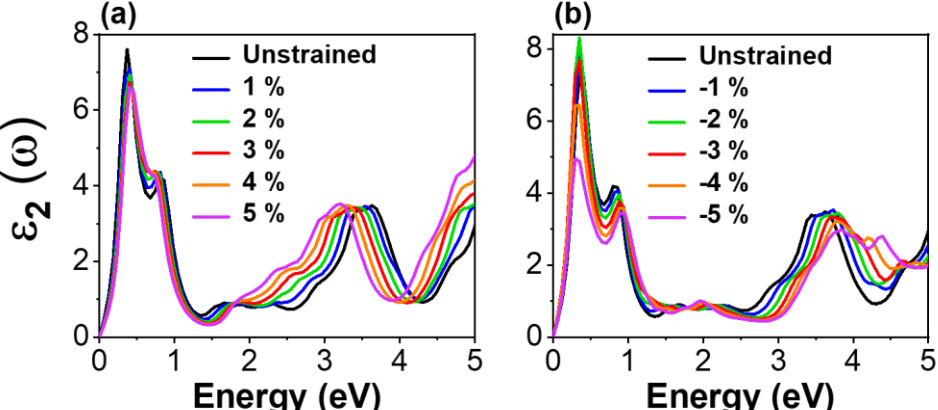

Figure S5 Imaginary part of dielectric function for MTLH as a function of biaxial strain, the peaks in the spectrum correspond to the possible interband transitions from valence to conduction bands.

3.5 PAPER IV: Janus structures

2D transition metal chalcogenides structures have undergone substantial research and found a wide range of uses in electronics and optoelectronics [70, 102-104, 140-144]. The transition metal dichalcogenides (TMDs) bearing the bandgaps ranging from 1.1–1.9 eV with promising mechanical and electronic properties make them suitable to use these systems in photonics and electronic devices [69, 73, 76, 80, 105, 106, 145, 146]. At the corners of the hexagonal Brillouin zone of TMDs, there exist high spin splitting due to the absence of inversion symmetry, and significant spin-orbit coupling (SOC), which is produced by the d-orbitals of transition metals in TMDs [73-75]. Because of the strong correlation between the spin and valley degrees of freedom, the TMDs are regarded as the optimal materials in valleytronics [76, 78, 147]. Additionally, the alloy composition in TMDs, such as in $Mo_xW_{1-x}S_2$, $WS_{2x}Se_{2-2x}$ and MoS_xSe_{2-x}, might be used to modify the electrical and optical characteristics [107-111]. Recently, the chemical vapor deposition (CVD) approach has been used to successfully develop the Janus phase of MoSSe in the 2H phase [112, 113], where the S layer is replaced with Se atoms in the case of MoS_2, while the Se layer with S atoms in $MoSe_2$. With respect to MX_2 (M=Mo, W, and X=S, Se) that preserves the mirror symmetry, the Janus structure i.e. MXY (M=W, Mo, X=Se, S, and Y=S, Se) breaks this symmetry displaying an out-of-plane piezoelectricity and Rashba-type spin splitting due to the perpendicular electric field that results from the breaking of mirror symmetry [72, 114-116, 148].

In this paper, encouraged from the excellent features of MA_2Z_4 materials introduced in paper II and III, we investigate here other members of this family such as pristine $MoSi_2P_4$ and Janus $XGeSiP_2As_2$ (X = Mo, W) monolayers. Using the relativistic density functional theory, the phonon band structures and the orbital-projected electronic band structures are computed thereby to study the dynamical stability and electronic properties. We observed the Zeeman type spin-splitting at K/K' and Rashba-type spin split states at the Γ-point of the Brillouin zone in Janus monolayers. Further exploring these features, we determined the in-plane and out-of-plane spin textures. Due to the breaking of mirror symmetry, we noticed reduced direct bandgaps and large spin-split states in the Janus $XGeSiP_2As_2$ (X = Mo, W) structures along with Rashba splitting, as compared to pristine $MoSi_2P_4$. In the supplementary material, we show and compare the optical spectra for pristine and Janus phases and explain how these materials could be useful in the infrared detectors. The unique electronic, spin and Rashba-type features together with the exceptional optical spectra offer the possibility to employ these systems in the valleytronics, spintronics and optoelectronics.

Journal of Magnetism and Magnetic Materials 563 (2022) 169897

Contents lists available at ScienceDirect

Journal of Magnetism and Magnetic Materials

journal homepage: www.elsevier.com/locate/jmmm

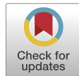

Emergence of Rashba splitting and spin-valley properties in Janus $MoGeSiP_2As_2$ and $WGeSiP_2As_2$ monolayers

Ghulam Hussain [a,*], Abdus Samad [b], Majeed Ur Rehman [c,*], Giuseppe Cuono [a], Carmine Autieri [a]

[a] International Research Centre MagTop, Institute of Physics, Polish Academy of Sciences, Aleja Lotnikow 32/46, PL-02668 Warsaw, Poland
[b] Department of Physics and Energy Harvest Storage Center, University of Ulsan, Ulsan 44610, South Korea
[c] College of Physics and Optoelectronic Engineering, Shenzhen University, Shenzhen, Guangdong 518060, China

ABSTRACT

First-principles calculations are performed to study the structural stability and spintronics properties of Janus $MoGeSiP_2As_2$ and $WGeSiP_2As_2$ monolayers. The high cohesive energies and the stable phonon modes confirm that both these structures are experimentally accessible. In contrast to pristine $MoSi_2P_4$, the Janus monolayers demonstrate reduced direct bandgaps and large spin-split states at K/K'. For the monolayered Janus structure, the broken mirror symmetry with respect to the Mo/W-plane gives rise to a potential gradient normal to the basal plane, which causes difference in the work function for the two surfaces. In addition, the spin textures exposed that breaking the mirror symmetry brings Rashba-type spin splitting in the systems which can be increased by using higher atomic spin–orbit coupling. The large valley spin splitting together with the Rashba splitting in these Janus monolayer structures can make a remarkable contribution to semiconductor valleytronics and spintronics.

1. Introduction

Two-dimensional (2D) structures of transition metal chalcogenides have been the subject of extensive study and have found tremendous applications in electronics and optoelectronics [1–9]. 2D transition metal dichalcogenides TMDCs have electronic bandgaps in the range of 1.1–1.9 eV, and reveal promising electronic and mechanical features, making them applicable in electronic devices and photonics [10–17]. Besides, the lack of inversion symmetry and large spin–orbit coupling (SOC) generated from d-orbitals of transition metals in TMDCs yield enormous spin splitting at the corners of hexagonal Brillouin zone [13,18,19]. The TMDCs are considered ideal materials in valleytronics due to the strong coupling amongst spin and valley degrees of freedom [10,20,21]. Also, the electronic and optical properties could be modulated using the alloy composition in TMDCs, for example in $Mo_xW_{1-x}S_2$, MoS_xSe_{2-x}, and $WS_{2x}Se_{2-2x}$ [22–26]. In recent times, the Janus structure of MoSSe has been successfully grown in the 2H phase via chemical vapor deposition (CVD) method [27,28], thereby replacing the Se layer with S atoms in the case of MoS_2, while the S layer with Se atoms in $MoSe_2$. Different from MX_2 (M = Mo, W and X = S, Se) which possesses mirror symmetry, the Janus phase MXY (M = Mo, W, X = S, Se, and Y = Se, S) shows an out-of-plane electric field owing to the broken mirror symmetry, consequently, the structure exhibits out-of-plane piezoelectricity and Rashba spin splitting [29–33].

Recently discovered 2D materials such as $MoSi_2N_4$ and WSi_2N_4 [34], with outstanding mechanical and semiconducting properties, have stimulated great research interest in studying their other counterparts, MA_2Z_4 (where M stands for transition metal such as Mo and W, A for Si or Ge and Z represents N, P, or As) [35–44]. The studies revealed remarkable electronic, thermal, mechanical, magnetic, and optoelectronic properties [38,44–56]. Furthermore, the breaking of inversion symmetry, together with strong SOC, induces spin-split states, for instance, large spin-splitting has been observed in the valence bands of $MoSi_2N_4$, WSi_2N_4, $MoSi_2As_4$, $CrSi_2P_4$, and $CrSi_2N_4$ at K/K' valleys of the two-dimensional hexagonal Brillouin zone [57–61]. Nonetheless, the Janus phase that is likely to reveal Rashba spin-splitting in this class of materials is essential for spintronic applications.

In the present work, the Janus XGeSiP_2As_2 (X = Mo, W) monolayers are investigated using the relativistic density functional theory. We calculate the phonon spectra and the orbital-projected electronic band structures to study the structural stability and electronic properties of these systems. Together with the band structures, the in-plane and out-of-plane spin textures are obtained to address the spin-split states observed at K/K', and the Rashba-type spin splitting at the Γ-point in Janus monolayers. Contrary to pristine $MoSi_2P_4$, the Janus XGeSiP_2As_2 (X = Mo, W) monolayers demonstrate reduced direct bandgaps, large spin-split states and Rashba splitting, due to the broken mirror symmetry. We found enhanced Rashba splitting as compared to Janus

* Corresponding authors.
E-mail addresses: ghussain@ifpan.edu.pl (G. Hussain), majeed@mail.ustc.edu.cn (M. Ur Rehman).

https://doi.org/10.1016/j.jmmm.2022.169897
Received 20 July 2022; Accepted 29 August 2022
Available online 10 September 2022
0304-8853/© 2022 Elsevier B.V. All rights reserved.

monolayers of transition metal dichalcogenides, *MXY* (where *M* represents Mo or W and $X \neq Y$ denote S, Se, or Te)[30], which could be very promising in spintronics devices, particularly in Datta-Das spin field effect transistors [62].

2. Computational details

First-principles relativistic calculations are carried out on the basis of density functional theory (DFT) using Vienna *Ab Initio* Simulation Package (VASP) [63,64]. The Perdew–Burke–Ernzerhof in the framework of generalized gradient approximation is used to treat electron exchange–correlation [65]. The projector augmented wave method is adopted to resolve the DFT.

Kohn-Sham equations via the plane-wave basis set. An energy cutoff of 350 eV is considered for plane-wave expansion of wave functions and for *k*-point sampling the Monkhorst–Pack scheme is utilized. A dense mesh of 15 × 15 × 1 *k*-point is used. Slab models are built using a vacuum layer of 20 Å in the out-of-plane direction. A force convergence criteria of 0.0001 eV/Å and energy tolerance of 10^{-7} eV are set for the lattice relaxation. 4 × 4 × 1 supercells of the Janus $MoGeSiP_2As_2$ and $WGeSiP_2As_2$ monolayers are considered for the phonon dispersion spectra calculations using the PHONOPY code [66].

3. Results and discussion

The pristine $MoSi_2P_4$ monolayer is observed to crystallize in a hexagonal structure with space group P $\overline{6}$ m2 (No. 187). Monolayer $MoSi_2P_4$ is seven-atom thick, strongly bonded, with atoms stacking order as P-Si-P-Mo-P-Si-P which can be seen as a sandwich of MoP_2 layer between the two Si-P layers (Fig. 1a). This structure preserves the mirror-plane symmetry with respect to Mo atom but breaks the spatial inversion symmetry. Fig. 1b illustrates the projected band structure for pristine monolayer $MoSi_2P_4$ where a direct bandgap of 0.61 eV appears at the K-point between the valence band maximum (VBM) and conduction band minimum (CBM). Due to the broken spatial inversion symmetry, a spin splitting of approximately 137 meV can be seen in the VBM (λ_{Kv}), while in CBM (λ_{Kc}) it is ~ 3.9 meV. Contrary to K-point, the bands at the M- and Γ-points are twofold spin degenerate, see supplementary Fig. S2. From Fig. 1b, it is evident that CBM at K-point is mainly contributed by Mo-dz^2 orbitals, whereas the VBM is composed of Mo-d_{xy} and Mo-d^2_{xy} states. In Fig. 1c, the side and top views of Janus $MoGeSiP_2As_2$ monolayer are presented showing the breaking of mirror symmetry with respect to the Mo plane and the stacking order as As-Si-As-Mo-P-Ge-P. As indicated, the broken symmetry results in unequal interatomic distances, for instance, the bond lengths of Mo-P, Mo-As, Si-As and Ge-P are 2.45, 2.54, 2.32 and 2.30 Å, respectively. Similar variations in the interatomic distances are also observed for $WGeSiP_2As_2$. The optimized lattice constant for $MoGeSiP_2As_2$ monolayer is calculated to be 3.525 Å,

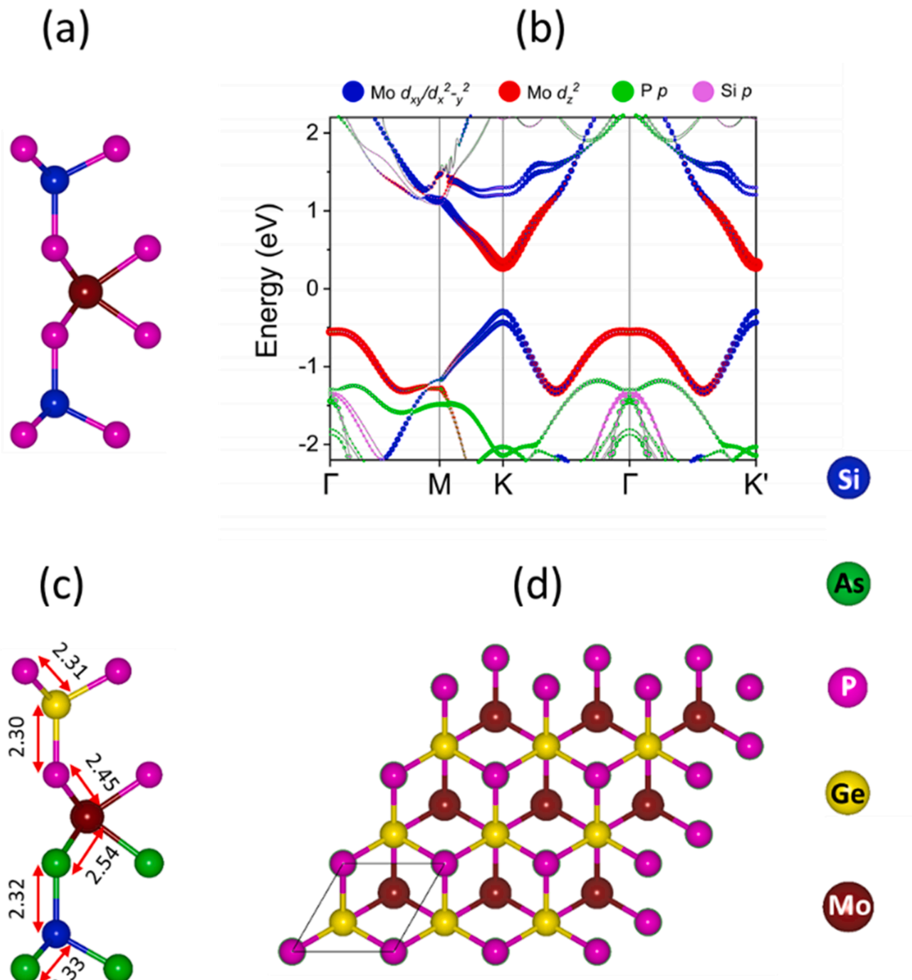

Fig. 1. (a) Side view of $MoSi_2P_4$ monolayer. (b) The projected bandstructure of $MoSi_2P_4$, the different colors represent the contribution of various orbitals to the wave functions at high symmetry k-points. The size of the dot is related to the amount of contribution, the bigger the size of the dot, the more the orbitals contribute. (c, d) Side and top views of Janus $MoGeSiP_2As_2$ monolayer with bond lengths shown in Å.

while that of $WGeSiP_2As_2$ is 3.564 Å.

To study the stability of these Janus structures, we calculated the cohesive energies and performed the phonon calculations using 4 × 4 × 1 supercell. The cohesive energy (E_c) for $MoGeSiP_2As_2$, is calculated from the $E_c = E_{MoGeSiP2As2} - (E_{Mo} + E_{Ge} + E_{Si} + E_P + E_{As})$, where $E_{MoGeSiP2As2}$, and the energy terms in parenthesis (E_{Mo}, E_{Ge}, E_{Si}, E_P and E_{As}) designate the total energy of monolayer $MoGeSiP_2As_2$ and that of individual atoms. It is computed to be −2.77 eV/atom for $MoGeSiP_2As_2$, and −2.84 eV/atom in the case of $WGeSiP_2As_2$, which are higher than the previously reported Janus structures of MoSSe (−2.34 eV) and WSSe (-2.06 eV) [31]. These values are large enough to promise the stability of Janus structures in this class of 2D materials. Moreover, the phonon spectra are useful to investigate the dynamical stability of materials. We calculated the phonon band structures for $MoGeSiP_2As_2$ and $WGeSiP_2As_2$ along the Brillouin zone's high symmetry directions (K-Γ-M−K) using the finite difference method that is implemented in Phonopy code (Fig. 2a and 2c). The phonon spectra of both the $MoGeSiP_2As_2$ and $WGeSiP_2As_2$ reveal no negative frequency modes, indicating the dynamical stability of these Janus monolayers. On the other hand, the phonon band structures of $MoSnSiP_2As_2$ and $MoPbSiP_2As_2$ (shown in supplementary Fig. S1) exhibit the negative frequency phonon modes along the high-symmetry directions in their first Brillouin zone, hence they are dynamically unstable. From this, we infer that the Janus structures of $MoGeSiP_2As_2$ and $WGeSiP_2As_2$ can be experimentally accessible. As the work function Φ of a material strongly changes with the conditions on the surface. For that reason, it is essential to see the impact of Janus phase on the work function Φ, since for Janus structure, the broken mirror symmetry with respect to the transition element (Mo/W) gives rise to a potential gradient normal to the basal plane. We illustrate the planar average of the electrostatic potential energy in Fig. 2b, d where the energy difference ΔΦ represents the work function difference [67]. For $MoGeSiP_2As_2$, the ΔΦ is calculated to be ~ 0.4 eV, while that of $WGeSiP_2As_2$, it is ~ 0.45 eV.

To understand the electronic properties, we calculated the orbital-projected electronic band structures for both the $MoGeSiP_2As_2$, and $WGeSiP_2As_2$ at PBE level considering the SOC, as presented in Fig. 3a, b. For $MoGeSiP_2As_2$, the VBM and CBM appear at the K-point of the Brillouin zone, indicating that the Janus phase retains the direct bandgap, however, with a slight decrease in the bandgap value (0.57 eV) with respect to pristine $MoSi_2P_4$ monolayer. It is depicted that the CBM is principally composed of Mo-d_z^2 orbitals whereas the VBM is composed of Mo-d_{xy} and Mo-d_{xy}^2 states. Besides, the Zeeman-type spin splitting in the valence band, λ_{Kv} is enhanced to 161.7 meV, while that of λ_{Kc} to 10.6 meV as compared to the pristine $MoSi_2P_4$. For $WGeSiP_2As_2$, which essentially bears the same physics as $MoGeSiP_2As_2$, and attains the similar trigonal C_{3v} symmetry in Janus form. The orbital-projected bandstructure for $WGeSiP_2As_2$ monolayer is demonstrated in Fig. 3b; the electronic bandgap is significantly reduced (0.25 eV) with respect to pristine $MoSi_2P_4$ and Janus $MoGeSiP_2As_2$, while preserving the direct nature of its bandgap. In addition, the spin splitting λ_{Kv} and λ_{Kc} are enhanced in $WGeSiP_2As_2$ to 472 and 20.6 meV, respectively. From the orbital contributions in the bandstructure, it is shown that CBM is maximally composed of W-d_z^2 orbitals, where the VBM is contributed by W-d_{xy} and W-d_{xy}^2 states. Table 1 lists the values for the electronic band gap E_g, and that of bands splitting λ_{Kv}, λ_{Kc}.

To explore the spintronics features for the two Janus structures ($MoGeSiP_2As_2$ and $WGeSiP_2As_2$), the spin textures for the two spin-splitted valence bands (at K/K' points) are computed for the entire

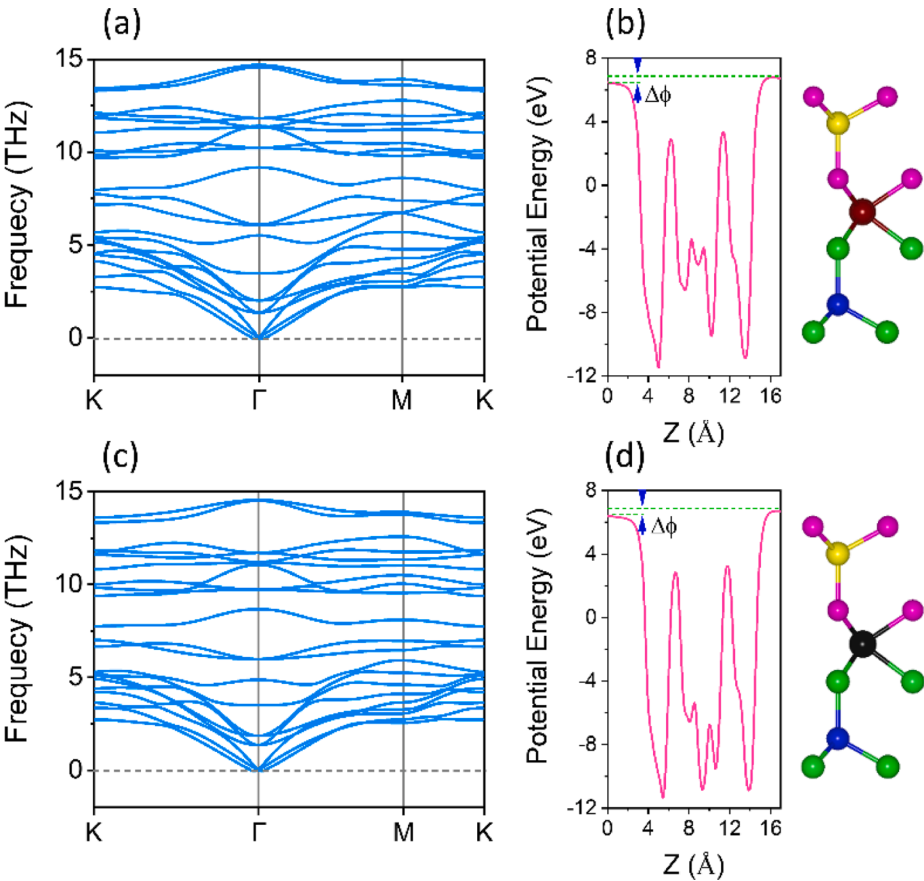

Fig. 2. Phonon spectra of Janus (a) $MoGeSiP_2As_2$, and (c) $WGeSiP_2As_2$ monolayers. Both the structures demonstrate positive phonon modes with no imaginary frequencies, confirming their dynamical stability. The planar average electrostatic potential energy of (b) $MoGeSiP_2As_2$, (d) $WGeSiP_2As_2$ monolayers, the work function difference, ΔΦ is estimated to be 0.4 and 0.45 eV, respectively.

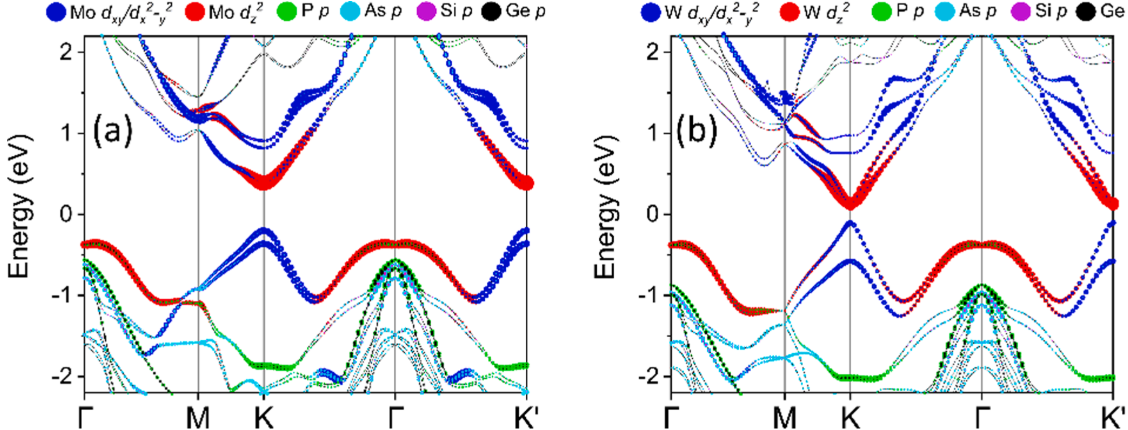

Fig. 3. Orbital-projected bandstructures of Janus systems, (a) $MoGeSiP_2As_2$, (b) $WGeSiP_2As_2$. The contribution of orbitals to the wave functions at high symmetry k-points is proportional to size of the colored dot i.e. the larger the dot size, the more they contribute.

Table 1
Electronic bandgap E_g, the valence band splitting λ_{Kv} at K-point, conduction band splitting λ_{Kc} at K-point, and the Rashba parameter α_R (eVÅ).

Material	E_g (eV)	λ_{Kv} (meV)	λ_{Kc} (meV)	α_R (eVÅ)
$MoSi_2P_4$	0.61	137	3.90	0.00
$MoGeSiP_2As_2$	0.57	162	10.6	0.50
$WGeSiP_2As_2$	0.25	472	20.6	0.52

Brillouin zone as demonstrated in Fig. 4. The arrows illustrate the in-plane components of spin polarization, while the colors display the out-of-plane component of spin polarization. Because of the time-reversal symmetry, these systems are overall nonmagnetic, since opposite out-of-plane components of spin polarization can be clearly seen at the time-reversal high symmetry K and − K points. We found clockwise rotation for the in-plane spin components of the upper valence band (upper panel), while counterclockwise for the lower valence band (lower panel). Due to the time-reversal symmetry, the spin splitting would likely be opposite at the two time-reversed high symmetry points of the Brillouin zone, and thus demonstrate opposite in-plane spin patterns at K/K' point. Interestingly, while the spin texture shows opposite polarizations for the two splitted bands, the same chirality is observed at K/K' points for the in-plane spin components in a single valence band.

Notably, the twofold spin degeneracy is lifted at the Γ-point for both the Janus monolayers, where the valence bands split not only in energy but also in momentum, giving rise to Rashba spin splitting (Fig. 5a, c). The Rashba energy E_R, the momentum offset K_R, and the Rashba parameter α_R are obtained at PBE + SOC level, where E_R is the energy

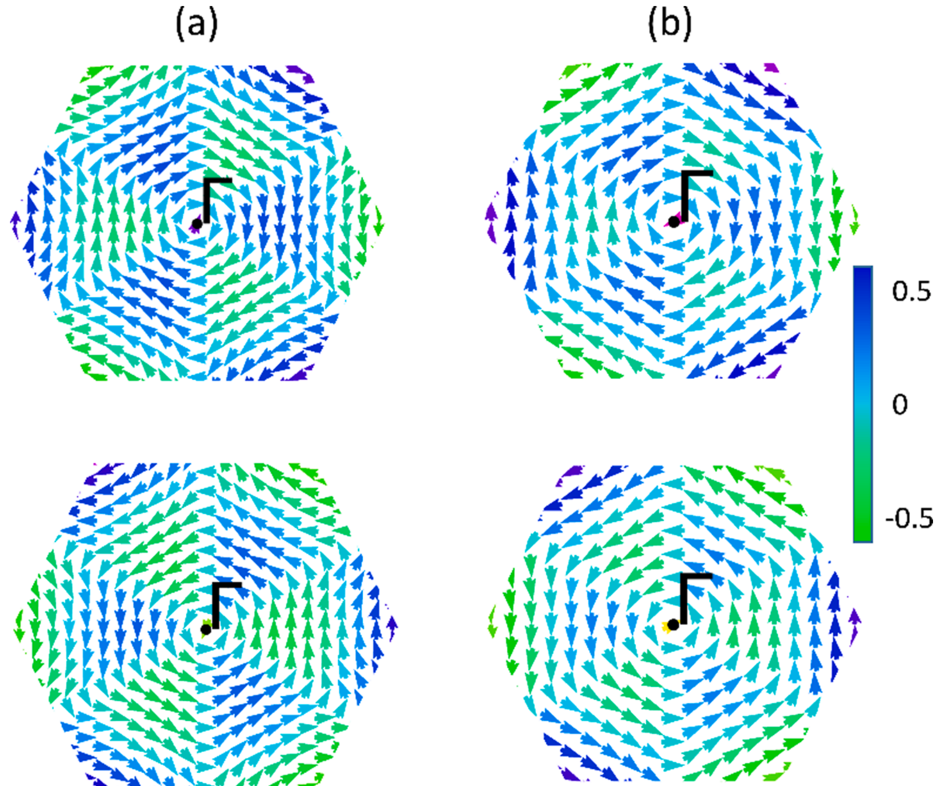

Fig. 4. Spin textures for the upper and lower spin-splitted valence bands calculated for the complete BZ, (a) $MoGeSiP_2As_2$, (b) $WGeSiP_2As_2$. The arrows represent the in-plane components of spin polarization, while the colors designate the out-of-plane component of spin polarization.

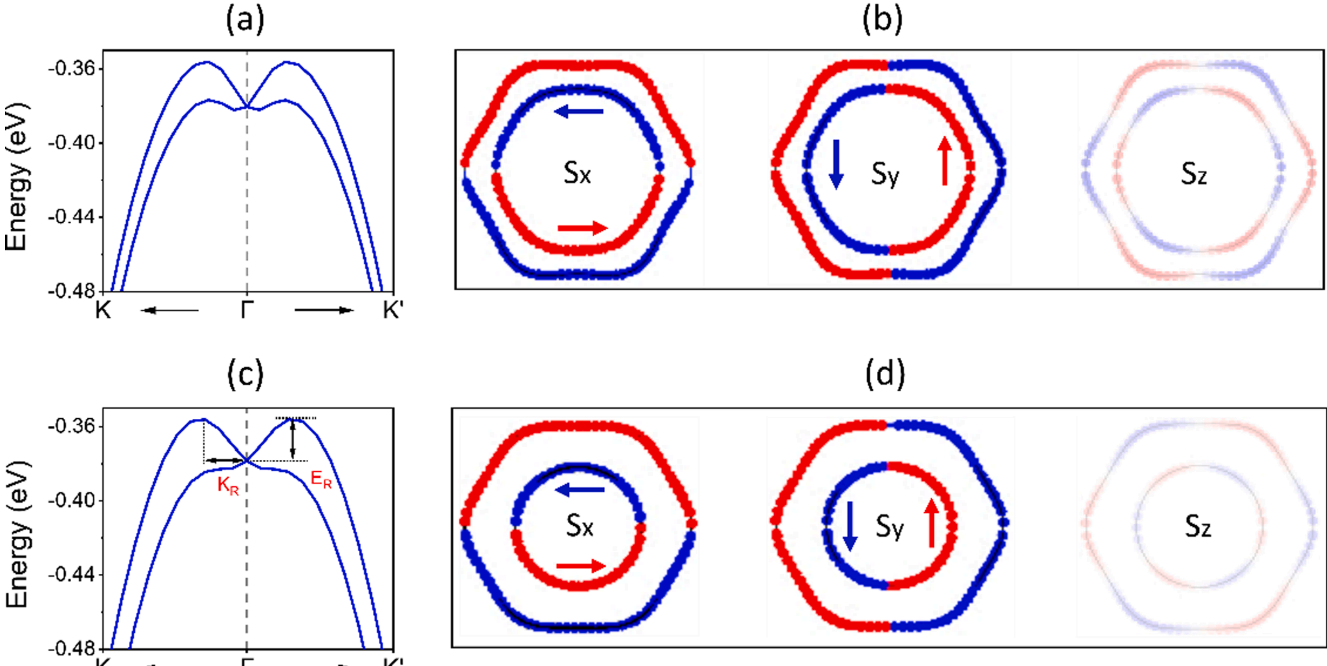

Fig. 5. Zoomed illustrations of the valence bands aroung Γ-point for the Janus phases, (a) $MoGeSiP_2As_2$, (c) $WGeSiP_2As_2$ to investigate the Rashba-type spin splitting. Spin-resolved constant energy 2D contours exhibiting the Rashba-type splitting for the spin projections i.e. Sx, Sy, and Sz, respectively. (b) $MoGeSiP_2As_2$, (d) $WGeSiP_2As_2$.

change of split states, K_R characterizes the shift of bands in momentum space at Γ-point (as indicated in Fig. 5c), and α_R can be expressed as, $\alpha_R = 2E_R/K_R$. At Γ-point, the valence bands are mainly contributed by Mo/W-d_z^2 orbitals and are slightly composed of P-*p* and Ge-*p* orbitals as evidenced in Fig. 3, defining the Rashba spin splitting in $MoGeSiP_2As_2$ and $WGeSiP_2As_2$ monolayers. The symmetry of $MoGeSiP_2As_2$ and $WGeSiP_2As_2$ become trigonal C_{3v}, which is different from that of $MoSi_2P_4$ with space group D_{3h} due to the out-of-plane asymmetry I ($I \neq Z \rightarrow -Z$). We noticed the Rashba spin splitting α_R is slightly larger in magnitude for $WGeSiP_2As_2$ (0.52 eVÅ) as compared to $MoGeSiP_2As_2$ (∼0.50 eVÅ). All the calculated parameters such as electronic band gap E_g, λ_{Kv}, λ_{Kc}, and α_R are summarized in Table 1. Fig. 5b, d illustrate the constant energy spin-resolved 2D contours for the spin texture centered at the Γ-point; the S_x, S_y and S_z components are calculated in the $k_x - k_y$ plane for $MoGeSiP_2As_2$ and $WGeSiP_2As_2$, respectively. The Rashba-type splitting of spin-up and spin-down states is distinctly manifested by red and blue curves, respectively. The 2D Rashba spin splitting for the two valence bands (spin-up and spin-down) produces spin-textures with clockwise and anti-clockwise spin directions. This trend can be observed almost perfectly for the in-plane S_x and S_y spin components with inner and outer branches of Rashba-type split valence bands. However, the feature is weakly accompanied by the out-of-plane S_z component, as observed in WSSe [30] and BiTeCl [68].

We determined that trigonal C_{3v} symmetry brings a net dipole moment [69]. in $WGeSiP_2As_2$ and $MoGeSiP_2As_2$ monolayers, which play a crucial role in the Zeeman-type bands splitting. The arrows in the spin textures characterize the in-plane components of spin polarization and the colors show the out-of-plane component of spin polarization. Because of the time-reversal symmetry, these systems are overall nonmagnetic, since the opposite out-of-plane components of spin polarization can be clearly seen at time-reversed K and − K points [69]. Around the Γ point, we observe a sequence of 6 regions where S_z becomes alternatively positive and negative. This is a signature of a strong cubic spin splitting [70–72], which is complementary to purely cubic Rashba and Dresselhaus types. This effect is particularly strong in Fig. 3c and it becomes weaker for the $WSiP_2As_2$. Moreover, the broken mirror symmetry assures to assist the Rashba-type spin splitting in these Janus systems. From Table 1, it is established that $WGeSiP_2As_2$ shows relatively larger band splitting (λ_{Kv}, λ_{Kc}) and the Rashba parameters due to the heavy nature of the W atom.

4. Conclusions

In summary, we presented a detailed and systematic study on Janus XGeSiP_2As_2 (X = Mo, W) monolayers obtained via first-principles methods. The cohesive energies and phonon dispersion calculations demonstrated that these structures are stable. In electronic band structures, the intrinsic spin splitting at the K/K'-points of pristine $MoSi_2P_4$ is further enhanced in the Janus phase, suggesting their valleytronic applications. Moreover, the broken mirror symmetry in XGeSiP_2As_2 induces an out-of-plane electric field that results in Rashba-type spin splitting at the Γ-point. This splitting occurs due to the asymmetric potential in the Janus phase, perpendicular to the basal plane. Additionally, a signature of strong cubic spin splitting has been observed for the $MoGeSiP_2As_2$. Our study unveils the potential of Janus $XGeSiP_2As_2$ monolayers for valleytronics and spintronics.

Declaration of Competing Interest

The authors declare that they have no known competing financial interests or personal relationships that could have appeared to influence the work reported in this paper.

Data availability

Data will be made available on request.

Acknowledgements

This work is supported by the Foundation for Polish Science through the international research agendas program co-financed by the European Union within the smart growth operational program. We

acknowledge the access to the computing facilities of the Interdisciplinary Center of Modeling at the University of Warsaw, Grants No. G75-10, No. GB84-0, and No. GB84-7.

Appendix A. Supplementary material

Supplementary data to this article can be found online at https://doi.org/10.1016/j.jmmm.2022.169897.

References

[1] M. Chhowalla, H.S. Shin, G. Eda, L.-J. Li, K.P. Loh, H. Zhang, The chemistry of two-dimensional layered transition metal dichalcogenide nanosheets, Nat. Chem. 5 (2013) 263–275.

[2] K.F. Mak, C. Lee, J. Hone, J. Shan, T.F. Heinz, Atomically thin MoS_2: a new direct-gap semiconductor, Phys. Rev. Lett. 105 (2010), 136805.

[3] X. Xu, W. Yao, D. Xiao, T.F. Heinz, Spin and pseudospins in layered transition metal dichalcogenides, Nat. Phys. 10 (2014) 343–350.

[4] B. Radisavljevic, A. Radenovic, J. Brivio, V. Giacometti, A. Kis, Single-layer MoS_2 transistors, Nat. Nanotechnol. 6 (2011) 147–150.

[5] S. Manzeli, D. Ovchinnikov, D. Pasquier, O.V. Yazyev, A. Kis, 2D transition metal dichalcogenides, Nat. Rev. Mater. 2 (2017) 1–15.

[6] C. Autieri, G. Cuono, C. Noce, M. Rybak, K.M. Kotur, C.E. Agrapidis, K. Wohlfeld, M. Birowska, Limited Ferromagnetic Interactions in Monolayers of MPS_3 M= Mn and Ni, J. Phys. Chem. C 126 (2022) 6791–6802.

[7] R. Basnet, K. Kotur, M. Rybak, C. Stephenson, S. Bishop, C. Autieri, M. Birowska, J. Hu, Controlling magnetic exchange and anisotropy by non-magnetic ligand substitution in layered MPX_3 (M= Ni, Mn; X= S, Se), arXiv preprint arXiv: 2205.04585, (2022).

[8] W. Lei, W. Wang, X. Ming, S. Zhang, G. Tang, X. Zheng, H. Li, C. Autieri, Structural transition, metallization, and superconductivity in quasi-two-dimensional layered PdS_2 under compression, Phys. Rev. B 101 (2020), 205149.

[9] W. Wang, B. Wang, Z. Gao, G. Tang, W. Lei, X. Zheng, H. Li, X. Ming, C. Autieri, Charge density wave instability and pressure-induced superconductivity in bulk 1T-NbS_2, Phys. Rev. B 102 (2020), 155115.

[10] H. Zeng, J. Dai, W. Yao, D. Xiao, X. Cui, Valley polarization in MoS_2 monolayers by optical pumping, Nat. Nanotechnol. 7 (2012) 490–493.

[11] Q.H. Wang, K. Kalantar-Zadeh, A. Kis, J.N. Coleman, M.S. Strano, Electronics and optoelectronics of two-dimensional transition metal dichalcogenides, Nat. Nanotechnol. 7 (2012) 699–712.

[12] K.F. Mak, J. Shan, Photonics and optoelectronics of 2D semiconductor transition metal dichalcogenides, Nat. Photon. 10 (2016) 216–226.

[13] A. Kuc, T. Heine, The electronic structure calculations of two-dimensional transition-metal dichalcogenides in the presence of external electric and magnetic fields, Chem. Soc. Rev. 44 (2015) 2603–2614.

[14] M.W. Iqbal, M.Z. Iqbal, M.F. Khan, M.A. Shehzad, Y. Seo, J.H. Park, C. Hwang, J. Eom, High-mobility and air-stable single-layer WS_2 field-effect transistors sandwiched between chemical vapor deposition-grown hexagonal BN films, Sci. Rep. 5 (2015) 1–9.

[15] T.B. Wendumu, G. Seifert, T. Lorenz, J.-O. Joswig, A. Enyashin, Optical properties of triangular molybdenum disulfide nanoflakes, J. Phys. Chem. Lett. 5 (2014) 3636–3640.

[16] Z. Ye, T. Cao, K. O'brien, H. Zhu, X. Yin, Y. Wang, S.G. Louie, X. Zhang, Probing excitonic dark states in single-layer tungsten disulphide, Nature, 513 (2014) 214–218.

[17] C. Autieri, A. Bouhon, B. Sanyal, Gap opening and large spin–orbit splitting in (M= Mo, W; X= S, Se, Te) from the interplay between crystal field and hybridisations: insights from ab-initio theory, Phil. Mag. 97 (2017) 3381–3395.

[18] N. Zibouche, A. Kuc, J. Musfeldt, T. Heine, Transition-metal dichalcogenides for spintronic applications, Ann. Phys. 526 (2014) 395–401.

[19] Z.Y. Zhu, Y.C. Cheng, U. Schwingenschlögl, Giant spin-orbit-induced spin splitting in two-dimensional transition-metal dichalcogenide semiconductors, Phys. Rev. B 84 (2011), 153402.

[20] K.F. Mak, K. He, J. Shan, T.F. Heinz, Control of valley polarization in monolayer MoS_2 by optical helicity, Nat. Nanotechnol. 7 (2012) 494–498.

[21] D. Xiao, G.-B. Liu, W. Feng, X. Xu, W. Yao, Coupled spin and valley physics in monolayers of MoS 2 and other group-VI dichalcogenides, Phys. Rev. Lett. 108 (2012), 196802.

[22] J. Xi, T. Zhao, D. Wang, Z. Shuai, Tunable electronic properties of two-dimensional transition metal dichalcogenide alloys: a first-principles prediction, J. Phys. Chem. Lett. 5 (2014) 285–291.

[23] X. Duan, C. Wang, Z. Fan, G. Hao, L. Kou, U. Halim, H. Li, X. Wu, Y. Wang, J. Jiang, Synthesis of $WS_{2x}Se_{2-2x}$ alloy nanosheets with composition-tunable electronic properties, Nano Lett. 16 (2016) 264–269.

[24] H.-P. Komsa, A.V. Krasheninnikov, Two-dimensional transition metal dichalcogenide alloys: stability and electronic properties, J. Phys. Chem. Lett. 3 (2012) 3652–3656.

[25] Y. Gong, Z. Liu, A.R. Lupini, G. Shi, J. Lin, S. Najmaei, Z. Lin, A.L. Elías, A. Berkdemir, G. You, Band gap engineering and layer-by-layer mapping of selenium-doped molybdenum disulfide, Nano Lett. 14 (2014) 442–449.

[26] Z. Lin, M.T. Thee, A.L. Elías, S. Feng, C. Zhou, K. Fujisawa, N. Perea-López, V. Carozo, H. Terrones, M. Terrones, Facile synthesis of MoS_2 and $Mo_xW_{1-x}S_2$ triangular monolayers, APL Mater. 2 (2014), 092514.

[27] J. Zhang, S. Jia, I. Kholmanov, L. Dong, D. Er, W. Chen, H. Guo, Z. Jin, V.B. Shenoy, L. Shi, Janus monolayer transition-metal dichalcogenides, ACS Nano 11 (2017) 8192–8198.

[28] A.-Y. Lu, H. Zhu, J. Xiao, C.-P. Chuu, Y. Han, M.-H. Chiu, C.-C. Cheng, C.-W. Yang, K.-H. Wei, Y. Yang, Janus monolayers of transition metal dichalcogenides, Nat. Nanotechnol. 12 (2017) 744–749.

[29] Q.-F. Yao, J. Cai, W.-Y. Tong, S.-J. Gong, J.-Q. Wang, X. Wan, C.-G. Duan, J. Chu, Manipulation of the large Rashba spin splitting in polar two-dimensional transition-metal dichalcogenides, Phys. Rev. B 95 (2017), 165401.

[30] Y. Cheng, Z. Zhu, M. Tahir, U. Schwingenschlögl, Spin-orbit–induced spin splittings in polar transition metal dichalcogenide monolayers, EPL (Europhysics Letters) 102 (2013) 57001.

[31] F. Li, W. Wei, P. Zhao, B. Huang, Y. Dai, Electronic and optical properties of pristine and vertical and lateral heterostructures of Janus MoSSe and WSSe, J. Phys. Chem. Lett. 8 (2017) 5959–5965.

[32] T. Hu, F. Jia, G. Zhao, J. Wu, A. Stroppa, W. Ren, Intrinsic and anisotropic Rashba spin splitting in Janus transition-metal dichalcogenide monolayers, Phys. Rev. B 97 (2018), 235404.

[33] F. Xiao, W. Lei, W. Wang, C. Autieri, X. Zheng, X. Ming, J. Luo, Pressure-induced structural transition, metallization, and topological superconductivity in PdSSe, Phys. Rev. B 105 (2022), 115110.

[34] Y.-L. Hong, Z. Liu, L. Wang, T. Zhou, W. Ma, C. Xu, S. Feng, L. Chen, M.-L. Chen, D.-M. Sun, Chemical vapor deposition of layered two-dimensional $MoSi_2N_4$ materials, Science 369 (2020) 670–674.

[35] L. Cao, G. Zhou, Q. Wang, L. Ang, Y.S. Ang, Two-dimensional van der Waals electrical contact to monolayer $MoSi_2N_4$, Appl. Phys. Lett. 118 (2021), 013106.

[36] A. Bafekry, M. Faraji, D. Hoat, M. Shahrokhi, M. Fadlallah, F. Shojaei, S. Feghhi, M. Ghergherehchi, D. Gogova, $MoSi_2N_4$ single-layer: a novel two-dimensional material with outstanding mechanical, thermal, electronic and optical properties, J. Phys. D Appl. Phys. 54 (2021), 155303.

[37] B. Mortazavi, B. Javvaji, F. Shojaei, T. Rabczuk, A.V. Shapeev, X. Zhuang, Exceptional piezoelectricity, high thermal conductivity and stiffness and promising photocatalysis in two-dimensional $MoSi_2N_4$ family confirmed by first-principles, Nano Energy 82 (2021), 105716.

[38] C.-C. Jian, X. Ma, J. Zhang, X. Yong, Strained $MoSi_2N_4$ monolayers with excellent solar energy absorption and carrier transport properties, J. Phys. Chem. C 125 (2021) 15185–15193.

[39] Q. Wang, L. Cao, S.-J. Liang, W. Wu, G. Wang, C.H. Lee, W.L. Ong, H.Y. Yang, L. K. Ang, S.A. Yang, Efficient Ohmic contacts and built-in atomic sublayer protection in $MoSi_2N_4$ and WSi_2N_4 monolayers, npj 2D, Mater. Appl. 5 (2021) 1–9.

[40] J. Yu, J. Zhou, X. Wan, Q. Li, High intrinsic lattice thermal conductivity in monolayer $MoSi_2N_4$, New J. Phys. 23 (2021), 033005.

[41] Z. Cui, Y. Luo, J. Yu, Y. Xu, Tuning the electronic properties of $MoSi_2N_4$ by molecular doping: a first principles investigation, Physica E 134 (2021), 114873.

[42] A. Bafekry, M. Faraji, M.M. Fadlallah, A.B. Khatibani, A. abdolahzadeh Ziabari, M. Ghergherehchi, S. Nedaei, S.F. Shayesteh, D. Gogova, Tunable electronic and magnetic properties of $MoSi_2N_4$ monolayer via vacancy defects, atomic adsorption and atomic doping, Appl. Surf. Sci. 559 (2021) 149862.

[43] H. Yao, C. Zhang, Q. Wang, J. Li, Y. Yu, F. Xu, B. Wang, Y. Wei, Novel Two-Dimensional Layered $MoSi_2Z_4$ (Z= P, As): New Promising Optoelectronic Materials, Nanomaterials 11 (2021) 559.

[44] X. Lv, Y. Xu, B. Mao, G. Liu, G. Zhao, J. Yang, Strain modulation of electronic and optical properties of monolayer $MoSi_2N_4$, Physica E 135 (2022), 114964.

[45] D. Pham, Electronic properties of a two-dimensional van der Waals $MoGe_2N_4$/$MoSi_2N_4$ heterobilayer: Effect of the insertion of a graphene layer and interlayer coupling, RSC Adv. 11 (2021) 28659–28666.

[46] G. Yuan, Z. Cheng, Y. Cheng, W. Duan, H. Lv, M. Wang, X. Ma, Highly Sensitive Band Alignment of Graphene/$MoSi_2N_4$Heterojunction Via External Electric Field, Available at SSRN 4052449.

[47] L. Cao, G. Zhou, Q. Wang, L. Ang, Y.S. Ang, Two-dimensional van der Waals electrical contact to monolayer MoSi, (2021).

[48] R. Chen, D. Chen, W. Zhang, First-principles calculations to investigate stability, electronic and optical properties of fluorinated $MoSi_2N_4$ monolayer, Results Phys. 30 (2021), 104864.

[49] A. Bafekry, M. Faraji, C. Stampfl, I.A. Sarsari, A.A. Ziabari, N. Hieu, S. Karbasizadeh, M. Ghergherehchi, Band-gap engineering, magnetic behavior and Dirac-semimetal character in the $MoSi_2N_4$ nanoribbon with armchair and zigzag edges, J. Phys. D Appl. Phys. 55 (2021), 035301.

[50] A. Ray, S. Tyagi, N. Singh, U. Schwingenschlogl, Inducing Half-Metallicity in Monolayer $MoSi_2N_4$, ACS Omega 6 (2021) 30371–30375.

[51] J.Q. Ng, Q. Wu, L. Ang, Y.S. Ang, Tunable electronic properties and band alignments of $MoSi_2N_4$/GaN and $MoSi_2N_4$/ZnO van der Waals heterostructures, Appl. Phys. Lett. 120 (2022), 103101.

[52] J. Xu, Q. Wu, Z. Sun, N. Mwankemwa, W.-B. Zhang, W.-X. Yang, First-principles investigations of electronic, optical, and photocatalytic properties of Au-adsorbed $MoSi_2N_4$ monolayer, J. Phys. Chem. Solids 162 (2022), 110494.

[53] A. Bafekry, C. Stampfl, M. Naseri, M.M. Fadlallah, M. Faraji, M. Ghergherehchi, D. Gogova, S. Feghhi, Effect of electric field and vertical strain on the electro-optical properties of the $MoSi_2N_4$ bilayer: A first-principles calculation, J. Appl. Phys. 129 (2021), 155103.

[54] Q. Li, W. Zhou, X. Wan, J. Zhou, Strain effects on monolayer $MoSi_2N_4$: Ideal strength and failure mechanism, Physica E 131 (2021), 114753.

[55] R. Islam, R. Verma, B. Ghosh, Z. Muhammad, A. Bansil, C. Autieri, B. Singh, Switchable large-gap quantum spin Hall state in two-dimensional MSi_2Z_4 materials class, arXiv preprint arXiv:2207.08407, (2022).

[56] G. Hussain, M. Asghar, M.W. Iqbal, H. Ullah, C. Autieri, Exploring the structural stability, electronic and thermal attributes of synthetic 2D materials and their heterostructures, Appl. Surf. Sci. 590 (2022), 153131.
[57] C. Yang, Z. Song, X. Sun, J. Lu, Valley pseudospin in monolayer $MoSi_2N_4$ and $MoSi_2As_4$, Phys. Rev. B 103 (2021), 035308.
[58] R. Islam, B. Ghosh, C. Autieri, S. Chowdhury, A. Bansil, A. Agarwal, B. Singh, Tunable spin polarization and electronic structure of bottom-up synthesized $MoSi_2N_4$ materials, Phys. Rev. B 104 (2021) L201112.
[59] H. Ai, D. Liu, J. Geng, S. Wang, K.H. Lo, H. Pan, Theoretical evidence of the spin–valley coupling and valley polarization in two-dimensional MoSi2X4 X= N, P, and As, PCCP 23 (2021) 3144–3151.
[60] Y. Liu, T. Zhang, K. Dou, W. Du, R. Peng, Y. Dai, B. Huang, Y. Ma, Valley-contrasting physics in single-layer $CrSi_2N_4$ and $CrSi_2P_4$, J. Phys. Chem. Lett. 12 (2021) 8341–8346.
[61] G. Hussain, M. Manzoor, M.W. Iqbal, I. Muhammad, A. Bafekry, H. Ullah, C. Autieri, Strain modulated electronic and optical properties of laterally stitched $MoSi_2N_4$/XSi_2N_4 (X= W, Ti) 2D heterostructures, Physica E: Low-dimensional Syst. Nanostruct. (2022) 115471.
[62] S. Datta, B. Das, Electronic analog of the electro-optic modulator, Appl. Phys. Lett. 56 (1990) 665–667.
[63] G. Kresse, D. Joubert, From ultrasoft pseudopotentials to the projector augmented-wave method, Phys. Rev. b 59 (1999) 1758.
[64] G. Kresse, J. Furthmüller, Efficient iterative schemes for ab initio total-energy calculations using a plane-wave basis set, Phys. Rev. B 54 (1996) 11169.
[65] J.P. Perdew, K. Burke, M. Ernzerhof, Generalized gradient approximation made simple, Phys. Rev. Lett. 77 (1996) 3865.
[66] A. Togo, I. Tanaka, First principles phonon calculations in materials science, Scr. Mater. 108 (2015) 1–5.
[67] Y. Ma, Y. Dai, W. Wei, X. Li, B. Huang, Emergence of electric polarity in BiTeX (X= Br and I) monolayers and the giant Rashba spin splitting, PCCP 16 (2014) 17603–17609.
[68] S.V. Eremeev, I.A. Nechaev, Y.M. Koroteev, P.M. Echenique, E.V. Chulkov, Ideal two-dimensional electron systems with a giant Rashba-type spin splitting in real materials: surfaces of bismuth tellurohalides, Phys. Rev. Lett. 108 (2012), 246802.
[69] D. Di Sante, A. Stroppa, P. Barone, M.-H. Whangbo, S. Picozzi, Emergence of ferroelectricity and spin-valley properties in two-dimensional honeycomb binary compounds, Phys. Rev. B 91 (2015), 161401.
[70] H.J. Zhao, H. Nakamura, R. Arras, C. Paillard, P. Chen, J. Gosteau, X. Li, Y. Yang, L. Bellaiche, Purely Cubic Spin Splittings with Persistent Spin Textures, Phys. Rev. Lett. 125 (2020), 216405.
[71] C. Autieri, P. Barone, J. Sławińska, S. Picozzi, Persistent spin helix in Rashba-Dresselhaus ferroelectric $CsBiNb_2O_7$, Phys. Rev. Mater. 3 (2019), 084416.
[72] S. Sheoran, D. Gill, A. Phutela, S. Bhattacharya, Coupled spin-valley, Rashba effect and hidden persistent spin polarization in WSi_2N_4 family, arXiv preprint arXiv: 2208.00127, (2022).

Emergence of Rashba splitting and spin-valley properties in Janus $MoGeSiP_2As_2$ and $WGeSiP_2As_2$ monolayers

Ghulam Hussain,[a,*] Abdus Samad,[b] Majeed Ur Rehman,[c,*] Giuseppe Cuono,[a] Carmine Autieri[a]

[a]International Research Centre MagTop, Institute of Physics, Polish Academy of Sciences, Aleja Lotnikow 32/46, PL-02668 Warsaw, Poland

[b]Department of Physics and Energy Harvest Storage Center, University of Ulsan, Ulsan 44610, South Korea

[c]College of Physics and Optoelectronic Engineering, Shenzhen University, Shenzhen, Guangdong 518060, China

E-mail: ghussain@ifpan.edu.pl, majeed@mail.ustc.edu.cn

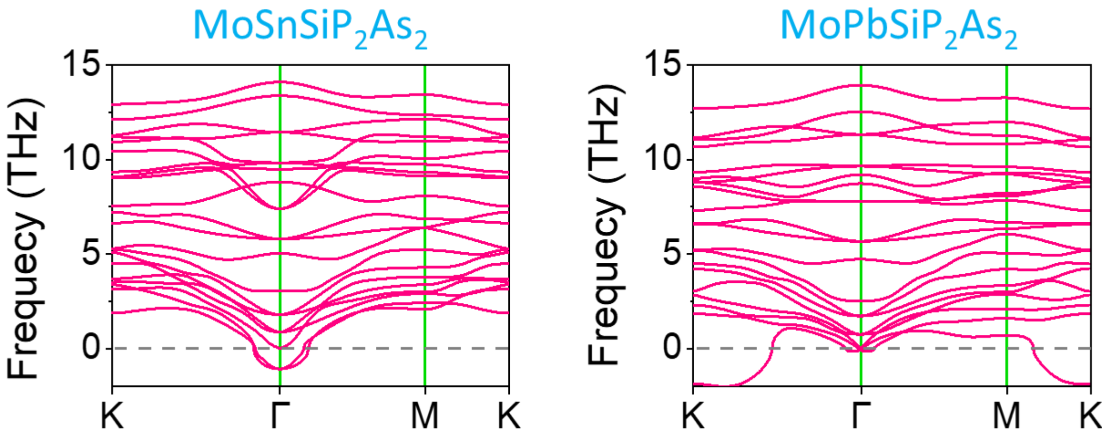

Figure S1 Phonon spectra of Janus $MoSnSiP_2As_2$ and $MoPbSiP_2As_2$ monolayers. Since, the structures show negative phonon modes, they are dynamically unstable.

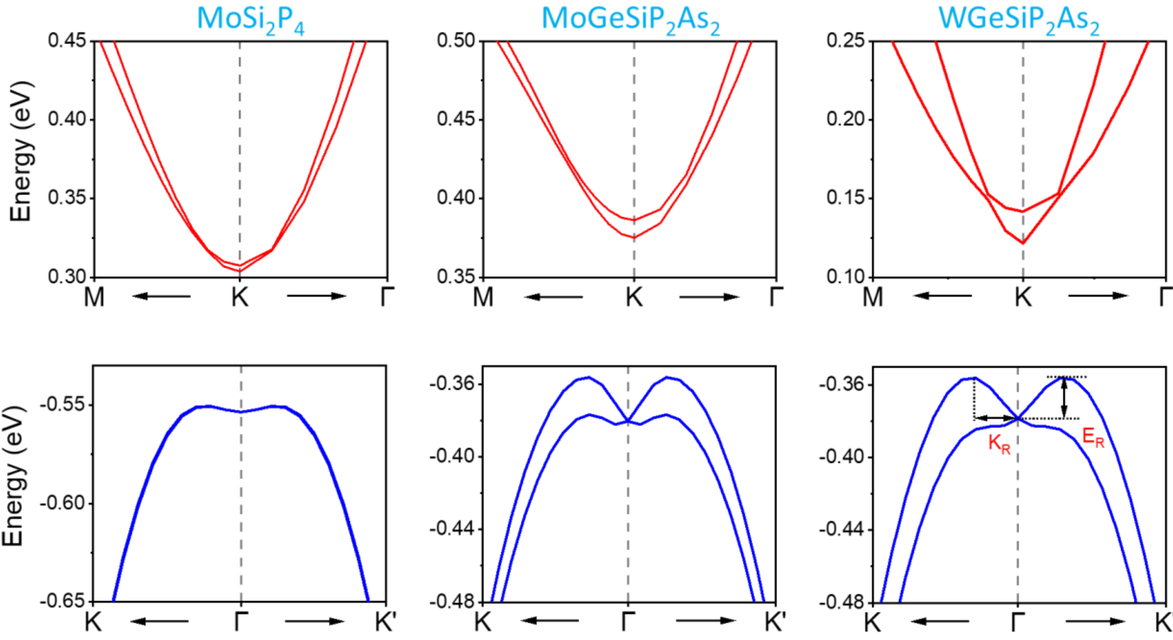

Figure S2 Zoomed illustrations of the conduction band split states λ_{Kc} at K-point, and that of valence band at Γ-point for the pristine and Janus phases to investigate the Rashba-type spin splitting.

Optical spectra

In studying the optical properties, the dielectric function of a material is a unique feature that describes the interaction of an oscillating light wave in the form of electric field with the material. The dielectric function can be used to derive other linear optical features, for instance, in Fig. S3, the plots for the absorbance and reflectance are illustrated. Using PBE functional, we computed the absorbance spectra of monolayer $MoSi_2P_4$ in pristine and Janus $XGeSiP_2As_2$ structures as shown. We noticed that both the pristine as well as Janus phases have characteristic absorption peaks in the infra-red region, which correspond to direct optical transitions in the band structures (e.g. the first absorbance peaks occur at the photon energies equal to the electronic band gaps at the K-point). Intriguingly, the first absorbance peak is red-shifted to 0.25 eV ($WGeSiP_2As_2$) from 0.57 eV ($MoGeSiP_2As_2$) offering the possibility to tune the IR range. In addition, for pristine

$MoSi_2P_4$ this corresponds to a wavelength of 2 μm, while for the Janus phase of $WGeSiP_2As_2$ this corresponds to a wavelength of ~5 μm employing their applications in the near- and mid-IR detector applications, respectively. Moreover, we show the reflectance spectra for the pristine and Janus structures in Fig S3(b), which indicate almost negligible reflectance in the IR range, and thus employ their utilization in the IR photo-detector devices.

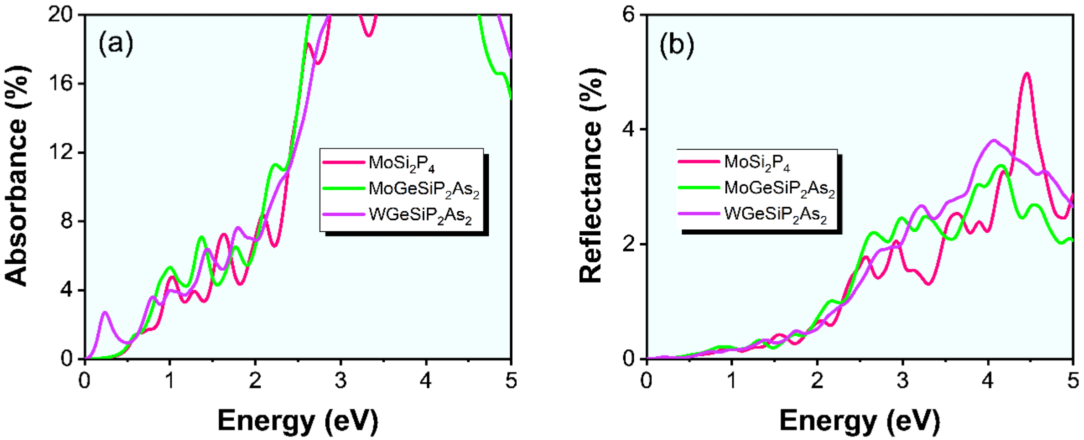

Figure S3 Comparison of the optical spectra of pristine $MoSi_2P_4$ with those of Janus $XGeSiP_2As_2$ structures indicated (a) Absorbance, and (b) Reflectance.

Chapter 6

CONCLUSIONS

In summary, using the first-principles calculations, we have investigated the optoelectronic features of 3D InAs/$InAs_{0.625}Sb_{0.375}$ SLs, 2D materials XSi_2N_4 (Mo, W, Ti) and their heterostructures, and Janus structures, respectively. We propose these materials as feasible optoelectronic materials that covers the range from far-IR to visible part of electromagnetic spectrum. While studying the electronic and optical attributes, we noticed significant variations as we moved from bulk InAs, InSb to the InAs/$InAs_{0.625}Sb_{0.375}$ SLs. Also, the properties are strongly depending on the lattice constant of the superlattice, which can be tuned effectively to cover the different regions of far-detection. The existence of two heavy-hole bands with increasing in-plane effective mass as one goes far from the Fermi level is observed. Besides, we noted a substantial decrease in the effective masses of heavy-holes, and energy gaps in the k_x-k_y plane with respect to their bulk counterpart. We discovered that the electrons are delocalized in the InAs part of SL, while the holes are localized in the $InAs_{0.625}Sb_{0.375}$ part giving rise to type II superlattice. Moreover, the absorption spectra in the far-infrared regime are strongly increased for InAs/$InAs_{0.625}Sb_{0.375}$ SLs as compared to bulk InAs and InSb suggesting their suitability in IR photodetectors.

Together with the 3D superlattice, we successfully demonstrated the thermodynamical stability of the novel 2D materials family, their heterostructures and Janus structures. We performed computationally demanding calculations for the realistic systems combining spin-orbit coupling, HSE functional and the strain induced engineering of electro-optical properties. It is established that the monolayers and the heterostructures are stable and experimentally accessible as confirmed by the total energy ground state calculations and the phonon spectra. After confirming the structural stability, we presented the electronic band structures and the density of states for the monolayered materials such as XSi_2N_4 (M = Mo, W, and Ti), and their 2D heterostructures $MoSi_2N_4$/XSi_2N_4, (X=W, Ti) revealing a semiconducting behavior with the band gaps ranging from the infrared to the visible region. The band structure for $MoSi_2N_4$/WSi_2N_4 heterostructure exposed that its bandgap lies in the visible region employing their applications for photovoltaics and other optoelectronic devices. However, for 'Ti' incorporated heterostructure ($MoSi_2N_4$/$TiSi_2N_4$) the band gap drops to the IR range providing the opportunity to utilize these heterostructures as IR detector materials. In addition, the effect of biaxial strain on the

optoelectronic properties of laterally stitched 2D heterostructures manifested significant modifications in the electronic band structures and optical properties. We noticed that the compressive strain causes a transition from indirect to direct band gap semiconductor in $MoSi_2N_4/WSi_2N_4$, while a semiconducting to metallic transition in $MoSi_2N_4/TiSi_2N_4$. Besides, the optical spectra including absorbance, transmittance and reflectance can be tuned efficiently using biaxial strain. Our findings based on the electro-optical properties and their controlled modulation via biaxial strain suggest the applications of these newly discovered 2D materials and heterostructures in nano- and optoelectronics.

Lastly, an explicit study on the pristine $MoSi_2P_4$ and Janus $XGeSiP_2As_2$ (X = Mo, W) monolayers of these recently discovered 2D materials is carried out. Both, the pristine and Janus phases were demonstrated to be thermodynamically. We observed an intrinsic spin splitting at the K/K'-points of the pristine $MoSi_2P_4$ in the electronic band structures, which is further enhanced in the Janus structure, suggesting their valleytronic applications. In addition, the broken mirror symmetry in Janus phase induces an out-of-plane electric field that results in splitting of valence bands at the Γ-point not only in energy but also in momentum space, a signature of Rashba-type spin splitting, which occurs due to the asymmetric potential in the Janus phase, perpendicular to the basal plane. Moreover, we noticed characteristic absorption peaks in the infra-red region for both the pristine as well as the Janus phases (shown in supplementary material) employing their use in the IR devices. The large spin and Rashba-type splittings together with the exceptional optical spectra in these structures can make extraordinary contribution in the valleytronics, spintronics and IR applications.

References

1. Adams, F. and C. Barbante, *Nanotechnology and analytical chemistry*, in *Comprehensive Analytical Chemistry*. 2015, Elsevier. p. 125-157.
2. Herschel, W., *XIV. Experiments on the refrangibility of the invisible rays of the sun.* Philosophical Transactions of the Royal Society of London, 1800(90): p. 284-292.
3. Barr, E.S., *Historical survey of the early development of the infrared spectral region.* American Journal of physics, 1960. **28**(1): p. 42-54.
4. Barr, E.S., *The infrared pioneers—I. Sir William Herschel.* Infrared Physics, 1961. **1**: p. 1-2.
5. Barr, E.S., *The infrared pioneers—II. Macedonio melloni.* Infrared physics, 1962. **2**(2): p. 67-74.
6. Hudson, R.D., *Infrared system engineering*. Vol. 1. 1969: Wiley-Interscience New York.
7. Rogalski, A., *History of infrared detectors.* Opto-Electronics Review, 2012. **20**(3): p. 279-308.
8. Barr, E.S., *The infrared pioneers—III. Samuel pierpont Langley.* Infrared physics, 1963. **3**(4): p. 195-206.
9. Langley, S.P. *The bolometer and radiant energy*. in *Proceedings of the American Academy of Arts and Sciences*. 1880. JSTOR.
10. Walcott, C.D., *Biographical Memoir of Samuel Pierpont Langley, 1834-1906*. Vol. 7. 1912: National Academy of Sciences.
11. Hertz, H., *Ueber einen Einfluss des ultravioletten Lichtes auf die electrische Entladung.* Annalen der Physik, 1887. **267**(8): p. 983-1000.
12. Elster, J. and H. Geitel, *Ueber die Entladung negativ electrischer Körper durch das Sonnen-und Tageslicht.* Annalen der Physik, 1889. **274**(12): p. 497-514.
13. Case, T.W., *Notes on the change of resistance of certain substances in light.* Physical Review, 1917. **9**(4): p. 305.
14. Kruse, P.W., L.D. McGlauchlin, and R.B. McQuistan, *Elements of infrared technology: Generation, transmission and detection.* New York: Wiley, 1962.
15. Cashman, R., *Film-type infrared photoconductors.* Proceedings of the IRE, 1959. **47**(9): p. 1471-1475.
16. Lovell, D., *Cashman thallous sulfide cell.* Applied optics, 1971. **10**(5): p. 1003-1008.
17. Lovell, D., *The development of lead salt detectors.* American Journal of Physics, 1969. **37**(5): p. 467-478.
18. Rollin, B. and E. Simmons, *Long Wavelength Infra-Red Photoconductivity of Silicon at Low Temperatures.* Proceedings of the Physical Society. Section B, 1952. **65**(12): p. 995.

19. Burstein, E., J. Oberly, and J. Davisson, *Infrared photoconductivity due to neutral impurities in silicon.* Physical Review, 1953. **89**(1): p. 331.
20. Borrello, S.R. and H. Levinstein, *Preparation and Properties of Mercury-Doped Germanium.* Journal of Applied Physics, 1962. **33**(10): p. 2947-2950.
21. Biberman, L. and R. Sendall, *Introduction: A brief history of imaging devices for night vision.* Electro-optical imaging: system performance and modelling, 2000.
22. Lawson, W., et al., *Preparation and properties of HgTe and mixed crystals of HgTe-CdTe.* Journal of Physics and Chemistry of Solids, 1959. **9**(3-4): p. 325-329.
23. Melngailis, I. and T. Harman, *Single-crystal lead-tin chalcogenides*, in *Semiconductors and Semimetals*. 1970, Elsevier. p. 111-174.
24. Harman, T. and I. Melngailis, *Narrow gap semiconductors*, in *Applied Solid State Science*. 1974, Elsevier. p. 1-94.
25. Dornhaus, R. and G. Nimtz, *The properties and applications of the Hg 1− x Cd x Te alloy system.* Narrow-Gap Semiconductors, 1983: p. 119-281.
26. Preier, H., *New aspects of the material and device technology of intrinsic infrared photodetectors*, in *Physics of Narrow Gap Semiconductors*. 1982, Springer. p. 280-282.
27. Long, D. and J.L. Schmit, *Mercury-cadmium telluride and closely related alloys*, in *Semiconductors and semimetals*. 1970, Elsevier. p. 175-255.
28. Smith, D. and C. Mailhiot, *Proposal for strained type II superlattice infrared detectors.* Journal of Applied Physics, 1987. **62**(6): p. 2545-2548.
29. Levine, B., *Quantum-well infrared photodetectors.* Journal of applied physics, 1993. **74**(8): p. R1-R81.
30. Rogalski, A., *Infrared detectors: status and trends.* Progress in quantum electronics, 2003. **27**(2-3): p. 59-210.
31. Schneider, H. and H.C. Liu, *Quantum well infrared photodetectors.* 2007.
32. Rogalski, A. and R. Ciupa, *Performance limitation of short wavelength infrared InGaAs and HgCdTe photodiodes.* Journal of electronic materials, 1999. **28**(6): p. 630-636.
33. Tidrow, M.Z., et al. *Device physics and focal plane array applications of QWIP and MCT.* in *Photodetectors: Materials and Devices IV*. 1999. SPIE.
34. Rogalski, A., P. Martyniuk, and M. Kopytko, *InAs/GaSb type-II superlattice infrared detectors: Future prospect.* Applied physics reviews, 2017. **4**(3): p. 031304.
35. Rogalski, A., et al., *InAsSb-based infrared photodetectors: Thirty years later on.* Sensors, 2020. **20**(24): p. 7047.
36. Ting, D.Z., et al., *InAs/InAsSb type-II strained-layer superlattice infrared photodetectors.* Micromachines, 2020. **11**(11): p. 958.
37. Ting, D.Z., et al., *Long wavelength InAs/InAsSb infrared superlattice challenges: A theoretical investigation.* Journal of Electronic Materials, 2020. **49**(11): p. 6936-6945.
38. Martyniuk, P., et al., *Theoretical modeling of XBn T2SLs InAs/InAsSb/B-AlSb longwave infrared detector operating under thermoelectrical cooling.* Optical and Quantum Electronics, 2020. **52**(2): p. 1-10.

39. Ting, D.Z., et al., *Advances in III-V semiconductor infrared absorbers and detectors.* Infrared Physics & Technology, 2019. **97**: p. 210-216.
40. Long, M., et al., *Palladium diselenide long-wavelength infrared photodetector with high sensitivity and stability.* ACS nano, 2019. **13**(2): p. 2511-2519.
41. Steenbergen, E., et al., *Significantly improved minority carrier lifetime observed in a long-wavelength infrared III-V type-II superlattice comprised of InAs/InAsSb.* Applied Physics Letters, 2011. **99**(25): p. 251110.
42. Klipstein, P., et al., *Modeling InAs/GaSb and InAs/InAsSb superlattice infrared detectors.* Journal of electronic materials, 2014. **43**(8): p. 2984-2990.
43. Lu, Q., W. Liu, and X. Wang, *2-D material-based photodetectors on flexible substrates.* Inorganic Flexible Optoelectronics: Materials and Applications, 2019: p. 117-142.
44. Moore, M., *International roadmap for devices and systems.* Accessed: Jan, 2020.
45. Bonaccorso, F., et al., *Graphene photonics and optoelectronics.* Nature photonics, 2010. **4**(9): p. 611-622.
46. Li, X., et al., *Graphene and related two-dimensional materials: Structure-property relationships for electronics and optoelectronics.* Applied Physics Reviews, 2017. **4**(2): p. 021306.
47. Bae, S., et al., *Roll-to-roll production of 30-inch graphene films for transparent electrodes.* Nature nanotechnology, 2010. **5**(8): p. 574-578.
48. Akinwande, D., N. Petrone, and J. Hone, *Two-dimensional flexible nanoelectronics.* Nature communications, 2014. **5**(1): p. 1-12.
49. Xia, F., et al., *Ultrafast graphene photodetector.* Nature nanotechnology, 2009. **4**(12): p. 839-843.
50. Wang, G., et al., *Two dimensional materials based photodetectors.* Infrared Physics & Technology, 2018. **88**: p. 149-173.
51. Grigorenko, A.N., M. Polini, and K. Novoselov, *Graphene plasmonics.* Nature photonics, 2012. **6**(11): p. 749-758.
52. Sun, Z., et al., *Graphene mode-locked ultrafast laser.* ACS nano, 2010. **4**(2): p. 803-810.
53. Liu, M., et al., *A graphene-based broadband optical modulator.* Nature, 2011. **474**(7349): p. 64-67.
54. Rogalski, A., M. Kopytko, and P. Martyniuk, *Two-dimensional infrared and terahertz detectors: Outlook and status.* Applied Physics Reviews, 2019. **6**(2): p. 021316.
55. Nicolosi, V., et al., *Liquid exfoliation of layered materials.* Science, 2013. **340**(6139): p. 1226419.
56. Zhang, B., et al., *Recent progress in 2D material-based saturable absorbers for all solid-state pulsed bulk lasers.* Laser & Photonics Reviews, 2020. **14**(2): p. 1900240.
57. Wang, J., et al., *Recent progress on localized field enhanced two-dimensional material photodetectors from ultraviolet—visible to infrared.* Small, 2017. **13**(35): p. 1700894.
58. Buscema, M., et al., *Photocurrent generation with two-dimensional van der Waals semiconductors.* Chemical Society Reviews, 2015. **44**(11): p. 3691-3718.

59. Long, M., et al., *Progress, challenges, and opportunities for 2D material based photodetectors.* Advanced Functional Materials, 2019. **29**(19): p. 1803807.
60. Wang, F., et al., *2D library beyond graphene and transition metal dichalcogenides: a focus on photodetection.* Chemical Society Reviews, 2018. **47**(16): p. 6296-6341.
61. Cheng, J., et al., *Recent advances in optoelectronic devices based on 2D materials and their heterostructures.* Advanced Optical Materials, 2019. **7**(1): p. 1800441.
62. Britnell, L., et al., *Strong light-matter interactions in heterostructures of atomically thin films.* Science, 2013. **340**(6138): p. 1311-1314.
63. Dai, Z., L. Liu, and Z. Zhang, *Strain engineering of 2D materials: issues and opportunities at the interface.* Advanced Materials, 2019. **31**(45): p. 1805417.
64. Pi, L., et al., *Recent progress on 2D noble-transition-metal dichalcogenides.* Advanced Functional Materials, 2019. **29**(51): p. 1904932.
65. Zhang, W., et al., *Two-dimensional semiconductors with possible high room temperature mobility.* Nano Research, 2014. **7**(12): p. 1731-1737.
66. Zhao, Y., et al., *High-electron-mobility and air-stable 2D layered PtSe2 FETs.* Advanced Materials, 2017. **29**(5): p. 1604230.
67. Kuc, A., N. Zibouche, and T. Heine, *Influence of quantum confinement on the electronic structure of the transition metal sulfide T S 2.* Physical Review B, 2011. **83**(24): p. 245213.
68. Kumar, A. and P. Ahluwalia, *Electronic structure of transition metal dichalcogenides monolayers 1H-MX2 (M= Mo, W; X= S, Se, Te) from ab-initio theory: new direct band gap semiconductors.* The European Physical Journal B, 2012. **85**(6): p. 1-7.
69. Mak, K.F. and J. Shan, *Photonics and optoelectronics of 2D semiconductor transition metal dichalcogenides.* Nature Photonics, 2016. **10**(4): p. 216-226.
70. Radisavljevic, B., et al., *Single-layer MoS2 transistors.* Nature nanotechnology, 2011. **6**(3): p. 147-150.
71. Eda, G. and S.A. Maier, *Two-dimensional crystals: managing light for optoelectronics.* ACS nano, 2013. **7**(7): p. 5660-5665.
72. Cheng, Y., et al., *Spin-orbit–induced spin splittings in polar transition metal dichalcogenide monolayers.* EPL (Europhysics Letters), 2013. **102**(5): p. 57001.
73. Kuc, A. and T. Heine, *The electronic structure calculations of two-dimensional transition-metal dichalcogenides in the presence of external electric and magnetic fields.* Chemical Society Reviews, 2015. **44**(9): p. 2603-2614.
74. Zhu, Z.Y., Y.C. Cheng, and U. Schwingenschlögl, *Giant spin-orbit-induced spin splitting in two-dimensional transition-metal dichalcogenide semiconductors.* Physical Review B, 2011. **84**(15): p. 153402.
75. Zibouche, N., et al., *Transition-metal dichalcogenides for spintronic applications.* Annalen der Physik, 2014. **526**(9-10): p. 395-401.
76. Zeng, H., et al., *Valley polarization in MoS2 monolayers by optical pumping.* Nature nanotechnology, 2012. **7**(8): p. 490-493.

77. Mak, K.F., et al., *Control of valley polarization in monolayer MoS2 by optical helicity.* Nature nanotechnology, 2012. **7**(8): p. 494-498.
78. Xiao, D., et al., *Coupled spin and valley physics in monolayers of MoS 2 and other group-VI dichalcogenides.* Physical review letters, 2012. **108**(19): p. 196802.
79. Lv, R., et al., *Transition metal dichalcogenides and beyond: synthesis, properties, and applications of single-and few-layer nanosheets.* Accounts of chemical research, 2015. **48**(1): p. 56-64.
80. Wang, Q.H., et al., *Electronics and optoelectronics of two-dimensional transition metal dichalcogenides.* Nature nanotechnology, 2012. **7**(11): p. 699-712.
81. Novoselov, K., et al., *2D materials and van der Waals heterostructures.* Science, 2016. **353**(6298): p. aac9439.
82. Li, X., et al., *2D Re-Based Transition Metal Chalcogenides: Progress, Challenges, and Opportunities.* Advanced Science, 2020. **7**(23): p. 2002320.
83. Gong, C., et al., *Electronic and optoelectronic applications based on 2D novel anisotropic transition metal dichalcogenides.* Advanced Science, 2017. **4**(12): p. 1700231.
84. Withers, F., et al., *Light-emitting diodes by band-structure engineering in van der Waals heterostructures.* Nature materials, 2015. **14**(3): p. 301-306.
85. Liu, Y., et al., *Van der Waals heterostructures and devices.* Nature Reviews Materials, 2016. **1**(9): p. 1-17.
86. Liu, Z., et al., *In-plane heterostructures of graphene and hexagonal boron nitride with controlled domain sizes.* Nature nanotechnology, 2013. **8**(2): p. 119-124.
87. Roy, K., et al., *Graphene–MoS2 hybrid structures for multifunctional photoresponsive memory devices.* Nature nanotechnology, 2013. **8**(11): p. 826-830.
88. Yu, W.J., et al., *Highly efficient gate-tunable photocurrent generation in vertical heterostructures of layered materials.* Nature nanotechnology, 2013. **8**(12): p. 952-958.
89. Yu, W.J., et al., *Vertically stacked multi-heterostructures of layered materials for logic transistors and complementary inverters.* Nature materials, 2013. **12**(3): p. 246-252.
90. Li, M.-Y., et al., *Epitaxial growth of a monolayer WSe2-MoS2 lateral pn junction with an atomically sharp interface.* Science, 2015. **349**(6247): p. 524-528.
91. Chen, C., et al., *Synthesis of Large-Area Uniform MoS2–WS2 Lateral Heterojunction Nanosheets for Photodetectors.* ACS Applied Nano Materials, 2021. **4**(5): p. 5522-5530.
92. Swain, G., S. Sultana, and K. Parida, *A review on vertical and lateral heterostructures of semiconducting 2D-MoS 2 with other 2D materials: A feasible perspective for energy conversion.* Nanoscale, 2021. **13**(22): p. 9908-9944.
93. Ling, X., et al., *Parallel stitching of 2D materials.* Advanced materials, 2016. **28**(12): p. 2322-2329.
94. Li, M.-Y., et al., *Heterostructures based on two-dimensional layered materials and their potential applications.* Materials Today, 2016. **19**(6): p. 322-335.
95. Antonova, I., *Vertical heterostructures based on graphene and other 2D materials.* Semiconductors, 2016. **50**(1): p. 66-82.

96. Iannaccone, G., et al., *Quantum engineering of transistors based on 2D materials heterostructures.* Nature nanotechnology, 2018. **13**(3): p. 183-191.
97. Yu, J.H., et al., *Vertical heterostructure of two-dimensional MoS2 and WSe2 with vertically aligned layers.* Nano letters, 2015. **15**(2): p. 1031-1035.
98. Nipane, A., et al., *Electrostatics of lateral pn junctions in atomically thin materials.* Journal of Applied Physics, 2017. **122**(19): p. 194501.
99. Yu, H., A. Kutana, and B.I. Yakobson, *Carrier delocalization in two-dimensional coplanar p–n junctions of graphene and metal dichalcogenides.* Nano letters, 2016. **16**(8): p. 5032-5036.
100. Tian, H., et al., *Novel field-effect Schottky barrier transistors based on graphene-MoS2 heterojunctions.* Scientific reports, 2014. **4**(1): p. 1-9.
101. Miao, J., et al., *High-responsivity graphene/InAs nanowire heterojunction near-infrared photodetectors with distinct photocurrent on/off ratios.* small, 2015. **11**(8): p. 936-942.
102. Chhowalla, M., et al., *The chemistry of two-dimensional layered transition metal dichalcogenide nanosheets.* Nature chemistry, 2013. **5**(4): p. 263-275.
103. Manzeli, S., et al., *2D transition metal dichalcogenides.* Nature Reviews Materials, 2017. **2**(8): p. 1-15.
104. Lei, W., et al., *Structural transition, metallization, and superconductivity in quasi-two-dimensional layered Pd S 2 under compression.* Physical Review B, 2020. **101**(20): p. 205149.
105. Iqbal, M.W., et al., *High-mobility and air-stable single-layer WS2 field-effect transistors sandwiched between chemical vapor deposition-grown hexagonal BN films.* Scientific reports, 2015. **5**(1): p. 1-9.
106. Ye, Z., et al., *Probing excitonic dark states in single-layer tungsten disulphide.* Nature, 2014. **513**(7517): p. 214-218.
107. Xi, J., et al., *Tunable electronic properties of two-dimensional transition metal dichalcogenide alloys: a first-principles prediction.* The journal of physical chemistry letters, 2014. **5**(2): p. 285-291.
108. Duan, X., et al., *Synthesis of WS2 x Se2–2 x alloy nanosheets with composition-tunable electronic properties.* Nano letters, 2016. **16**(1): p. 264-269.
109. Komsa, H.-P. and A.V. Krasheninnikov, *Two-dimensional transition metal dichalcogenide alloys: stability and electronic properties.* The journal of physical chemistry letters, 2012. **3**(23): p. 3652-3656.
110. Gong, Y., et al., *Band gap engineering and layer-by-layer mapping of selenium-doped molybdenum disulfide.* Nano letters, 2014. **14**(2): p. 442-449.
111. Lin, Z., et al., *Facile synthesis of MoS2 and MoxW1-xS2 triangular monolayers.* Apl Materials, 2014. **2**(9): p. 092514.
112. Zhang, J., et al., *Janus monolayer transition-metal dichalcogenides.* ACS nano, 2017. **11**(8): p. 8192-8198.

113. Lu, A.-Y., et al., *Janus monolayers of transition metal dichalcogenides.* Nature nanotechnology, 2017. **12**(8): p. 744-749.
114. Yao, Q.-F., et al., *Manipulation of the large Rashba spin splitting in polar two-dimensional transition-metal dichalcogenides.* Physical review B, 2017. **95**(16): p. 165401.
115. Li, F., et al., *Electronic and optical properties of pristine and vertical and lateral heterostructures of Janus MoSSe and WSSe.* The journal of physical chemistry letters, 2017. **8**(23): p. 5959-5965.
116. Hu, T., et al., *Intrinsic and anisotropic Rashba spin splitting in Janus transition-metal dichalcogenide monolayers.* Physical Review B, 2018. **97**(23): p. 235404.
117. Hong, Y.-L., et al., *Chemical vapor deposition of layered two-dimensional MoSi2N4 materials.* Science, 2020. **369**(6504): p. 670-674.
118. Lv, X., et al., *Strain modulation of electronic and optical properties of monolayer MoSi2N4.* Physica E: Low-dimensional Systems and Nanostructures, 2022. **135**: p. 114964.
119. Wu, Q., et al., *Semiconductor-to-metal transition in bilayer MoSi2N4 and WSi2N4 with strain and electric field.* Applied Physics Letters, 2021. **118**(11): p. 113102.
120. Wu, M. and J. Li, *Sliding ferroelectricity in 2D van der Waals materials: Related physics and future opportunities.* Proceedings of the National Academy of Sciences, 2021. **118**(50): p. e2115703118.
121. Islam, R., et al., *Switchable large-gap quantum spin Hall state in two-dimensional MSi $ _2 $ Z $ _4 $ materials class.* arXiv preprint arXiv:2207.08407, 2022.
122. Bafekry, A., et al., *MoSi2N4 single-layer: a novel two-dimensional material with outstanding mechanical, thermal, electronic and optical properties.* Journal of Physics D: Applied Physics, 2021. **54**(15): p. 155303.
123. Bafekry, A., et al., *Tunable electronic and magnetic properties of MoSi2N4 monolayer via vacancy defects, atomic adsorption and atomic doping.* Applied Surface Science, 2021. **559**: p. 149862.
124. Pham, D., *Electronic properties of a two-dimensional van der Waals MoGe 2 N 4/MoSi 2 N 4 heterobilayer: Effect of the insertion of a graphene layer and interlayer coupling.* RSC advances, 2021. **11**(46): p. 28659-28666.
125. Islam, R., et al., *Tunable spin polarization and electronic structure of bottom-up synthesized MoSi 2 N 4 materials.* Physical Review B, 2021. **104**(20): p. L201112.
126. Perdew, J.P., K. Burke, and M. Ernzerhof, *Generalized gradient approximation made simple.* Physical review letters, 1996. **77**(18): p. 3865.
127. Perdew, J.P., et al., *Atoms, molecules, solids, and surfaces: Applications of the generalized gradient approximation for exchange and correlation.* Physical review B, 1992. **46**(11): p. 6671.
128. Gupta, A., T. Sakthivel, and S. Seal, *Recent development in 2D materials beyond graphene.* Progress in Materials Science, 2015. **73**: p. 44-126.

129. Novoselov, K.S., et al., *Electric field effect in atomically thin carbon films.* science, 2004. **306**(5696): p. 666-669.
130. Geim, A.K. and K.S. Novoselov, *The rise of graphene*, in *Nanoscience and technology: a collection of reviews from nature journals*. 2010, World Scientific. p. 11-19.
131. Wu, D., et al., *High quantum efficiency mid-wavelength infrared type-II InAs/InAs1− xSbx superlattice photodiodes grown by metal-organic chemical vapor deposition.* Applied Physics Letters, 2019. **114**(1): p. 011104.
132. Moehle, C.M., et al., *InSbAs two-dimensional electron gases as a platform for topological superconductivity.* Nano Letters, 2021. **21**(23): p. 9990-9996.
133. Pikulin, D. and T. Hyart, *Interplay of exciton condensation and the quantum spin Hall effect in InAs/GaSb bilayers.* Physical Review Letters, 2014. **112**(17): p. 176403.
134. Winkler, G.W., et al., *Topological phases in InAs 1− x Sb x: from novel topological semimetal to Majorana wire.* Physical Review Letters, 2016. **117**(7): p. 076403.
135. Nguyen, N.M., et al., *Unprotected edge modes in quantum spin Hall insulator candidate materials.* arXiv preprint arXiv:2209.06912, 2022.
136. Mikhailova, M., K. Moiseev, and Y.P. Yakovlev, *Interface-induced optical and transport phenomena in type II broken-gap single heterojunctions.* Semiconductor science and technology, 2004. **19**(10): p. R109.
137. Hussain, G., et al., *Strain modulated electronic and optical properties of laterally stitched MoSi2N4/XSi2N4 (X= W, Ti) 2D heterostructures.* Physica E: Low-dimensional Systems and Nanostructures, 2022. **144**: p. 115471.
138. Zhong, T., et al., *Sliding ferroelectricity in two-dimensional MoA 2 N 4 (A= Si or Ge) bilayers: high polarizations and Moiré potentials.* Journal of Materials Chemistry A, 2021. **9**(35): p. 19659-19663.
139. Zhong, H., et al., *Strain-induced semiconductor to metal transition in m A 2 z 4 bilayers (m= Ti, Cr, Mo; a= Si; z= N, P).* Physical Review B, 2021. **103**(8): p. 085124.
140. Mak, K.F., et al., *Atomically thin MoS 2: a new direct-gap semiconductor.* Physical review letters, 2010. **105**(13): p. 136805.
141. Xu, X., et al., *Spin and pseudospins in layered transition metal dichalcogenides.* Nature Physics, 2014. **10**(5): p. 343-350.
142. Autieri, C., et al., *Limited Ferromagnetic Interactions in Monolayers of MPS3 (M= Mn and Ni).* The Journal of Physical Chemistry C, 2022. **126**(15): p. 6791-6802.
143. Basnet, R., et al., *Controlling magnetic exchange and anisotropy by non-magnetic ligand substitution in layered MPX3 (M= Ni, Mn; X= S, Se).* arXiv preprint arXiv:2205.04585, 2022.
144. Wang, W., et al., *Charge density wave instability and pressure-induced superconductivity in bulk 1 T− Nb S 2.* Physical Review B, 2020. **102**(15): p. 155115.
145. Wendumu, T.B., et al., *Optical properties of triangular molybdenum disulfide nanoflakes.* The Journal of Physical Chemistry Letters, 2014. **5**(21): p. 3636-3640.

146. Autieri, C., A. Bouhon, and B. Sanyal, *Gap opening and large spin–orbit splitting in (M= Mo, W; X= S, Se, Te) from the interplay between crystal field and hybridisations: insights from ab-initio theory.* Philosophical Magazine, 2017. **97**(35): p. 3381-3395.
147. Mak, K.F., et al., *Control of valley polarization in monolayer MoS 2 by optical helicity.* Nature nanotechnology, 2012. **7**(8): p. 494-498.
148. Xiao, F., et al., *Pressure-induced structural transition, metallization, and topological superconductivity in PdSSe.* Physical Review B, 2022. **105**(11): p. 115110.